

NORTHWESTERN UNIVERSITY

Polarimetric Imaging: From Optical Coherent Tomography to Laser Radar

A DISSERTATION

SUBMITTED TO THE GRADUATE SCHOOL
IN PARTIAL FULFILLMENT OF THE REQUIREMENTS

for the degree

DOCTOR OF PHILOSOPHY

Field of Electric Engineering

by

Xue Liu

EVANSTON, ILLINOIS

June 2012

© Copyright by Xue Liu 2012

All Rights Reserved

ABSTRACT

Polarimetric Imaging: From Optical Coherence Tomography to Laser Radar

Xue Liu

Polarization, the term used to describe the complex direction of the electric field vector, plays an essential role in the interaction of light and matter. Polarimetric imaging technique takes advantage of the fact that a given object emits and scatters light in a unique way depending on its properties, which allows us to distinguish objects with similar reflectivity but different polarimetric features. By breaking down the light into independent polarization components, one can often reveal occluded surface feature from the intensity-based images.

The subject of this thesis is polarimetric imaging. It addresses the science of acquiring, processing, and analyzing the polarization states of images. Any arbitrary polarization state of the light can be represented by the well-known Stokes Vector, with each of the four parameters of the vector being real observable quantities expressed in terms of polarization states. It represents both polarized and unpolarized in a very succinct vector form. The primary focus of this thesis is mapping the full Stokes vector of different scenarios for different applications under different constraints. We demonstrate an inline Stokesmeter architecture that circumvents the speed barrier of the conventional Stokesmeter and integrate it with Laser Radar (LADAR). This polarization-sensitive LADAR is applied to various scenes and found to yield the ability to detect

information indiscernible to a conventional, intensity-based LADAR. We also demonstrate theoretically and experimentally the first polarization-sensitive OCT (PSOCT) system capable of capturing the full Stokesmetric information of the biological sample reflection with the interferometry of unpolarized light using a combination of heterodyning and filtering techniques. In order to incorporate the outstanding ability of the PSOCT to take 3D image of object into the LADAR, we investigate a data buffering system making use of a pair of white light cavities (WLC). We study the possibilities of constructing the WLC with negatively dispersive medium or linearly chirped Bragg grating. The analysis show that optical delay can be achieved in WLC based on negatively dispersive medium while the accumulated effect of multiple scatterings at different locations inside the LCBG prevents the WLC being realized with simple LCBG.

Acknowledgements

Foremost, I would like to express my sincere gratitude to my advisor, Prof. Selim Shahriar, for his continuous support of my Ph.D. studies and research. Without his motivation, encouragement and guidance, this journey would not have been possible.

In addition, I would like to thank the rest of my thesis committee: Prof. Horace Yuen and Prof. Seng-Tiong Ho, for their insightful comments and helpful advices.

My sincere thanks also goes to my colleagues in the lab, Shih Tseng, Honam Yum, Subramanian Krishnamurthy, Ye Wang, Yanfei Tu, May Kim, Josh Yablon, etc. for their kind collaboration and help to me over the years.

Last but not the least, I would like to thank my family: my parents, Mingjiu Liu and Nina Zhong, for being the lighthouse at every step of my life; my wife, Wen Zhang, for bringing joy to my life.

Table of Contents

Acknowledgements.....	5
Table of Contents.....	6
List of Figures.....	9
List of Tables.....	14
Chapter 1 Polarimetric imaging.....	15
1.1 Introduction.....	15
Chapter 2 Polarization.....	19
2.1 Representation of the Polarization.....	19
2.1.1 Stokes vector.....	19
2.1.2 Mueller matrix.....	20
2.1.3 Poincare sphere.....	21
Chapter 3 Inline Stokesmeter.....	23
3.1 Classical Stokesmeter architecture.....	23
3.2 Inline Stokesmeter.....	24
3.3 Inline, spectrally selective holographic Stokesmeter.....	28
3.4 Measuring the Stokes Vector.....	29
3.5 Polarization imaging with the inline holographic Stokesmeter.....	31
Chapter 4 Volume-Grating Stokesmeter Based on Photonic Band Gap Structures.....	33

4.1 Background.....	33
4.2 Polarization dependent photonic band gap.....	34
4.3 Volume-grating Stokesmeter.....	38
Chapter 5 Polarization-Sensitive Optical Coherence Tomography (PSOCT).....	42
5.1. Optical coherence tomography (OCT).....	42
5.2 polarization-Sensitive Optical Coherence Tomography (PSOCT).....	44
5.3 Configuration of the PSOCT system.....	47
5.4. Mathematical Representation of the PSOCT.....	49
5.5. Results.....	55
5.5.1 Verification of the PSOCT system with single point light source.....	55
5.5.2 Stokesmetric imaging of biological sample.....	56
5.5.3 Backscattering Muellermetric imaging of biological sample.....	58
Chapter 6 PSOCT for Clinical Studies.....	62
6.1 Background.....	62
6.2 PSOCT for clinical application.....	63
6.3 PSOCT for ophthalmology.....	65
6.4 PSOCT for dermatology.....	68
Chapter 7 Polarimetric Laser Radar (LADAR).....	71
7.1 Introduction.....	71
7.2 Fully Automated Polarimetric Ladar System.....	73
7.3 Stokesmetric Imaging of Various Scenes.....	75

Chapter 8 White Light Cavity (WLC) based on superluminal effect 79

 8.1 Introduction..... 79

 8.2 Theoretical Model and Experimental Configuration: 81

Chapter 9 Optical data buffer based on ring WLC 85

 9.1 Introduction..... 85

 9.2 Fiber-based Fast-light Data Buffer 87

 9.3 Fast-light Data Buffer vs Conventional Fiber Loop Data Buffer 96

Chapter 10 Optical data buffer based on Linearly Chirped Bragg Grating (LCBG)..... 100

 10.1 Introduction..... 100

 10.2 White Light Cavity (WLC) condition..... 102

 10.3 Theoretical Analysis of Linearly Chirped Bragg Grating (LCBG) 104

 10.4 Simulating the LCBG with Transfer Matrix Method (TMM) 108

 10.5 Revisiting the reflection properties of the LCBG 110

Reference 113

List of Figures

<i>Fig. 1.1 Decomposed polarization of electro-magnetic wave in two orthogonal directions.....</i>	16
<i>Fig. 1.2 Pictures of a scene of interest taken by a regular camera with/without polarized filter in front of lens</i>	17
<i>Fig. 2.1 Examples of Stokes vector representation.....</i>	20
<i>Fig. 2.2 Poincare vector (\vec{P}) representations in the Poincare space.</i>	22
<i>Fig. 3.1 Classical Stokesmeter with a removable QWP and a rotating LP.....</i>	23
<i>Fig. 3.2 Inline automatic Stokesmeter with a rotating QWP and a rotating LP.</i>	24
<i>Fig. 3.3 High-speed inline Stokesmeter with two LCR's and a LP.....</i>	26
<i>Fig. 3.4 Schematic diagram of the inline, spectrally selective holographic Stokesmeter.</i>	28
<i>Fig. 3.5 Comparison of the Stokes parameters measured by the inline Stokesmeter and the classic Stokesmeter: (a) linear -45° polarized light. (b) linear horizontally polarized light. (c) right circularly polarized light.</i>	31
<i>Fig. 3.6 Polarization imaging for a set of objects with various polarization properties. The objects are illuminated by a left-circularly polarized light.</i>	32
<i>Fig. 4.1 (a) Two-dimensional photonic crystals that consist of six rows of 4mm diameter Pyrex rods ($\epsilon_r = 4.2$) on a 9mm square lattice. The z-polarized and y-polarized light is incident on the PBG structure along the x-axis. (b) Schematic diagram for PBG calculation (TF: total field, SF: scattered field, PBC: periodic boundary condition, ABC: absorbing boundary condition, Source: Gaussian pulse \times sinusoidal function).....</i>	34

Fig. 4.2 Photonic band gaps for z-polarized and y-polarized input beam for an array of 4mm diameter Pyrex rods ($\epsilon_r = 4.2$) on a 9mm square lattice.	36
Fig. 4.3 Photonic band gap for different linear polarization state with respect to the z-axis for an array of 4mm diameter Pyrex rods ($\epsilon_r = 4.2$) on a 9mm square lattice.	37
Fig. 4.4 The transmission of different linear polarization state for two different frequencies (e.g. 14 GHz and 15 GHz) in the band gap.....	38
Fig. 4.5 (a) Proposed architecture for a PC based volume-grating Stokesmeter (b) Input voltage signal scheme of two EOM's (EOM: electro-optic modulator, PBS: polarization beam splitter, PBG: Photonic Band Gap material, M: mirror, L: lens, D: detector, FPGA : Field Programmable Gate Array).....	39
Fig. 5.1 A fiber-based Optical coherence tomography (OCT) system.	42
Fig. 5.2 continuous train of pulses emitted by Super-Luminescent Diode (SLD).....	43
Fig. 5.3 Conventional PSOCT system.....	45
Fig. 5.4 Poincare-Stokes vector (\vec{S}_p) and Poincare vector (\vec{P}) representations in the Poincare space.	47
Fig. 5.5 Schematic diagram of the heterodyned PSOCT system. SLD: superluminescent diode; LP: linear polarizer; AOM: acousto-optic modulator; HWP: half wave plate; QWP: quarter wave plate; BS: beam splitter; M: mirror; DET: detector; HPF: high-pass filter; LPF: low-pass filter.	48
Fig. 5.6 Generating light of different degrees of depolarization. PBS: Polarization Beam Splitter; BS: Beam Splitter M: Mirror, PZT: Piezo Transducer	55

<i>Fig. 5.7 Theoretical and experimentally measured Stokes parameters for lights of different degrees of depolarization using the heterodyned PSOCT system. ♦ stands for the theoretical value, ● stands for the measured value.</i>	56
<i>Fig. 5.8 Stokesmetric imaging of different layers within the porcine muscle sample.</i>	57
<i>Fig. 5.9 Backscattering Mueller matrix images of the porcine tendon sample.</i>	59
<i>Fig. 5.10 3-D structure images of each Mueller matrix element of the tendon sample.....</i>	61
<i>Fig. 6.1 Schematic diagram of the PSOCT system. SLD: superluminescent diode; LP: linear polarizer; AOM: acousto-optic modulator; HWP: half wave plate; QWP: quarter wave plate; BS: beam splitter; M: mirror; DET: detector; HPF: high-pass filter; LPF: low-pass filter.....</i>	65
<i>Fig. 6.2 An eye sample holder</i>	66
<i>Fig. 6.3 Schematic diagram of Human eye.....</i>	67
<i>Fig. 6.4 (a) OCT image of a healthy human retina (b) OCT image of a detached retina</i>	68
<i>Fig. 6.5 OCT images of human skin based on the intensity and retardance of backscattered light.</i>	69
<i>Fig. 7.1 Schematic illustration of the fully-automated imaging Polarimetric LADAR.</i>	73
<i>Fig. 7.2 The activation and relaxation of phase delay of each LCR in a measurement cycle.....</i>	75
<i>Fig. 7.3 Stokesmetric images of objects illuminated by right circularly polarized light.....</i>	76
<i>Fig. 7.4 Stokesmetric images produced under right circularly polarized light, for an artificial harbor.</i>	78
<i>Fig. 8.1 WLC filled with Negative Dispersion Medium.....</i>	80

<i>Fig. 8.2 The dual-gain scheme to realize negative dispersion.</i>	81
<i>Fig. 8.3 Schematics of (a) fiber ring resonator, (b) ring resonator coupled to a single mode fiber</i>	82
<i>Fig. 8.4 WLC with the fast light medium switched on and off</i>	84
<i>Fig. 9.1 (a) Phases associated with the transfer functions of the resonator displayed in Fig. 1(b).</i> $\angle H_{b_1/a_1} = \arg(b_1/a_1)$, $\angle H_0 = \arg(a_1/a_1)$ in the absence of WLC effect, and $\angle H_{WLC} = \arg(a_1/a_1)$ for WLC, with $n_1 = -1.192 \times 10^{-15} / \text{rad}$, $n_3 = 1.223 \times 10^{-32} / \text{rad}^3$ (b) Reference pulse after propagating in a fiber of length ℓ (solid line) and the outputs associated with H_0 (dashed line) and H_{WLC} (circles). The output in the presence of the WLC effect is essentially overlapped with the reference.	91
<i>Fig. 9.2 Schematic illustration of the fiber-based data buffer system, employing bi-frequency Brillouin pumps. LWLC: Left White Light Cavity; RWLC: Right White Light Cavity.</i>	94
<i>Fig. 9.3 Output pulses from the fiber-based buffering system: (a) reference pulse, (b) pulse after 50 round trips inside the trapping loop.</i>	96
<i>Fig. 9.4 Schematics illustration of (a) a WLC-based data buffer augmented by amplification, (b) a conventional recirculating data buffer [13]; SLA: Semiconductor Laser Amplifier; WLC_{1,2}: White Light Cavity_{1,2}. In Fig. 6(b), the optical diode acts as an isolator.</i>	98
<i>Fig. 10.1 Schematic illustration of WLC: two reflectors are separated by L to form a modified FP cavity.</i>	102
<i>Fig. 10.2 Schematic illustration of a typical Fabry-Perot (FP) cavity of length L formed by a pair of LCBGs. Different wavelengths ($\lambda_1 < \lambda_2 < \lambda_3$) are reflected at different locations inside the grating region</i>	105

<i>Fig. 10.3 Coupled-mode model of light propagating in the LCBG</i>	105
<i>Fig. 10.4 The theoretical amplitude and phase of reflection coefficient for a negatively chirped LCBG.</i>	107
<i>Fig. 10.5 The simulated result for amplitude and phase of reflection coefficient for the LCBG.</i>	109
<i>Fig. 10.6 The attenuation of forward-propagating wave in the LCBG.</i>	110
<i>Fig. 10.7 The scheme and reflection spectrum of segmented apodized chirped grating.....</i>	111
<i>Fig. 10.8 The total phase for a round-trip propagation in the cavity based on segmented apodized chirped grating.</i>	112

List of Tables

<i>Table 3-1 Four sets of combinations of angles of QWP and LP that yield high A_L values.....</i>	<i>26</i>
<i>Table 5-1 Intensities for different polarization states.....</i>	<i>52</i>
<i>Table 5-2 The DOP and proportion of polarization components of Stokes Vector for different layers.....</i>	<i>57</i>

Chapter 1 Polarimetric imaging

1.1 Introduction

The primary physical quantities associated with any optical field are the amplitude, frequency and direction of the vibration, also called the polarization¹. The former two are perceivable to the human eyes for the amplitude/frequency of the light is represented by its brightness/color. However, the polarization, describing an ellipse formed by the electric field vector in a plane transverse to propagation, cannot be directly measured by intensity-based sensors, including the human eyes. As such, analyzing the polarization is of great significance for it can provide us with extra information carried by the light, especially after it is diffused or reflected by objects.

The history of human taking advantage of the polarized light dated back to about 1000 AD when the Vikings used crystals to observe the polarized sky light in foggy weather, and were thus able to navigate in the absence of sunlight. The first known quantitative work on observation of polarization was published by Erasmus Bartolinus in 1669. He was followed by Huygens who contributed most significantly to the field of optics by proposing the wave nature of light and discovering polarized light. Since then, the field of optics has been rich with literature on the nature and applications of polarized radiation. A long list of names of the pioneers who contributed to the development of polarimetric imaging, including D. Brewster (1816), A. Fresnel (1820), M. Faraday (1832), G.B. Stokes (1852), J.C. Maxwell (1873), W.O. Strutt–Lord Rayleigh (1881), H. Poincaré (1892) and R.C. Jones (1942). Of course, this list is incomplete and still expanding.

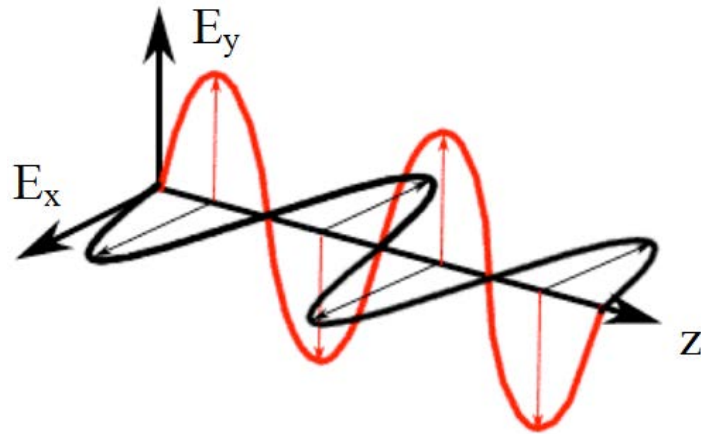


Fig. 1.1 Decomposed polarization of electro-magnetic wave in two orthogonal directions

The trace of the complex electric field vector forms an ellipse² in a plane transverse to propagation as shown in Fig. 1.1. The transformation of the wave vector behavior plays an essential role in the interaction between electromagnetic wave and matter^{3,4}. Thus the control of the polarization properties of optical waves is named “ellipsometry” in optical sensing and imaging, whereas it is called “polarimetry” in the fields of radar and ladar. As such, polarimetric imaging deals with the full vector nature of polarized electromagnetic waves. It takes advantage of the fact that a given object emits and scatters light in a unique way depending on its properties, which allows us to distinguish objects with similar reflectivity but different polarimetric features. By breaking down the light into independent polarization components, one can often reveal occluded surface information such as the composition, texture and roughness. As such, polarimetric imaging is utilized widely in many situations. For example, astrophysicists use polarimeters to measure the spatial distribution of magnetic fields on the surface of the sun⁵. In the field of medical imaging, researchers analyze the polarization of light through coherence interferometry to yield the details about the optical properties of biological tissues⁶. For defense

applications, polarization imaging is often used to detect objects through smoke and obscurants such as vegetation or camouflage⁷.



(a) Photograph of a window without using polarization filter



(b) Photograph of a window using a horizontally polarized filter

Fig. 1.2 Pictures of a scene of interest taken by a regular camera with/without polarized filter in front of lens

Fig.1.2 shows an example of utilizing a polarized filter in photography to reduce unwanted glare. The scattered skylight from the window has a significant level of polarization. By breaking down the reflection into independent polarization states (horizontal and vertical) and eliminating the undesirable light (in this case the vertically polarized light), we successfully reveal occluded information from the intensity-based images (Figure (a)). Of course, Figure 1.2a is merely a basic example of the many greatness polarimetric imaging brings to our lives.

Much formalism has been developed to describe the polarization of light, including the polarization ellipse, the Jones vector, the Stokes vector and the Poincare Sphere⁸. The polarimetric properties of light are most easily introduced using the wave nature of Electro-

Magnetic energy. As such, the Stokes vector, with each of the four parameters of the vector being real observable quantities expressed in terms of optical intensities, is of utmost interest to us because it can represent any arbitrary polarization state of light, both polarized and unpolarized, in a very succinct vector form.

The subject of this thesis is polarimetric imaging. It addresses the science of acquiring, processing, and analyzing the polarization states of images. The primary focus will be mapping the full Stokes vector in different applications under different constraints for different scenarios, especially for biomedical diagnosis and remote sensing. The rest of the thesis is organized as follows: In Chapter 2 we will introduce the conventional Stokesmeter and its limitations. In Chapter 3 we will propose an inline Stokesmeter architecture that circumvents this barrier of the conventional one. In Chapter 4 we introduce a multiplexing Stokesmeter based on Photonic Bandgap (PBG) structures. In Chapter 5 we investigated on the limitation of conventional Optical coherence tomography (OCT) to detect unpolarized light for it relies on interference between local oscillator and the target reflection. We demonstrate a scheme that overcomes this limitation by using heterodyne and filtering techniques. In Chapter 6 the clinical application of our PSOCT system is discussed. In Chapter 7 the high-speed polarimetric techniques are applied to complicated imaging systems such as the Polarimetric Laser Radar (PLADAR) system to ensure fast measurement. In Chapter 8 and 9 we discuss the combination of the OCT and PLADAR techniques to create the frame of coherent polarimetric LADAR and the active and passive optical buffers to enhance the dynamic detection range of the LADAR.

Chapter 2 Polarization

2.1 Representation of the Polarization

2.1.1 Stokes vector

Polarization-dependent reflectivity is quite common in nature. In fact, every surface alters the polarization of the incident radiation, if very slightly. Any arbitrary electric field can be expressed in the following form: $\vec{E} = \hat{e}_x E_x + \hat{e}_y E_y$. In the general case, E_x and E_y , the two orthogonal transverse components of the electric field, have time-varying amplitudes and phases as follows:

$$\begin{aligned} E_x &= E_{x0}(t)e^{i[\omega t + \phi_x(t)]} \\ E_y &= E_{y0}(t)e^{i[\omega t + \phi_y(t)]} \end{aligned} \quad (2.1)$$

The well-known, maybe also the best way to represent the polarization state of light is using the Stokes Vector⁹, which is defined in terms of E_x and E_y .

$$\bar{S}(\tau) \equiv \begin{pmatrix} I \\ Q \\ U \\ V \end{pmatrix} \equiv \begin{pmatrix} \langle E_x E_x^* \rangle + \langle E_y E_y^* \rangle \\ \langle E_x E_x^* \rangle - \langle E_y E_y^* \rangle \\ \langle E_x E_y^* \rangle + \langle E_y E_x^* \rangle \\ i \langle E_x E_y^* \rangle - i \langle E_y E_x^* \rangle \end{pmatrix}$$

(2.2)

where the brackets imply averaging over the observation time. I is the overall intensity, Q denotes the intensity difference between vertical and horizontal linear polarizations, U stands for

the intensity difference between linear polarizations at $+45^\circ$ and -45° , and V is the intensity difference between left and right circular polarizations. It should be noted that the parameters are arranged into a column vector only for convenience of representation.

The Stokes parameters are real observable quantities expressed in terms of optical intensities. For completely polarized light, $I^2 = Q^2 + U^2 + V^2$. For partially polarized light and unpolarized light, $I^2 > Q^2 + U^2 + V^2$. The normalized Stokes vectors for horizontal, vertical, 45° , and circularly polarized light follow easily as shown in Figure 2.1.

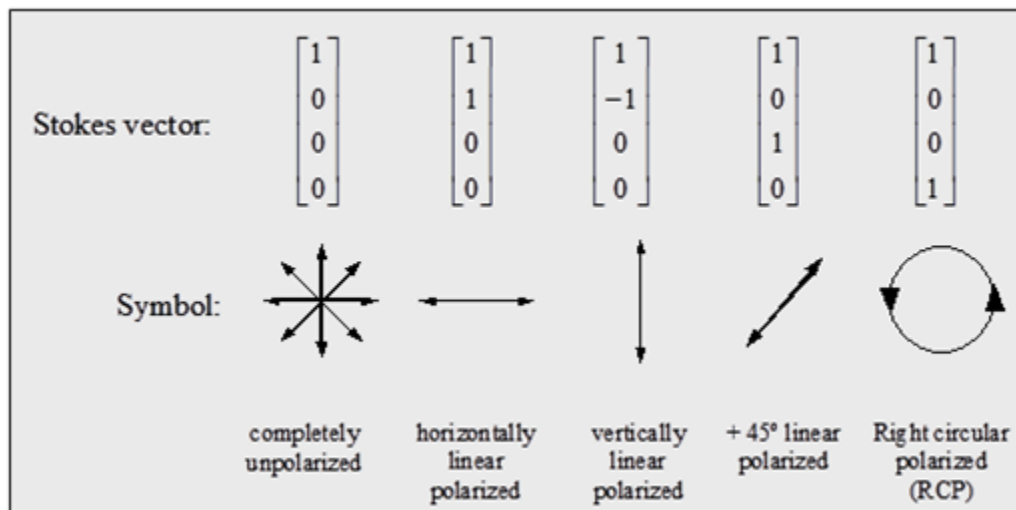


Fig. 2.1 Examples of Stokes vector representation

2.1.2 Mueller matrix

In the Mueller–Stokes formalism¹⁰, a 4×4 matrix, called the Mueller matrix¹¹ (denoted as M), is often used to describe mathematically how a medium alters the polarization of light¹². It relates

the Stokes vectors of incoming and outgoing light (denoted as \vec{S}_{in} and \vec{S}_{out} , respectively) via:

$\vec{S}_{out} = M\vec{S}_{in}$, which can also be explicitly written as the following:

$$\begin{pmatrix} I' \\ Q' \\ U' \\ V' \end{pmatrix} = \begin{pmatrix} M_{11} & M_{12} & M_{13} & M_{14} \\ M_{21} & M_{22} & M_{23} & M_{24} \\ M_{31} & M_{32} & M_{33} & M_{34} \\ M_{41} & M_{42} & M_{43} & M_{44} \end{pmatrix} \begin{pmatrix} I \\ Q \\ U \\ V \end{pmatrix} \quad (2.3)$$

The net Mueller matrix of the any optical system is given by the ordered product of the Mueller matrices of the individual elements. From the elements of the Mueller matrix, we can infer the properties of the medium such as the reflectance, absorption and birefringence.

It should be noted that compared with the also famous Jones matrix^{13,14,15} formalisms, the Stokes–Mueller approaches is different in many aspects although they both rely on linear algebra. Specifically, the Stokes–Mueller formalism has certain advantages. First of all, it encompasses any polarization state of light, whether it is totally or partially polarized while the Jones vector can only present polarized light. Secondly, the intensity-based nature of Stokes vectors and Mueller matrices makes the measurement of them relatively easy with conventional instruments, including wave plates and intensity meter. As such, we primarily focus on the Stokesmetric properties of light in this thesis.

2.1.3 Poincare sphere

One way to help visualize the change of Stokes vector is through the projection on a sphere called the Poincare sphere¹⁶. It rises from the trigonometric relation derived from the expression of the electric field. From Eqn. (2.1) we get

$$(E_{x0}^2 + E_{y0}^2)^2 - (E_{x0}^2 - E_{y0}^2)^2 - (2E_{x0}E_{y0} \cos(\delta_y - \delta_x))^2 - (2E_{x0}E_{y0} \sin(\delta_y - \delta_x))^2 = 0 \quad (2.4)$$

We can easily recognize the four quadratic terms correspond to the four parameters of the Stokes vector. The Poincare vector \vec{P} is defined as $\vec{P} = Q\hat{q} + U\hat{u} + V\hat{v}$, where \hat{q} , \hat{u} and \hat{v} are the unit vectors of the three axes in the Poincare space. Q , U and V are the corresponding parameters in the Stokes vector, as shown in Fig. 2.2. Note that points near the “equator” of the sphere are linearly polarized, while points near the “poles” are circularly polarized. In the Poincare space¹⁷, we can define another vector, called the Poincare-Stokes vector, denoted as \vec{S}_p . This vector is parallel to \vec{P} , but has a length equal to the total intensity, I . The difference in the length between $|\vec{S}_p|$ and $|\vec{P}|$ characterizes the degree of depolarization. A system capable of performing complete polarimetric imaging must be able to measure $|\vec{S}_p|$ in addition to \vec{P} .

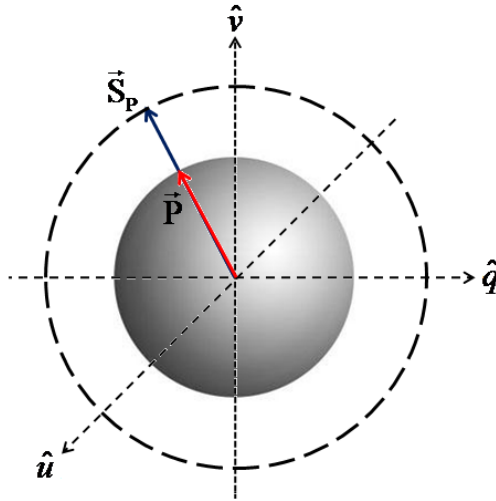


Fig. 2.2 Poincare vector (\vec{P}) representations in the Poincare space.

Chapter 3 Inline Stokesmeter

3.1 Classical Stokesmeter architecture

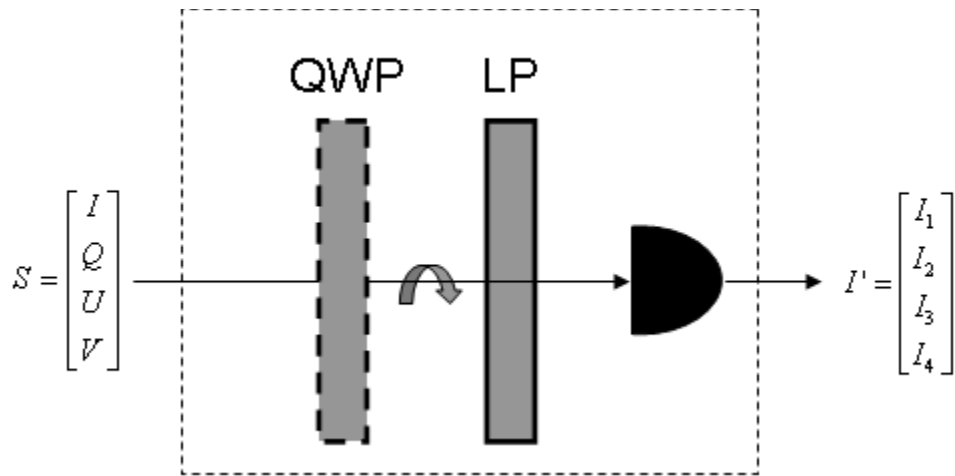


Fig. 3.1 Classical Stokesmeter with a removable QWP and a rotating LP.

The classical method¹⁸ to measure the Stokes parameters is illustrated in Fig. 3.1. It consists of a removable QWP and a rotating LP. The first three measurements of the transmitted intensity, denoted as I_1 , I_2 , and I_3 , are carried out with the QWP removed, while the transmission axis of the LP is rotated clockwise (when looking into the direction of the beam propagation) to 0° , 90° , and 45° , respectively. I_4 denotes the measured intensity after inserting the QWP with the fast axis at 0° and the LP oriented at 45° . The system can be represented by the equation

$$\bar{I} = A\bar{S} \quad (3.1)$$

where $\bar{I} = [I_1, I_2, I_3, I_4]^T$, \bar{S} is the input Stokes vector, and A is defined as the measurement matrix. The computed elements of A are given by

$$A = \frac{1}{2} \begin{bmatrix} 1 & 1 & 0 & 0 \\ 1 & -1 & 0 & 0 \\ 1 & 0 & 1 & 0 \\ 1 & 0 & 0 & 1 \end{bmatrix} \quad (3.2)$$

The Stokes vector \bar{S} is given by $\bar{S} = A^{-1}\bar{I}$

3.2 Inline Stokesmeter

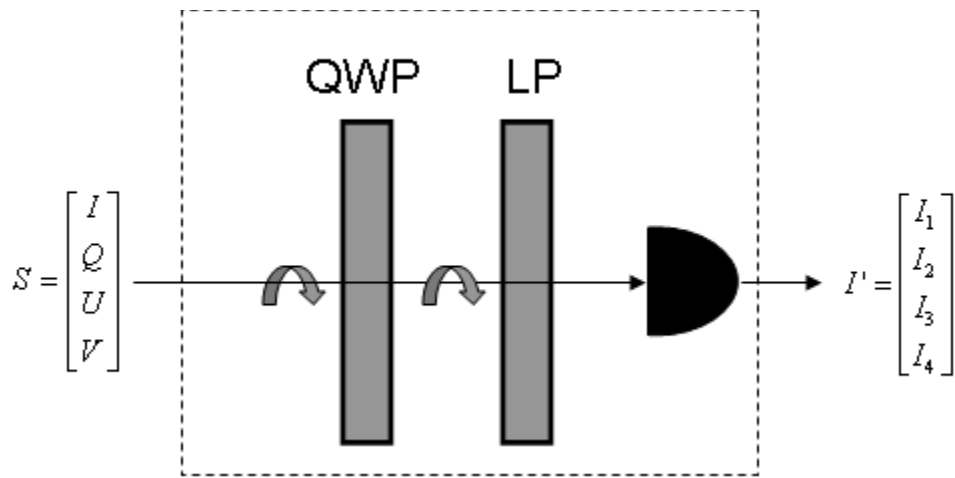


Fig. 3.2 Inline automatic Stokesmeter with a rotating QWP and a rotating LP.

Fig. 3.2 shows the inline Stokesmeter akin to what was presented by by Ambirajan and Look [16]. In this architecture, the QWP and the LP are rotated simultaneously for each measurement, which allows for higher operational speed than the classical Stokesmeter because no removal or insertion of the QWP is required. For an input light beam with a Stokes vectors $\bar{S} = [I, Q, U, V]^T$ transmitted through the QWP rotated at an angle β_i followed by the LP rotated at an angle α_i , the Stokes vector of the output beam $\bar{S}' = [I', Q', U', V']^T$ is

$$\bar{S}' = M \bar{S} \quad (3.3)$$

where $M = M_{LP} M_{QWP}$ equals the product of the Mueller matrices of the QWP and LP [18].

Using the well-known Mueller matrices for a QWP and an LP, the following relation is obtained

$$\begin{bmatrix} I' \\ Q' \\ U' \\ V' \end{bmatrix} = \frac{1}{2} \begin{bmatrix} 1 & \cos 2\beta_i \cos 2(\alpha_i - \beta_i) & \sin 2\beta_i \cos 2(\alpha_i - \beta_i) & \sin 2(\alpha_i - \beta_i) \\ \cos 2\alpha_i & \cos 2\alpha_i \cos 2\beta_i \cos 2(\alpha_i - \beta_i) & \cos 2\alpha_i \sin 2\beta_i \cos 2(\alpha_i - \beta_i) & \cos 2\alpha_i \sin 2(\alpha_i - \beta_i) \\ \sin 2\alpha_i & \sin 2\alpha_i \cos 2\beta_i \cos 2(\alpha_i - \beta_i) & \sin 2\alpha_i \sin 2\beta_i \cos 2(\alpha_i - \beta_i) & \sin 2\alpha_i \sin 2(\alpha_i - \beta_i) \\ 0 & 0 & 0 & 0 \end{bmatrix} \begin{bmatrix} I \\ Q \\ U \\ V \end{bmatrix} \quad (3.4)$$

The intensity observed by the detector, I' , is given by:

$$I'(\alpha_i, \beta_i) = \frac{1}{2} [I + Q \cos 2\beta_i \cos 2(\alpha_i - \beta_i) + U \sin 2\beta_i \cos 2(\alpha_i - \beta_i) + V \sin 2(\alpha_i - \beta_i)]. \quad (3.5)$$

In order to determine the four Stokes parameters, four measurements of the transmitted intensity

I' are taken with different combinations of α_i and β_i , yielding the equation $\bar{I} = A_{IL} \bar{S}$ where A_{IL} is

the measurement matrix for this system, given by

$$A_{IL} = \frac{1}{2} \begin{bmatrix} 1 & \cos 2\beta_1 \cos 2(\alpha_1 - \beta_1) & \sin 2\beta_1 \cos 2(\alpha_1 - \beta_1) & \sin 2(\alpha_1 - \beta_1) \\ 1 & \cos 2\beta_2 \cos 2(\alpha_2 - \beta_2) & \sin 2\beta_2 \cos 2(\alpha_2 - \beta_2) & \sin 2(\alpha_2 - \beta_2) \\ 1 & \cos 2\beta_3 \cos 2(\alpha_3 - \beta_3) & \sin 2\beta_3 \cos 2(\alpha_3 - \beta_3) & \sin 2(\alpha_3 - \beta_3) \\ 1 & \cos 2\beta_4 \cos 2(\alpha_4 - \beta_4) & \sin 2\beta_4 \cos 2(\alpha_4 - \beta_4) & \sin 2(\alpha_4 - \beta_4) \end{bmatrix} \quad (3.6)$$

The determinant of the measurement matrix, $|A_{IL}|$, governs in part the accuracy of the measurement process. We have carried out a systematic tabulation of $|A_{IL}|$ as a function of the angles α_i and β_i , and determined that $|A_{IL}|_{\max} = 0.184$. Note that this value is larger than $|A_{IL}| = 0.125$ for the conventional Stokesmeter. We found that more than one possible combinations yield this maximum value of $|A_{IL}|$, as shown in Table-1. Explicit choices of parameters in this form have not been reported previously, to the best of our knowledge.

Table 3-1 Four sets of combinations of angles of QWP and LP that yield high $|A_{IL}|$ values.

α_1	β_1	α_2	β_2	α_3	β_3	α_4	β_4	$ A_{IL} $
0°	60°	15°	0°	45°	45°	90°	15°	0.184
0°	60°	15°	0°	60°	60°	90°	15°	0.184
0°	75°	30°	30°	75°	90°	90°	30°	0.184
0°	75°	45°	45°	75°	90°	90°	30°	0.184

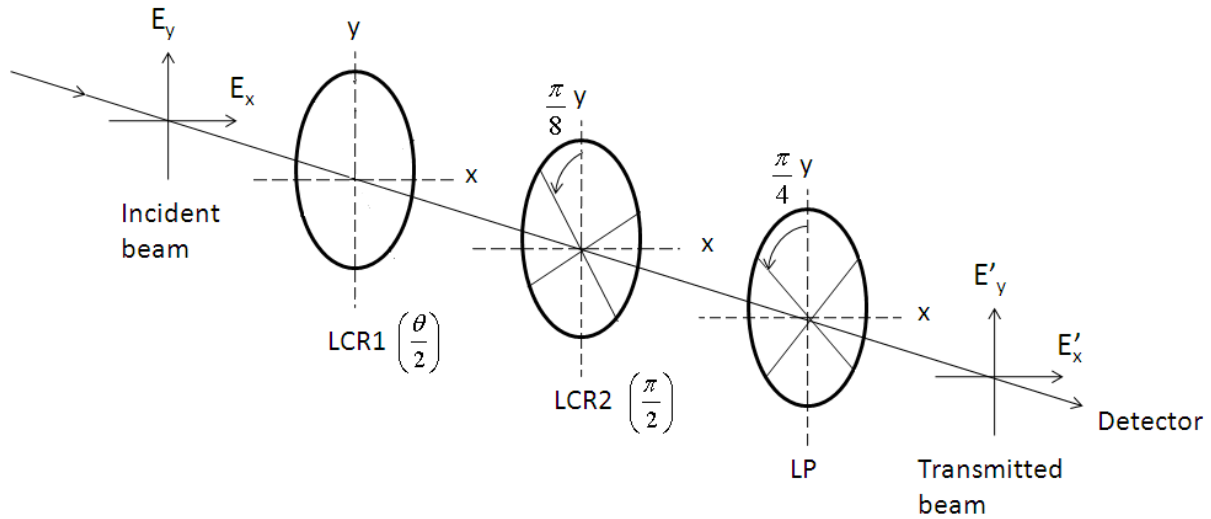


Fig. 3.3 High-speed inline Stokesmeter with two LCR's and a LP.

The Stokesmeter described above can be realized with components that are rotated mechanically. Alternatively, it is possible to construct a system with two voltage-controlled liquid crystal retarders (LCR) along with an LP at a fixed orientation^{19,20,21}. Free from any mechanical motion,

this device can easily achieve the video rate operation. Fig. 3.3 shows the basic schematic diagram of such a Stokesmeter. The incident light propagates through LCR1 and LCR2 (fast axis rotated by $\frac{\pi}{8}$) followed by an LP with the transmission axis oriented at $\frac{\pi}{4}$. The Mueller matrix

for this system is

$$M = M_{LP}\left(\frac{\pi}{4}\right)M_{LCR2}\left(\phi_2, \frac{\pi}{8}\right)M_{LCR1}\left(\phi_1\right)$$

$$= \frac{1}{2} \begin{bmatrix} 1 & \frac{1}{2}(1 - \cos \phi_2) & \frac{1}{2} \cos \phi_1 (1 + \cos \phi_2) - \frac{\sqrt{2}}{2} \sin \phi_1 \sin \phi_2 & \frac{1}{2} \sin \phi_1 (1 + \cos \phi_2) + \frac{\sqrt{2}}{2} \cos \phi_1 \sin \phi_2 \\ 0 & 0 & 0 & 0 \\ 1 & \frac{1}{2}(1 - \cos \phi_2) & \frac{1}{2} \cos \phi_1 (1 + \cos \phi_2) - \frac{\sqrt{2}}{2} \sin \phi_1 \sin \phi_2 & \frac{1}{2} \sin \phi_1 (1 + \cos \phi_2) + \frac{\sqrt{2}}{2} \cos \phi_1 \sin \phi_2 \\ 0 & 0 & 0 & 0 \end{bmatrix} \quad (3.7)$$

where ϕ_1 and ϕ_2 denote the phase retardations produced by LCR1 and LCR2, respectively. In the first three measurements, ϕ_1 is set to be 0, $\frac{\pi}{2}$ and π consecutively while ϕ_2 is kept 0. In the fourth measurement, the voltage on LCR2 is adjusted so that $\phi_2 = \pi$ while the phase retardation produced by LCR1 remains π . The measurement matrix for such a system, as calculated according to the first row of the Mueller matrix in eqn. 3.7, is found to be

$$A = \frac{1}{2} \begin{bmatrix} 1 & 0 & 1 & 0 \\ 1 & 0 & 0 & 1 \\ 1 & 0 & -1 & 0 \\ 1 & 1 & 0 & 0 \end{bmatrix} \quad (3.8)$$

The determinant of the measurement matrix is $|A| = 0.125$ for the particular implementation shown in Eqn.(3.8) We have found that this is the highest determinant achievable with this architecture. With the LCR (from Meadowlark® Inc.) used in our current setup, it takes

approximately 20ms to complete the full circle of four measurements, enabling it to be operated at a video-rate speed.

3.3 Inline, spectrally selective holographic Stokesmeter

The architecture described in Fig.3.3 makes use of a conventional polarizer. As an alternative, such a polarizer can be replaced by a holographic grating, designed to work as a spectrally selective polarizer. This architecture is illustrated schematically in Fig. 3.4.

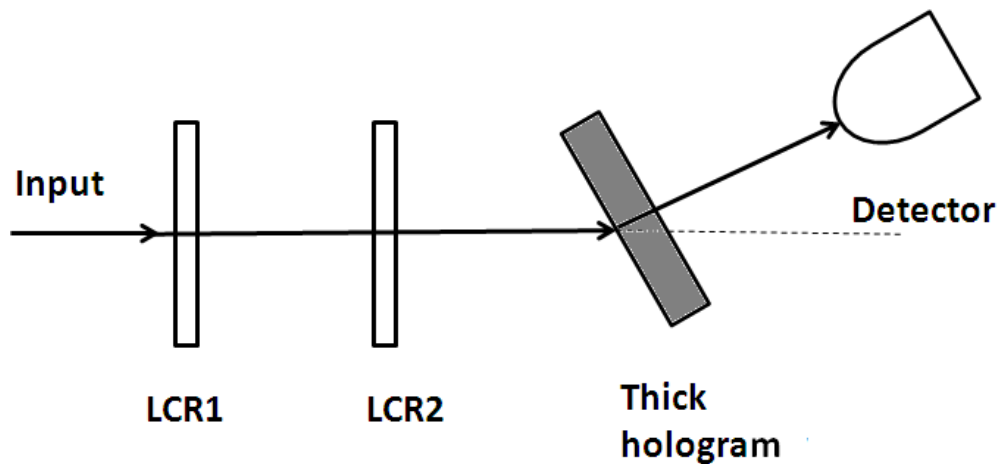


Fig. 3.4 Schematic diagram of the inline, spectrally selective holographic Stokesmeter.

In order to replace the LP oriented at 45° in the Stokesmeter demonstrated in Fig.3.3, the hologram is written to have a polarization selective diffraction efficiency, η , such that $\eta = \eta_0 \cos^2(\theta - \frac{\pi}{4})$ where θ is the angle of the input polarization with respect to the vertical axis with η_0 close to unity. Such a grating can easily be written, as discussed in ref.[19]. As shown in ref [25], this grating is also spectrally selective. For a given angle of incidence, only light in a

very narrow band ($\Delta\lambda \cong 1\text{nm}$ for a grating thickness of 1 mm) undergoes diffraction. Within this band, this device is then equivalent to the Stokesmeter discussed in section 3.3. Furthermore, by tilting its angular orientation, we can select a different band of light. Therefore, such a Stokesmeter is able to perform high speed spectrally multiplexed inline Stokesmetric imaging.

3.4 Measuring the Stokes Vector

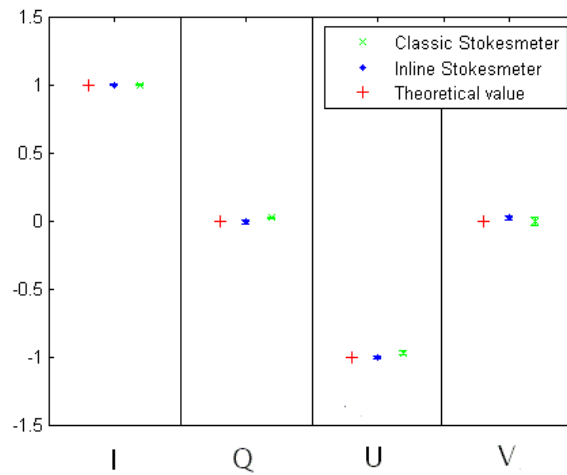
In section 3.3 we identified optimum operating conditions for the inline Stokesmeter for both the mechanical and LCR-based versions. In order to test the validity of these parameters, we have carried out measurement of the Stokes parameters using an inline Stokesmeter, and compared the results with those obtained using the classical architecture. For both architectures, we studied three different polarization states of light: (a) linear -45° polarized light, (b) linear horizontally polarized light and (c) right circularly polarized light. As shown in Fig. 3.5, compared with the measurement made by the classical Stokesmeter, the Stokes parameters measured by the inline architecture are closer to the theoretical value for all three cases. We define the accuracy of the measurement as follows

$$\varepsilon = \left(1 - \left| \frac{S_{mea} - S_{theo}}{I_{theo}} \right| \right) \times 100\%$$

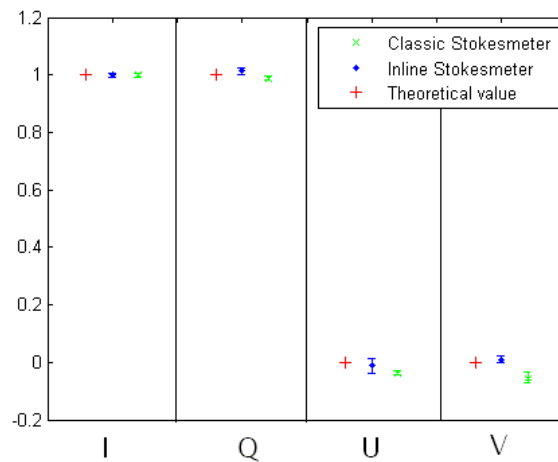
(3.9)

where S_{mea} and S_{theo} stand for measured and theoretical values of the Stokes parameters (I , Q , U and V). I_{theo} stands for the theoretical value of the intensity, which is normalized to unity in our calculation. The average accuracy of the measurements done by the inline Stokesmeter is

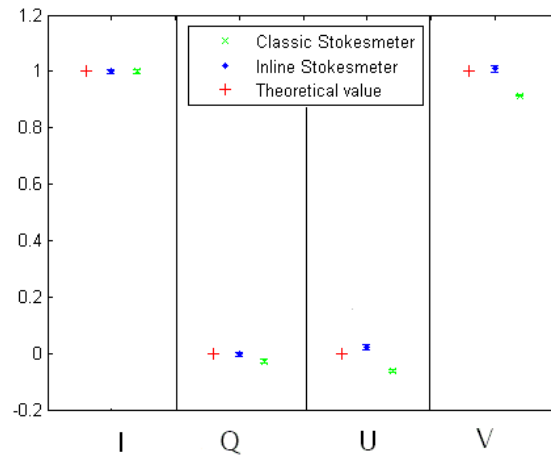
improved from 94.14% of the conventional method to 98.85% while the system error remains nearly unchanged (about 0.8%). The possible sources of this residual error include the imperfection of the HWP and LP, the imprecision in orientating the optical components and the inherent intensity noise in the detection process.



(a)



(b)



(c)

Fig. 3.5 Comparison of the Stokes parameters measured by the inline Stokesmeter and the classic Stokesmeter: (a) linear -45° polarized light. (b) linear horizontally polarized light. (c) right circularly polarized light.

3.5 Polarization imaging with the inline holographic Stokesmeter

We have used the inline automatic holographic Stokesmeter illustrated in Fig.3.4 to analyze the polarization images for an artificial scene. The tested objects of different polarimetric properties include leaves, sand paper and different types of metals. We purposely attached a transparent adhesive tape to one piece of metal in the center of the scene to form a shape of the letter “K”. The objects are illuminated by left circularly polarized light. The reflection is analyzed by the inline holographic Stokesmeter. Since the attached tape doesn’t change the reflectivity of the metal significantly, it cannot be easily identified in the camera view as shown in the first frame of Fig. 3.6. However, when the Stokes vector of light reflected by the scene is analyzed by the inline Stokesmeter, from the images that contains only the left/right circularly polarized light (V.

$/V_+$), the letter K shaped by the tape can be easily identified in the complex scenery due to the different polarimetric properties of the tape and the surroundings.

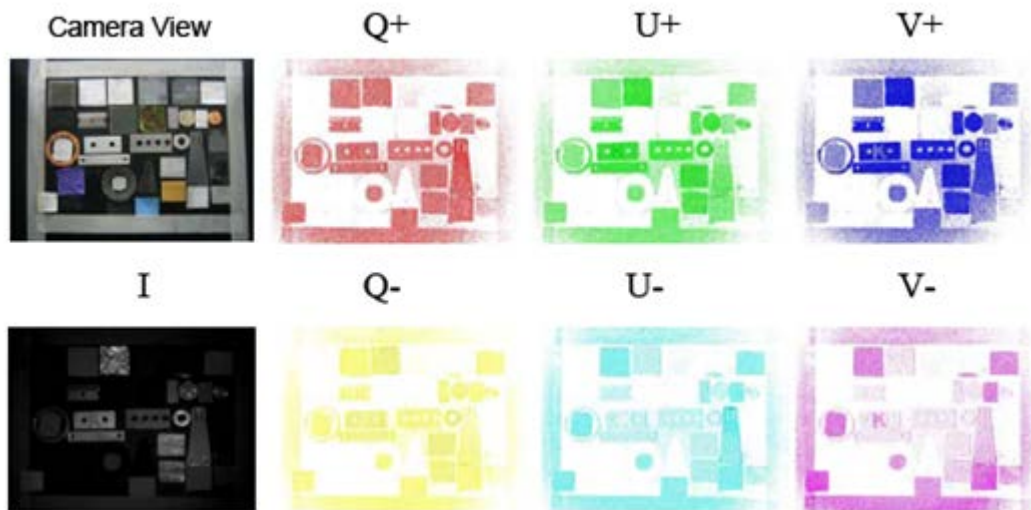


Fig. 3.6 Polarization imaging for a set of objects with various polarization properties. The objects are illuminated by a left-circularly polarized light.

Chapter 4 Volume-Grating Stokesmeter Based on Photonic Band Gap Structures

4.1 Background

Current polarization imaging systems, including mechanical quarter-wave plate/linear polarizer combinations, photodetectors with polarization filtering gratings etched onto the pixels, and liquid crystal variable retarders^{22,23,24}, can be limited in speed or by the lack of an ability to determine the complete Stokes vector. A holographic Stokesmeter (HSM)²⁵ uses the polarization dependence of volume grating diffraction efficiencies to determine all four Stokes parameters in parallel and at a high speed. However, the current HSM cannot be used for a wide frequency range due to limitations of thick holographic materials.

The polarization-dependent band gap characteristics have been experimentally observed for propagation in the plane of periodicity in both slab and bulk 2D Photonic Crystals (PC)^{26,27}, and has been used to create novel wave plates and polarization beam splitters²⁸. The polarization dependent properties of PC's can be tailored by adjusting the lattice geometry, size, and dimensionality, as well as the refractive indices of the constituent materials. Thus PC's are more versatile than the conventional devices in controlling polarization. In addition, since Maxwell's equations are scale-invariant, results obtained at one portion of the EM spectrum apply equally well across the entire spectrum with appropriate scaling of the structure. Therefore if we can

implement a volume-grating polarimeter using these properties of a PC, such devices can be operated over a wide range of frequencies.

4.2 Polarization dependent photonic band gap

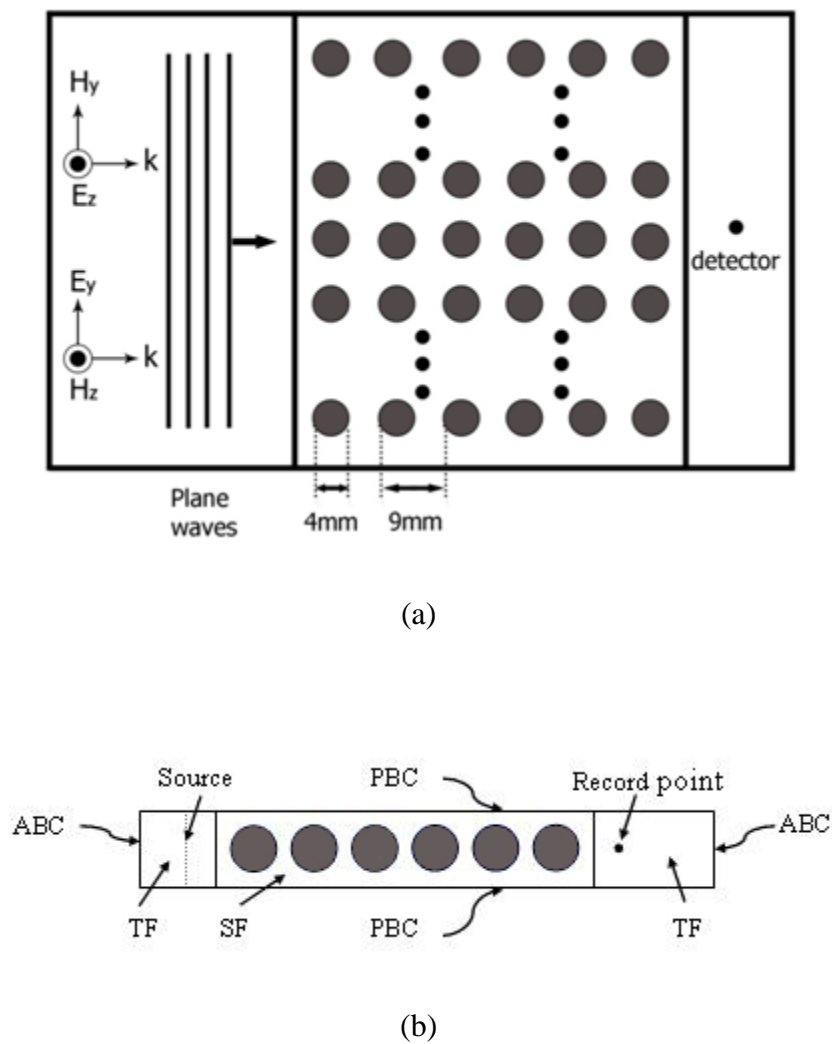


Fig. 4.1 (a) Two-dimensional photonic crystals that consist of six rows of 4mm diameter Pyrex rods ($\epsilon_r = 4.2$) on a 9mm square lattice. The z-polarized and y-polarized light is incident on the

PBG structure along the x-axis. (b) Schematic diagram for PBG calculation (TF: total field, SF: scattered field, PBC: periodic boundary condition, ABC: absorbing boundary condition, Source: Gaussian pulse \times sinusoidal function)

The 2-dimensional PBG structure we simulate for the Stokesmeter consists of six rows of 4mm diameter Pyrex rods ($\epsilon_r = 4.2$) on a 9mm square lattice, as shown in Fig. 4.1(a). The structure is assumed to extend to infinity in the y - and z - direction with no charge. The incident wave, into the PBG structure along the x -axis, is assumed uniform in the z -direction, so that all partial derivatives of the fields with respect to z equal to zero. We simulate a light wave-function normally incident (i.e. no E_x or H_x component) upon a slab with infinite extent in the y and z directions by placing one unit slab of the photonic crystal in the computational cell as shown in Fig. 4.1(b). The FDTD simulation is performed for both z -polarized (i.e. $E_y = 0$) and y -polarized (i.e. $E_z = 0$) light by sending a single pulse of light with a wide frequency profile multiplied by a sinusoidal wave through the PC. The output amplitudes are calibrated at a record point after the PC with and without the photonic crystal. By performing a Discrete Fourier Transform for both transmitted and incident amplitudes, we get the transmission spectrum as shown in Fig. 4.2. Deep absorptions in the frequency ranges of 12 GHz to 15 GHz and 23 GHz to 26 GHz are observed for the z -polarized case. For the y -polarized case, a shallow absorption around 17 GHz and a deep absorption around 27 GHz are produced.

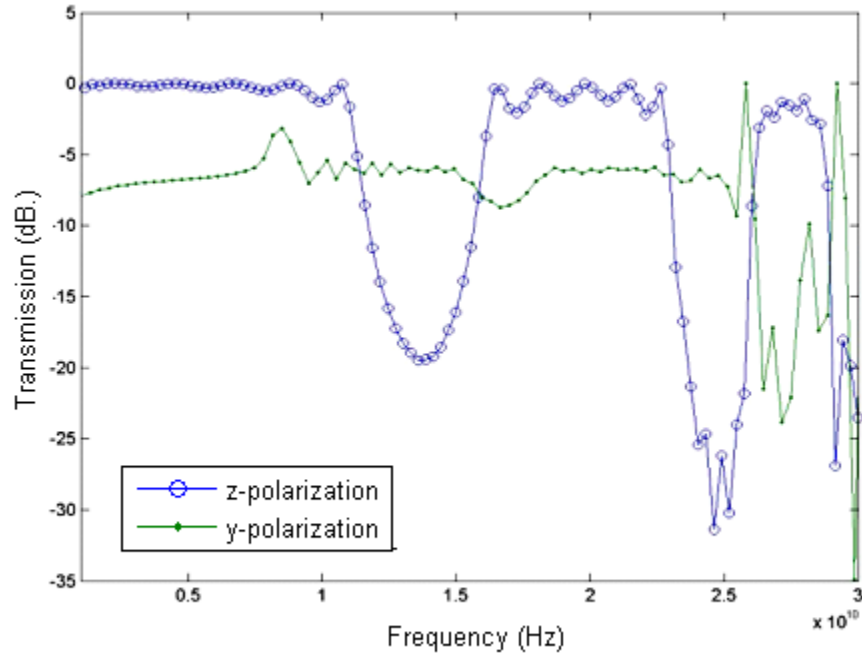


Fig. 4.2 Photonic band gaps for z-polarized and y-polarized input beam for an array of 4mm diameter Pyrex rods ($\epsilon_r = 4.2$) on a 9mm square lattice.

An arbitrary linear polarization state of the input beam is easily produced by rotating the direction of the electric field in the yz -plane. By performing FDTD simulation for such a beam, we find the transmission spectrum of this PBG structure has a significant dependence on the polarization state of the input beam, as illustrated in Fig. 4.3. As the angle of polarization of the incident wave in yz -plane increases from 0° to 90° (i.e., from z -polarization to y -polarization), the absorption dip becomes deeper. The transmission with respect to the linear polarization states are plotted for two sample frequencies inside the band gap (14 GHz and 15 GHz) as shown in Fig. 4.4, which are qualitatively similar to the polarization dependent diffraction efficiency from a volume holographic grating²⁹.

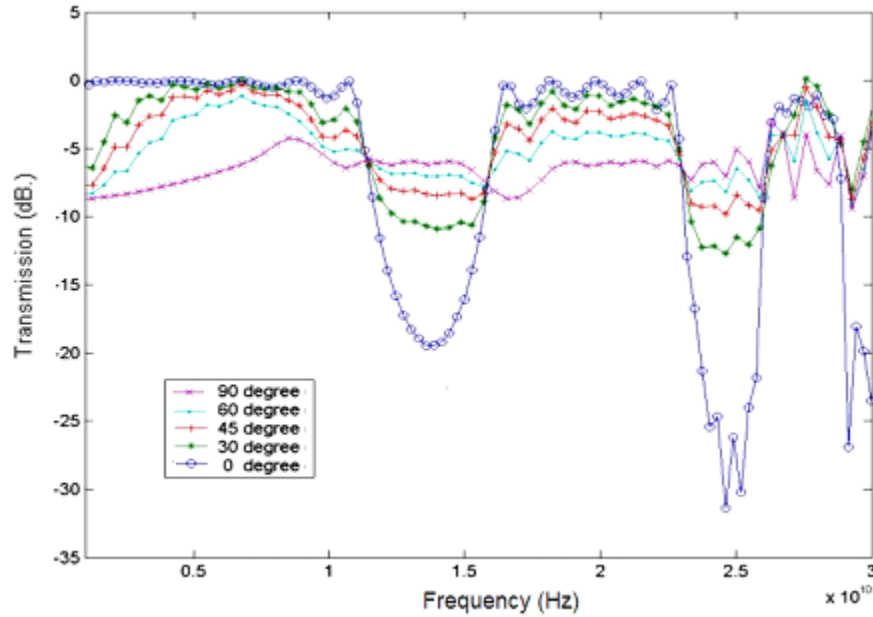


Fig. 4.3 Photonic band gap for different linear polarization state with respect to the z -axis for an array of 4mm diameter Pyrex rods ($\epsilon_r = 4.2$) on a 9mm square lattice.

We define the contrast ratio as $CR = \frac{T_{\max} - T_{\min}}{T_{\min}}$, where T_{\max} and T_{\min} denote the maximum and minimum transmission, respectively. As seen in Fig. 4.4, for frequency component at 14GHz (15GHz), the transmission varies from 0.012 (0.014) at 0° to 0.245 (0.256) at 90° , resulting in a CR of 95.2% (94.1%). Note that the simulated PC model consists of only 6 rows of Aluminum rod. In reality, more arrows of rods can be implemented to assure an almost 100% absorption at this frequency, meaning that this PBG structure may be used to as a polarimeter with a nearly perfect contrast ratio.

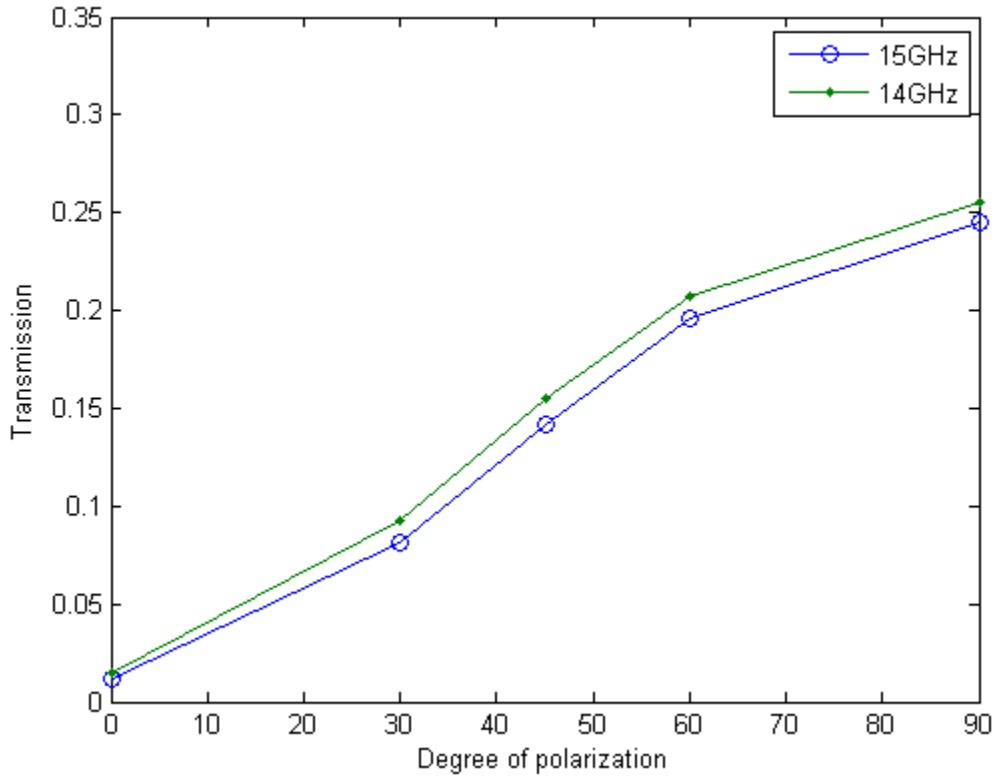
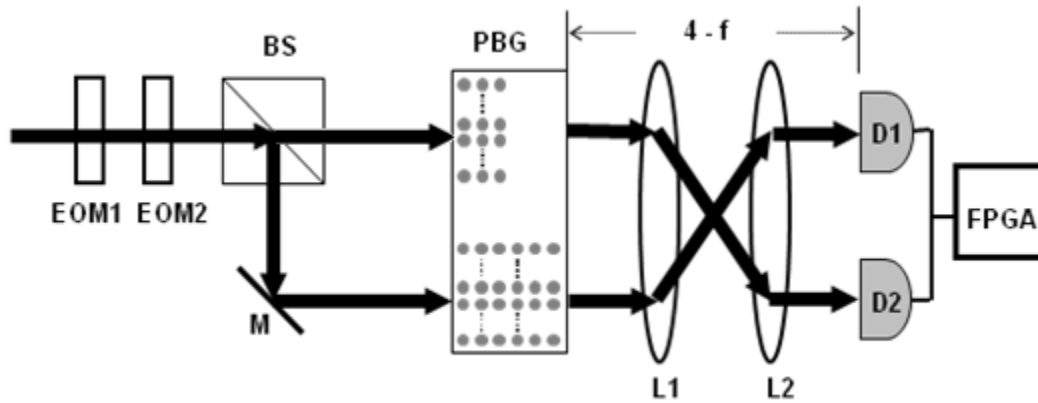


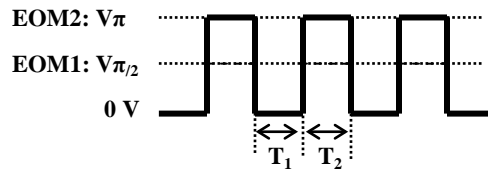
Fig. 4.4 The transmission of different linear polarization state for two different frequencies (e.g. 14 GHz and 15 GHz) in the band gap

4.3 Volume-grating Stokesmeter

Based on the polarization sensitivity of the PBG structure, we propose a volume-grating Stokesmeter as shown in Fig. 4.5(a), which consists of a pair of spatially separated volume gratings in a PC, two Electro-Optic Modulators (EOM's) and an imaging system.



(a)



(b)

Fig. 4.5 (a) Proposed architecture for a PC based volume-grating Stokesmeter (b) Input voltage signal scheme of two EOM's (EOM: electro-optic modulator, PBS: polarization beam splitter, PBG: Photonic Band Gap material, M: mirror, L: lens, D: detector, FPGA : Field Programmable Gate Array)

The basic structure of this device is almost the same as the compact version of holographic Stokesmeter³⁰ except that the volume gratings in a holographic material are replaced with the ones in a PC. The first and second EOM play the role of a quarter-wave plate and a half-wave plate respectively. The fast axis of the second EOM is rotated 45° with respect to that of the first EOM. In order to determine the Stokes Vector of the input beam, the transmitted beam is

measured twice separately at two time periods (T_1 and T_2) as shown at the bottom of Fig. 4.5(b). During the interval T_1 (T_2), the EOM's are turned off (on). I_{t1} (I_{t2}) indicate the intensity transmitted through the top (bottom) volume grating during the interval T_1 . Similarly, I_{t3} (I_{t4}) indicate the intensity transmitted through the top (bottom) volume grating during the interval T_2 . A_i (B_i) characterizes the diffraction efficiency of the i th (1: top, 2: bottom) grating for the z -polarized (y -polarized) input light. The angle γ_1/γ_2 denote the rotation of the substrate containing the 1st/2nd grating around the x -axis in the clockwise direction when looking in the $+x$ direction. By measuring all four transmitted beam intensities for a specific frequency in a PBG during intervals T_1 and T_2 , we can find the input Stokes parameters, as we did for the HSM¹⁶, through the following measurement matrix:

$$\begin{bmatrix} I_{t1} \\ I_{t2} \\ I_{t3} \\ I_{t4} \end{bmatrix} = \begin{bmatrix} A_1 + B_1 & (A_1 - B_1)\cos(2\gamma_1) & (A_1 - B_1)\sin(2\gamma_1) & 0 \\ A_2 + B_2 & (A_2 - B_2)\cos(2\gamma_2) & (A_2 - B_2)\sin(2\gamma_2) & 0 \\ A_1 + B_1 & -(A_1 - B_1)\cos(2\gamma_1) & 0 & (A_1 - B_1)\sin(2\gamma_1) \\ A_2 + B_2 & -(A_2 - B_2)\cos(2\gamma_2) & 0 & (A_2 - B_2)\sin(2\gamma_2) \end{bmatrix} \begin{bmatrix} I \\ Q \\ U \\ V \end{bmatrix} \quad (4.1)$$

Here, (I, Q, U, V) represents the input Stokes parameters.

We point out that if $\gamma_1 = \gamma_2$, different contrast ratios between the z - and y - polarized light are required for the two (top and bottom) gratings in Fig. 4.5. This can be seen mathematically from equation (1): the determinant of the measurement matrix vanishes if $A_1 = A_2$, $B_1 = B_2$ and $\gamma_1 = \gamma_2$. The volume-grating elements in this system can be a pair of spatially separated PBGs with two different numbers of rows of rods. Alternatively, these elements can be constructed with a pair of spatially separated PBG structure, where the diameters of the rods are different, but the distances between the rods are the same. Either way we can create the polarization-dependent transmission

spectrum for a specific frequency with two different contrast ratios of the transmitted beam intensities for y - and z - polarizations. Another alternative is to use different values of $\gamma_1 = \gamma_2$.

It is also possible to implement a spectrally resolved volume-grating Stokesmeter³¹ based on such PBG structures. Researchers have recently developed many structures activated by several external parameters, including electric field, magnetic field, and strain to implement tunable band stops in PBG^{32,33,34}. The tunability of band gaps is usually achieved by controlling the electric permittivity or the magnetic permeability of the constituent materials since the band gap positions are governed by the average refractive index of the composite. Thus, by using one of these methods to realize a tunable PBG structure in our architecture, it should be possible to implement a PBG based spectrally resolved polarimeter. Comparing with the classic polarization imaging systems, in which the mechanical rotations between the wave-plate and polarizer are needed for determining each Stokes parameter, the new imaging system works at a much faster speed.

Chapter 5 Polarization-Sensitive Optical Coherence

Tomography (PSOCT)

5.1. Optical coherence tomography (OCT)

Optical coherence tomography (OCT) is a relatively new technology for non-invasive biological imaging and non-destructive evaluation of materials^{35,36,37,38}. It is actually a spin-off from the telecommunications industry, where this technique is used in Optical Time Domain Reflector (OTDR) to determine the location of breakage in optical fiber. Scientists quickly discovered the value of this technique in the field of medical imaging.

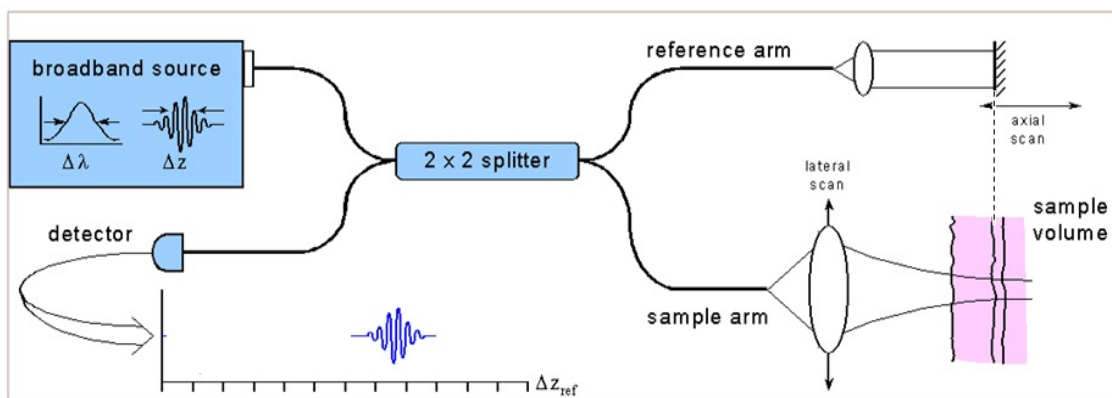


Fig. 5.1 A fiber-based Optical coherence tomography (OCT) system.

Simply put, The OCT in the most basic form is a Michelson interferometer. It is realizable either in free space or in optical fiber. The OCT technique is based on low coherence interferometry (LCI) depth-scanning of the sample in the time domain³⁹. As shown in fig. 5.1,

light source emits a pulse that is split into two arms. The pulse in reference/sample arm is reflected by mirror/biological sample, respectively. They are recombined and detected after the beam splitter. When the two arms have the identical optical path length, the two pulses will “see” each other and thus produce an interference pattern. When the optical path difference between the two arms exceeds the length of the pulse, the reflected pulse will “miss” each other. No interference will be produced. This scheme enables us to select the reference light to interfere with signal light from a specific layer of interest to us. If we run a scan to all the layers inside the sample, we can produce a 3D image of the object sample. Under such a scheme, the coherence length of the broadband light source determines the axial resolution of the OCT system. Currently, the OCT systems are able to discriminate the reflectivity of different depths within a sample typically at a micron-scale resolution^{40,41,42,43}.

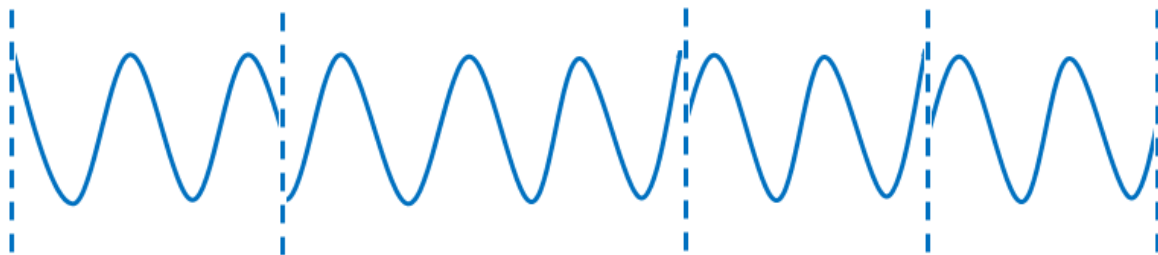


Fig. 5.2 continuous train of pulses emitted by Super-Luminescent Diode (SLD).

In a more realistic scenario, the light source used for OCT, called the Super-Luminescent Diode (SLD), usually emits a continuous train of pulses with different lifetimes rather than a single pulse, as shown in Fig. 5.2. The average of lifetime is called the coherence time, denoted as τ_c . There are random phase jumps between pulses, which ensure that one pulse will only

interfere with the reproduction of itself. The distance travelled in τ_c is called the coherence length of the light source, which determines the axial resolution of OCT system. It is associated with the bandwidth through the following equation

$$\Delta z = c \tau_c = \frac{c 2\sqrt{\ln 2}}{\Delta \omega} = \frac{\sqrt{\ln 2}}{\pi} \frac{\lambda_o^2}{\Delta \lambda} \quad (5.1)$$

The lateral resolution, on the other hand, depends on the focusing optics. Ideally, the spot size of Gaussian-profiled beam with width d focused by a perfect lens with focal length f is determined by

$$\Delta x = \frac{8\lambda}{\pi} \left(\frac{f}{d} \right) \quad (5.2)$$

In reality, there are other factors involved in the focusing of the beam such as the aberrations of the lens and the aperture size. Therefore, it is helpful to calculate the actual size of the focused spot using optical software like Zemax.

5.2 polarization-Sensitive Optical Coherence Tomography (PSOCT)

Many biological tissues, such as tendon, bone, and tooth, exhibit birefringence because of their linear or fibrous structure, which alters the polarization state of light propagating in them^{44,45}.

For the purpose of acquiring the polarimetric signatures of biological tissues, several polarization-sensitive OCT (PSOCT) systems have been developed in recent years^{46,47,48,49,50,51}.

For example, de Boer *et al* used the PSOCT system to generate images of thermally damaged tissue. Hitzenberger *et al* used the PSOCT to detect the phase retardation and fast axis orientation in chicken myocardium. Everett *et al* applied the PSOCT to the measurement of the

birefringence of porcine myocardium. Gang Yao *et al* reported a PSOCT system aiming to yield the full set of Mueller matrix images of biological tissues and turbid media.

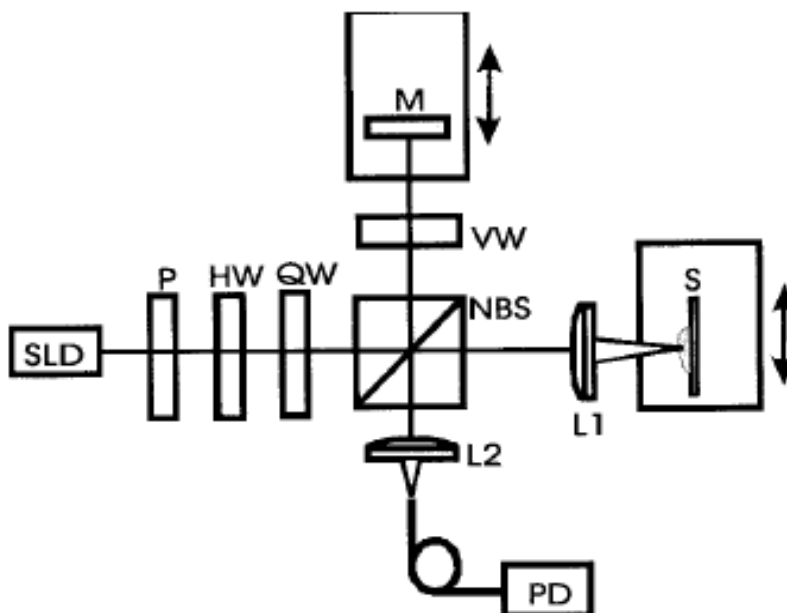


Fig. 5.3 Conventional PSOCT system

The PSOCT systems described in the ref.16-17 is shown in Fig. 5.3. However, it is not capable of capturing the unpolarized part of the light reflected from the sample. Because of the coherent-detection scheme in this OCT system, an incorrect Degree of Polarization (DOP) of unity for the reflected light is measured for the solid sample. In order to calculate the DOP of light backscattered by liquid media, the authors assume that the total amount of light returned by the sample remains the same as the depth is varied. Although this assumption is not explicitly stated in the paper, it is the only plausible explanation for the results presented. The DOP of different layers, normalized the DOP of the surface layer, is not the true DOP, since there is no evidence

that the total amount of light reflected remains unchanged at various depths. Furthermore, even if this were the case for this particular sample, it does not represent a technique of general validity nor utility. What is needed is an ability to measure DOP without resorting to a depth scan and without having to make assumptions about the constancy of the total return signal from various depths.

To illustrate this inadequacy, consider the Poincare sphere shown in Fig.5.4. The Poincare vector \vec{P} is defined as $\vec{P} = Q\hat{q} + U\hat{u} + V\hat{v}$, where \hat{q} , \hat{u} and \hat{v} are the unit vectors of the three axes in the Poincare space. Q denotes the intensity difference between vertical and horizontal linear polarizations; U stands for the intensity difference between linear polarizations at $+45^\circ$ and -45° , and V represents the intensity difference between left and right circular polarizations. In the Poincare space, we can define another vector, called the Poincare-Stokes vector, denoted as \vec{S}_p . This vector is parallel to \vec{P} , but has a length equal to the total intensity, I . The difference in the length between $|\vec{S}_p|$ and $|\vec{P}|$ characterizes the degree of depolarization. In the experiments of ref.'s 12 through 17, the system can only measure the magnitude and direction of \vec{P} . A system capable of performing complete polarimetric imaging must be able to measure $|\vec{S}_p|$ in addition to \vec{P} . Explicitly, in some cases the reflected light from the sample is partially polarized. The information carried by the unpolarized light, represented by the gap between the surfaces of the Poincare sphere and the intensity sphere of radius $|\vec{S}_p|$, is missed by the PSOCT's. This incapability results in incomplete information in the measurement of the Mueller matrix in ref [50] and [51]

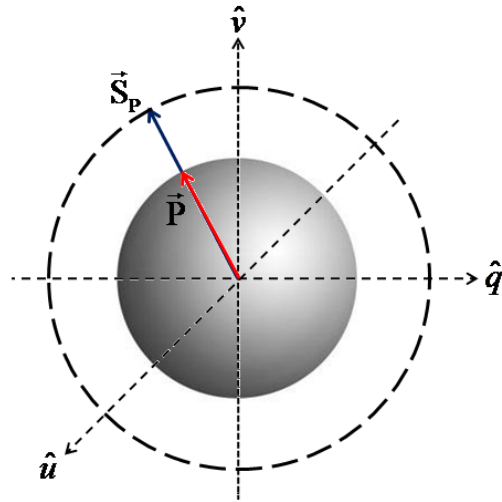


Fig. 5.4 Poincaré-Stokes vector (\vec{S}_p) and Poincaré vector (\vec{P}) representations in the Poincaré space.

5.3 Configuration of the PSOCT system

In this section, we demonstrate theoretically and experimentally the first PSOCT system capable of capturing the full Stokesmetric information of the sample reflection with the interferometry of unpolarized light using a combination of heterodyning and filtering techniques.

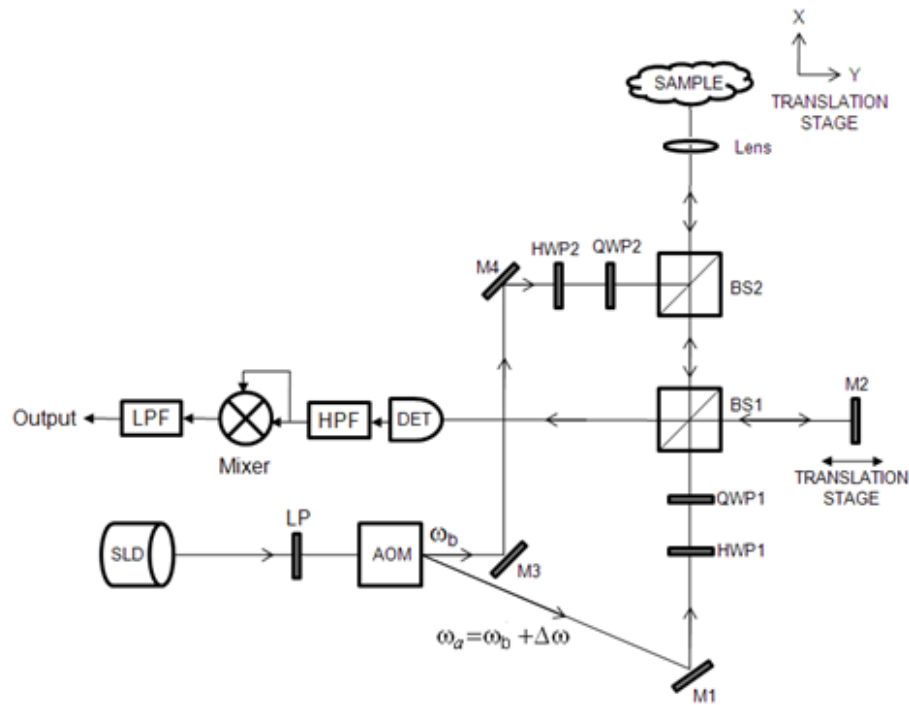


Fig. 5.5 Schematic diagram of the heterodyned PS-OCT system. SLD: superluminescent diode; LP: linear polarizer; AOM: acousto-optic modulator; HWP: half wave plate; QWP: quarter wave plate; BS: beam splitter; M: mirror; DET: detector; HPF: high-pass filter; LPF: low-pass filter.

Fig.5.5 depicts the configuration of the heterodyned polarization-sensitive OCT system. A collimated beam from a broadband superluminescent diode (SLD) at a central wavelength of 845nm is used as the light source. The linear polarizer (LP) selects a purely linear input state of the beam before being launched into the acousto-optic modulator (AOM). The unshifted beam at central frequency ω_b , and the first order diffraction at central frequency ω_a are coupled into the two arms of a modified Michelson interferometer as the incident sample beam and the reference

beam, respectively. A half-wave plate (HWP), followed by a quarter-wave plate (QWP) is placed on each arm of the Michelson interferometer to control the polarization state of the light. The probe beam is focused by a lens onto the sample mounted on a two-dimensional motorized translation stage, which can be driven for vertical and horizontal scans by computer programs. The backscattered light from the sample recombines with the reference beam at a non-polarizing beam splitter (BS1). Only when the optical path difference between the two arms is within the coherence length of the SLD source do the two beams produce a beat note at the central frequency $\omega = \omega_a - \omega_b$. Thus, by moving M2 axially on the translation stage, one can select backscattered light from different depth layers of the sample to heterodyne with the reference beam. A photodetector is placed after BS1. The detected signal is sent into a high pass filter (HPF) followed by a mixer and a low pass filter (LPF).

5.4. Mathematical Representation of the PSOCT

In this section we present a mathematical description of the heterodyned PSOCT system measurement of the Stokes vector of depolarized reflection from the sample. The electric field of the reference beam, which for generality we describe as elliptically polarized, is represented by

$$\vec{E}_r = (a_x \hat{x} + a_y \exp(i\delta_a) \hat{y}) \exp(i\omega_a t) \beta(t) \quad (5.3)$$

where a_x and a_y are the amplitudes of the electric fields in the x- and y- directions, respectively.

δ_a denotes the phase difference between the two components. ω_a is up-shifted 40MHz by the AOM from the central frequency of the SLD in the current experimental setup. $\beta(t)$ represents

the short coherence time of the laser source. For a broadband source such as the SLD, this can be expressed as $\beta(t) = \exp(i\phi(t))$ and has the following property⁵³:

$$\langle \beta(t)\beta^*(t-\tau) \rangle = \exp(-\gamma|\tau|) \quad (5.4)$$

Here, the angular bracket denotes time averaging and γ^{-1} represents the coherence time of the source. For a pulsed source, $\beta(t)$ represents the pulse envelope, leading to a characteristic correlation time of the order of the pulse width.

The back-scattered light from the sample, with an unknown polarization state, is expressed by the superposition of two separate components as follows,

$$\vec{E}_s(t') = [(b_x \hat{x} + b_y \exp(i\delta_b) \hat{y}) + (c \exp(i\delta_{cx}(t')) \hat{x} + c \exp(i\delta_{cy}(t')) \hat{y})] \exp(i\omega_b t') \exp(i\phi_b(t')) \beta(t') \quad (5.5)$$

where $t' = t - \tau_d$ with τ_d being the time difference between the sample and reference arms. The first part of this expression denotes the polarized light, with b_x and b_y representing the amplitudes of the electric field in the x- and y- directions, respectively and δ_b denoting the phase difference between the two components. The second part denotes the depolarized component of backscattered object light, for which the mean amplitudes of electric field in the x- and y- directions are equal, denoted as c . $\delta_{cx}(t')$ and $\delta_{cy}(t')$ represent the randomly changing phases of the two components, which have a property similar to that of $\beta(t)$. Specifically,

$$\langle \exp(i\delta_\phi(t)) \exp(-i\delta_\phi(t-\tau)) \rangle = \exp(-\gamma_p |\tau|) \quad [\phi=cx \text{ or } cy] \quad (5.6)$$

so that γ_p represents the bandwidth of depolarization. $\phi_b(t)$ denotes the relative phase fluctuation of the object beam with respect to the reference beam, due to the environment of the experiment,

for example. Here, we have ignored the reflected light at frequency ω_a since the heterodyning process readily eliminates it.

According to Eq.(5.5), the maximum heterodyned signal for a specific layer occurs when the light reflected by the layer traverses the same optical path length as the light in the reference arm, i.e., $\tau_d = 0$. In such a case, the total intensity of the signal seen by the detector, denoted as I' , can be written as

$$\begin{aligned} I' = \langle |\vec{E}_r + \vec{E}_s|^2 \rangle = & a_x^2 + b_x^2 + a_y^2 + b_y^2 + 2c^2 + \langle 2a_x b_x \cos(\omega t - \varphi_b(t)) \rangle \\ & + \langle 2a_y b_y \cos(\omega t - \varphi_b(t) + \delta_a - \delta_b) \rangle + \langle 2a_x c \cos(\omega t - \delta_{cx}(t) - \varphi_b(t)) \rangle \\ & + \langle 2a_y c \cos(\omega t + \delta_a - \delta_{cy}(t) - \varphi_b(t)) \rangle + \langle 2b_x c \cos(-\delta_{cx}(t)) \rangle + \langle 2b_y c \cos(\delta_b - \delta_{cy}(t)) \rangle \end{aligned} \quad (5.7)$$

where $\omega = \omega_a - \omega_b$ is the central frequency of the heterodyned signal. The angular brackets imply time-averaging over the detection process. Since $\varphi_b(t)$, $\delta_{cx}(t)$ and $\delta_{cy}(t)$ are randomly varying phases, the last two terms in Eq.(5.7) averages to 0 provided the detection bandwidth is much smaller than the depolarization bandwidth γ_p .

To measure the Stokes vector of the reflected object beam, we process the detected signal through the following filtering steps. First, we use the HPF to extract the beat note at frequency ω by filtering out the DC signal and noise. We assume that the low frequency cutoff for the HPF occurs at a frequency much larger than the bandwidth of any low-frequency system noise. The signal after the HPF becomes

$$\begin{aligned} I' = & 2a_x b_x \cos(\omega t - \varphi_b(t)) + 2a_x c \cos(\omega t - \delta_{cx}(t)) \\ & + 2a_y b_y \cos(\omega t - \varphi_b(t) + \delta_a - \delta_b) + 2a_y c \cos(\omega t + \delta_a - \delta_{cy}(t)) \end{aligned} \quad (5.8)$$

The signal is then squared by a mixer, which results in new DC components as well as sinusoidal signals at frequency 2ω . The DC part of the signal is extracted by the LPF with a bandwidth lower than the depolarization bandwidth γ_p . The final output from the LPF is

$$I' = \frac{1}{2}(2a_x b_x)^2 + \frac{1}{2}(2a_y b_y)^2 + \frac{1}{2}(2a_x c)^2 + \frac{1}{2}(2a_y c)^2 + (2a_x b_x)(2a_y b_y) \cos(\delta_a - \delta_b) \quad (5.9)$$

Eqn.(5.9) shows that the output signal depends on the polarization states of both the sample reflection and the reference beam. Here a_x , a_y and δ_a are controllable parameters for the reference arm. The four unknown quantities, b_x , b_y , c and δ_b , fully determine the Stokes vector of the reflected beam through the following expression⁵⁴

$$\vec{S}_r = [b_x^2 + b_y^2 + 2c^2, b_x^2 - b_y^2, 2b_x b_y \cos \delta_b, 2b_x b_y \sin \delta_b]^T \quad (5.10)$$

In principle, b_x , b_y , c and δ_b can be determined by analyzing the OCT signal generated by the sample reflection and the reference beam of four arbitrary linearly independent polarizations.

To illustrate this process systematically, we define first a convenient set of input polarization states. These are *vertical*, *horizontal*, *linear 45°*, *linear -45°*, *right circular* and *left circular*, denoted as V, H, P, M, R and L, respectively. The intensities of the output signal for different reference beams calculated from Eq.(5.9) are summarized in Table-5.1. Here, we have defined $a = \sqrt{I_r}$ for notational brevity where I_r denotes the intensity of the reference beam.

Table 5-1 Intensities for different polarization states

$I'_v = \frac{1}{2}(2ab_y)^2 + (2ac)^2$

$I'_H = \frac{1}{2}(2ab_x)^2 + (2ac)^2$
$I'_P = \frac{1}{2}((\sqrt{2}ab_x)^2 + (\sqrt{2}ac)^2 + (\sqrt{2}ab_y)^2 + (\sqrt{2}ac)^2) + (\sqrt{2}ab_x)(\sqrt{2}ab_y) \cos \delta_b$
$I'_M = \frac{1}{2}((\sqrt{2}ab_x)^2 + (\sqrt{2}ac)^2 + (\sqrt{2}ab_y)^2 + (\sqrt{2}ac)^2) - (\sqrt{2}ab_x)(\sqrt{2}ab_y) \cos \delta_b$
$I'_R = \frac{1}{2}((\sqrt{2}ab_x)^2 + (\sqrt{2}ac)^2 + (\sqrt{2}ab_y)^2 + (\sqrt{2}ac)^2) + (\sqrt{2}ab_x)(\sqrt{2}ab_y) \sin \delta_b$
$I'_L = \frac{1}{2}((\sqrt{2}ab_x)^2 + (\sqrt{2}ac)^2 + (\sqrt{2}ab_y)^2 + (\sqrt{2}ac)^2) - (\sqrt{2}ab_x)(\sqrt{2}ab_y) \sin \delta_b$

Based on the results in Table-5.1, the four parameters that determines the Stokes Vector in

Eqn.(5.10) are calculated as follows,

$$b_x = \left[(I'_H - I'_V) + \sqrt{(I'_H - I'_V)^2 + (I'_P - I'_M)^2 + (I'_R - I'_L)^2} \right]^{\frac{1}{2}}$$

(5.11.a)

$$b_y = \left[-(I'_H - I'_V) + \sqrt{(I'_H - I'_V)^2 + (I'_P - I'_M)^2 + (I'_R - I'_L)^2} \right]^{\frac{1}{2}}$$

(5.11.b)

$$c = \left[2I'_H - (I'_H - I'_V) - \sqrt{(I'_H - I'_V)^2 + (I'_P - I'_M)^2 + (I'_R - I'_L)^2} \right]^{\frac{1}{2}}$$

(5.11.c)

$$\delta_b = \tan^{-1} \left(\frac{I'_R - I'_L}{I'_P - I'_M} \right)$$

(5.11.d)

The Stokes vector can be simply expressed as

$$\vec{S}_r = [I'_H + I'_V, I'_H - I'_V, I'_P - I'_M, I'_R - I'_L]^T \quad (5.12)$$

However, due to the linear dependence (Note that $I'_H + I'_V = I'_P + I'_M = I'_R + I'_L$), Eqn. (5.12) can also be expressed by four linearly independent elements from the reference set, e.g.,

$$\vec{S}_r = [I'_H + I'_V, I'_H - I'_V, 2I'_P - I'_H - I'_V, 2I'_R - I'_H - I'_V]^T \quad (5.13)$$

Thus, by using four of the six inputs (e.g., H, V, P and R), we can determine \vec{S}_r .

The polarization dependent scattering property of the sample can be characterized fully by determining all element of the Mueller matrix, M, which relates the Stokes vector of the object beam (\vec{S}_o) to the Stokes vector of the scattered light (\vec{S}_r): $\vec{S}_r = M\vec{S}_o$. In order to determine the elements of M, it is necessary to vary the polarization of the object beam through four different orthogonal states. This can be accomplished by rotating HWP2 and QWP2 in Fig.5.5. A detailed analysis shows that the full Mueller matrix is given by

$$M = \begin{bmatrix} I'_{HH} + I'_{HV} + I'_{VH} + I'_{VV} & I'_{HH} + I'_{HV} - I'_{VH} - I'_{VV} & I'_{PH} + I'_{PV} - I'_{MH} - I'_{MV} & I'_{RH} + I'_{RV} - I'_{LH} - I'_{LV} \\ I'_{HH} - I'_{HV} + I'_{VH} - I'_{VV} & I'_{HH} - I'_{HV} - I'_{VH} + I'_{VV} & I'_{PH} - I'_{PV} - I'_{MH} + I'_{MV} & I'_{RH} - I'_{RV} - I'_{LH} + I'_{LV} \\ I'_{HP} - I'_{HM} + I'_{VP} - I'_{VM} & I'_{HP} - I'_{HM} - I'_{VP} + I'_{VM} & I'_{PP} - I'_{PM} - I'_{MP} + I'_{MM} & I'_{RP} - I'_{RM} - I'_{LP} + I'_{LM} \\ I'_{HR} - I'_{HL} + I'_{VR} - I'_{VL} & I'_{HR} - I'_{HL} - I'_{VR} + I'_{VL} & I'_{PR} - I'_{PL} - I'_{MR} + I'_{ML} & I'_{RR} - I'_{RL} - I'_{LR} + I'_{LL} \end{bmatrix} \quad (5.14)$$

where the first/second letter of the subscript denotes the polarization state of the incident object/reference beam, respectively.

5.5. Results

5.5.1 Verification of the PSOCT system with single point light source

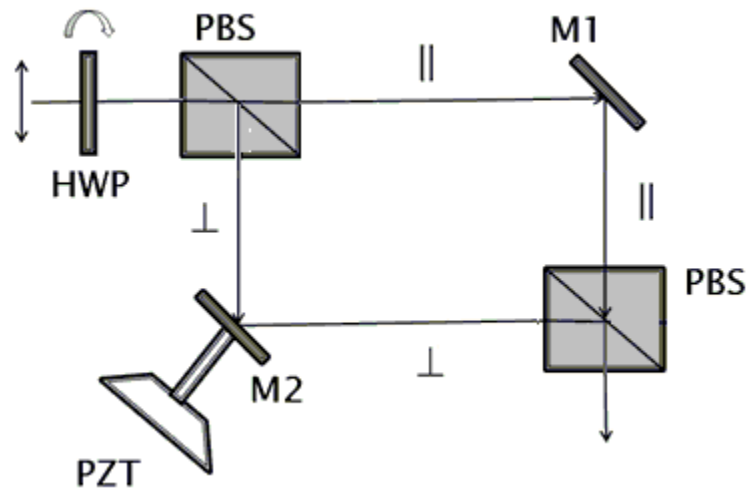


Fig. 5.6 Generating light of different degrees of depolarization. PBS: Polarization Beam

Splitter; BS: Beam Splitter M: Mirror, PZT: Piezo Transducer

To test the heterodyned PSOCT system, we generate partially polarized light using the configuration shown in Fig.5.6, and use it as a controlled form of sample reflection. The linear vertically polarized input light, after being rotated by a HWP, is split by a polarization beam splitter (PBS) into horizontally and vertically polarized components. The relative phase difference between these two paths is randomly changed between $-\pi$ and π by a mirror mounted on a Piezo transducer (PZT), which is driven by a noise signal produced by a computer using a random number generator. The two polarization components are recombined at a regular BS. When the amplitudes of the two components are equal, fully unpolarized light is achieved. We

can also change the ratio between the vertical and horizontal components by rotating the HWP, thus getting partially polarized light of different degrees of depolarization. Fig.5.7 shows the theoretical and measured Stokes parameters for unpolarized ($DOP = 0$) and two cases of partially polarized light ($DOP = 50\%$ for the first case and $DOP = 66.7\%$ for the second). The average deviation of the measured Stokes parameters using the heterodyned PSOCT system is 2.59% from the theoretical values, which may be attributable to the imprecision in orientating the optical components and the inherent intensity noise in the detection process.

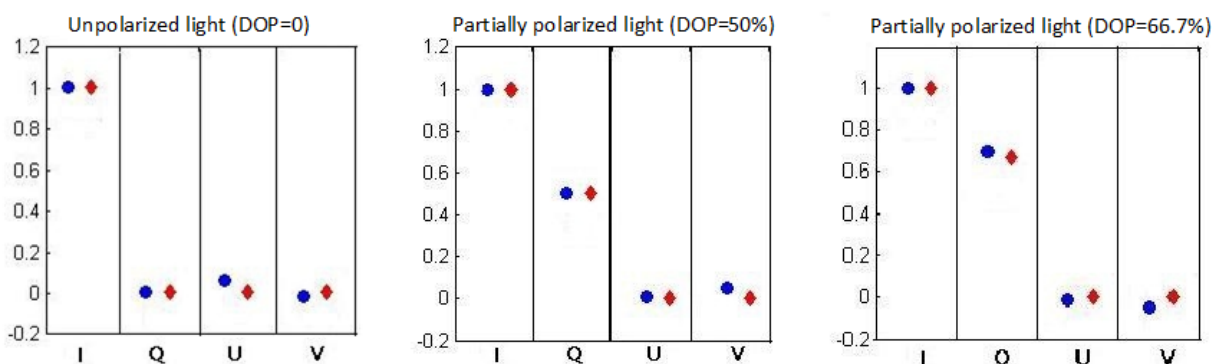


Fig. 5.7 Theoretical and experimentally measured Stokes parameters for lights of different degrees of depolarization using the heterodyned PSOCT system. ♦ stands for the theoretical value, ● stands for the measured value.

5.5.2 Stokesmetric imaging of biological sample

We applied the PSOCT system to perform Stokesmetric imaging of layers at varying depths in a porcine tendon sample. The imaged area ($2.4\text{mm} \times 2.0\text{mm}$) of the sample is chosen to consist of both muscle and fat. The incident object beam is set to be left-circularly polarized. The beam has a diameter of 40 microns after being focused by the lens. Two-dimensional image scanning

is performed to three layers of different depths in the sample: (I) the surface (II) the sub-surface layer 30 microns under a surface and (III) the sub-surface layer 50 microns under a surface. The Stokes vector of backscattered light collected at each scanning step, treated as a pixel, is analyzed according to eqn.(5.12) and plotted in Fig.5.8. For Q , U and V , green and red colors stand for positive and negative values, respectively. The fifth column shows the unpolarized part of the light.

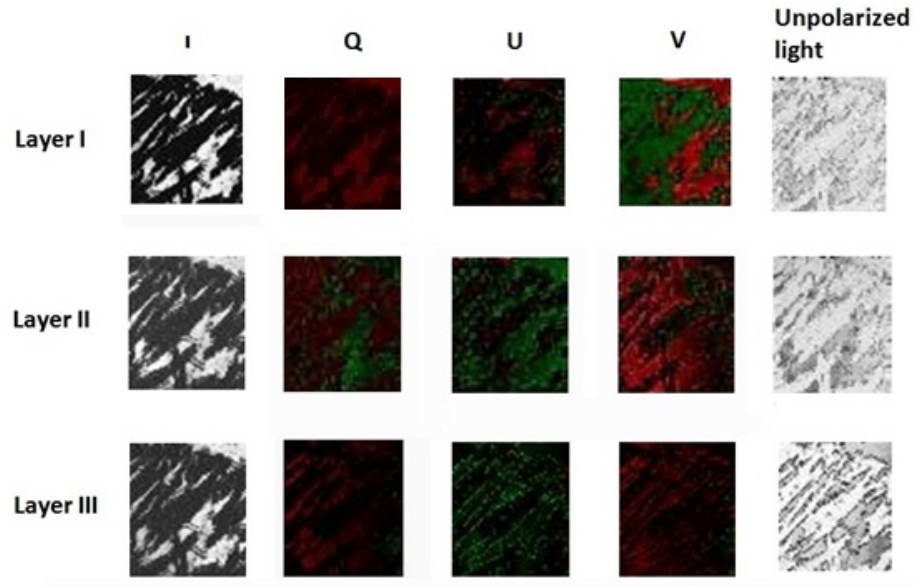


Fig. 5.8 Stokesmetric imaging of different layers within the porcine muscle sample.

Table 5-2 The DOP and proportion of polarization components of Stokes Vector for different layers.

	DOP (%)	$ Q ^2 / I^2$ (%)	$ U ^2 / I^2$ (%)	$ V ^2 / I^2$ (%)
Layer I	68.73	8.12	5.47	33.15
Layer II	55.10	13.77	7.60	8.98
Layer III	35.57	2.80	2.09	7.76

In Table-5.2, we present an analysis of this data for signals integrated over the whole image.

Note that these numbers very nearly satisfy the relation that $\text{DOP} = \left(\frac{|Q|^2 + |U|^2 + |V|^2}{I^2} \right)^{1/2}$. As

can be seen from Table-5.2, the DOP decreases as the depth of penetration in the sample increases. The table also shows that each layer couples the original polarization, which is purely circular, into linear polarizations to different extents. More importantly, as can be seen from Fig.5.8, the signs of the images for the Q and U elements, representing the directions of the linear polarizations, differ from one another for the three layers. As shown in ref.⁵⁵ and ref.⁵⁶, the change of the polarization of light in a medium has a dependence on the geometrical and optical properties of the particles. The differences of signs and values of the reflected Q and U images of the three layers may imply different compositions of particles.

5.5.3 Backscattering Muellermetric imaging of biological sample

We use the PSOCT to obtain the Muellermetric images of Layer III of the porcine tendon sample. In keeping with eqn. (5.14), thirty-six heterodyned images for different polarization combinations of the incident object beam and the reference beam are recorded. The sixteen

images corresponding to the 4×4 backscattered Mueller matrix are computed by linear combinations of the raw images according to eqn.(5.14). These are shown below in Fig. 5.9 where M_{ij} represents the i th row and the j th column of the Mueller matrix. Here again, green and red colors represent the positive and negative values, respectively.

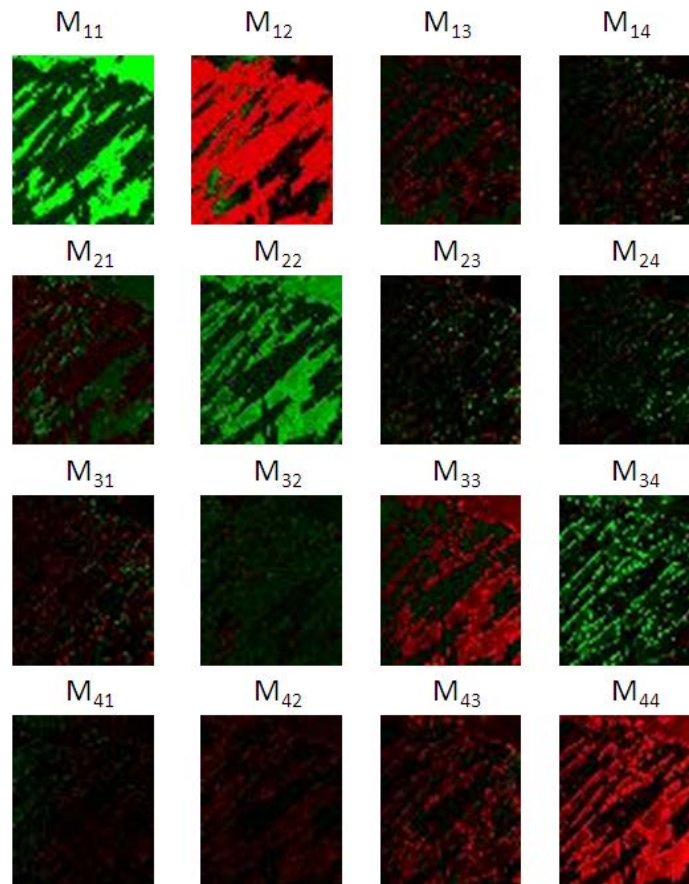


Fig. 5.9 Backscattering Mueller matrix images of the porcine tendon sample.

Fig. 5.9 leads to some important observations about the backscattering Mueller matrix of the layer of the tendon sample. (1) The diagonal elements have much bigger magnitude than the off-diagonal ones. Strong morphological patterns can be observed in the diagonal images. M_{33} and

M_{44} exhibit negative values due to the π phase-shift produced at reflection. (2) For the off-diagonal elements, M_{21} , M_{31} and M_{41} have near-zero amplitudes, which agrees with the fact that the sample can hardly convert unpolarized light into polarized light. The elements M_{34} and M_{43} , representing the coupling between circularly polarized light and 45° linearly polarized light, have significantly larger values than the other off-diagonal elements. The anti-symmetry (equal amplitude with opposite signs) of M_{34} and M_{43} indicate the birefringence produced by the sample. The phase delay between the horizontal and vertical polarizations turns the incident left-circularly polarized light into -45° linearly polarized light, which is readily shown on pictures in the third row of Fig.5. In addition, Some dotted patterns are observed on M_{34} . As we know, different particles cluster at different locations. The discontinuity may imply compositional variation on the layer.

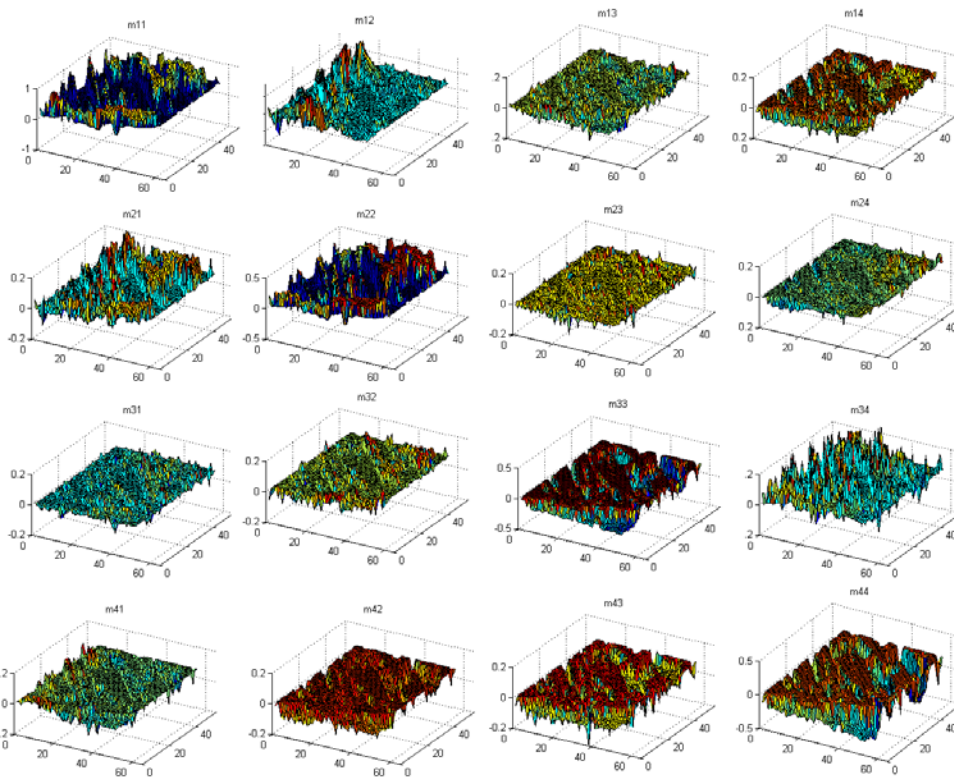


Fig. 5.10 3-D structure images of each Mueller matrix element of the tendon sample

The 3-D Muellermetric images of Layer III are plotted in Fig. 5.10. The variations in spatial structure of each elementary image can be readily observed in such pictures. The knowledge of the Mueller matrix of the sample enables us to determine the polarization state of back-scattered light from any point on the sample for any arbitrary probe beam. On the other hand, the 16 elements of the Mueller matrix fully characterize the polarimetric signature of the tissue, thus can be used for sample characterization and identification.

Chapter 6 PSOCT for Clinical Studies

6.1 Background

As shown in Chapter 5, OCT is a non-invasive imaging technique that yields high-resolution cross-sectional images of the internal microstructure of tissues^{57,58,59,60}. The superb optical sectioning ability of OCT results from the short coherence length of a broadband light source, which enables the OCT to map layers with micron-scale resolution. Thus, it has gained medical applications in various disciplines like cardiology, neurology and dentistry. However, the most dominating and promising application fields for OCT are still ophthalmology and dermatology. In ophthalmology the transparency of major ocular media provides a nearly unrestricted access of optical transmittance to the most important structures like cornea and retina. In dermatology the non-invasiveness of OCT technique allows the inspection of dermal morphological structures *in vivo*, bypassing the possibility of iatrogenic traumas that may occur as a result of a biopsy.

Biological media interact with the polarization of light through three different mechanisms: birefringence, diattenuation, and depolarization. While diattenuation is regarded negligible in most tissues, the other two interaction mechanisms are commonly found in various tissues. Birefringence is caused by asymmetrical structures of proteinic components such as collagen fibrils, microtubules and myosin filaments. The refractive index of some biological media is sensitive to the polarization of light in a manner identical to anisotropic crystals. Examples of birefringent biological media include the retina, skin, muscles and tendons. Scattering, on the other hand, may also alter the polarization state of the light. Even in the case of a single

scattering event the polarization state of the scattered light depends on the size and shape of the scattering particle. In a multiple-scattering scene, small changes by a single scattering event are accumulated, leading to a completely random polarization state (depolarization). Depolarization can be found in ocular tissues such as the retina nerve fiber and retinal pigment epithelium as well as dermal tissues like the stratum reticulare.

6.2 PSOCT for clinical application

Naturally, the information content of OCT images can be greatly enhanced if the light backscattered from the biological tissues can be analyzed polarimetrically. This kind of Polarization-sensitive OCT (PSOCT), combining the advantages of OCT (high depth resolution) and polarimetric imaging (sensitivity to polarization), provides a better contrast between different tissues, especially in diseases where biological layers are damaged, distorted or disappear altogether, thus making it difficult to identify specific layers based on backscattered intensity.

As shown in Chapter 2, the four-element Stokes vector completely characterizes the polarization of the reflected light. It can reveal the morphological and biochemical information, from both the polarized and depolarized parts, about the tissue that is not apparent in intensity-based OCT images. As such, the ability to detect depolarized light is crucial when the degree of polarization (DOP) of scattered light is the prominent indication for diseases. The Mueller Matrix images contain the maximum amount of information, including retardance, depolarization and diattenuation, which can be gleaned regarding the polarization characteristics of the medium.

As such, it is often thought of as the complete “optical polarization fingerprint” of a biological sample.

A lot of efforts have been made in recent years in developing various forms of PSOCT for clinical applications^{61,62,63,64,65,66,67,68,69}. Early work focused on measuring the birefringence, including axis orientation and retardation. For instance, Hitzenberger et al. studied phase retardation and fast axis orientation in chicken myocardium with the PSOCT system. Pierce et al. used a PSOCT system to illustrate the birefringence of collagen and the loss of such birefringence in thermally damaged tissues. Other work extended the measurements to many other parameters like the Jones matrix, Stokes vectors and Mueller matrix. For example, Ducros et al applied a PSOCT system to acquire depth-resolved images of the Stokes parameters of light reflected from ex vivo rabbit eyes. Yao et al. reported a PSOCT system that captured a partial set of MM images of biological tissues and turbid media. Gotzinger et al. mapped the retardation and slow axis distribution of the human cornea. Ducros et al. also determined the thickness of the retinal nerve fiber layer for both human and Rhesus monkey by measuring the retardation between incident and backscattered polarized light. Smith showed the potential to discriminate between cancerous and benign moles from their Mueller-matrix images taken by PSOCT.

On the clinical side, Carl Zeiss Meditec has developed a PSOCT system capable of identifying glaucoma by quantifying changes to the retinal ganglion cell axons by measuring the linear retardance in the retinal nerve fiber layer.

In Chapter 5, we have demonstrated a complete PSOCT system that is able to determine the full Stokes vector. The full 4×4 MM images of a biological sample can be obtained with this PSOCT system. This was also reported in a recent paper by our group⁷⁰.

6.3 PSOCT for ophthalmology

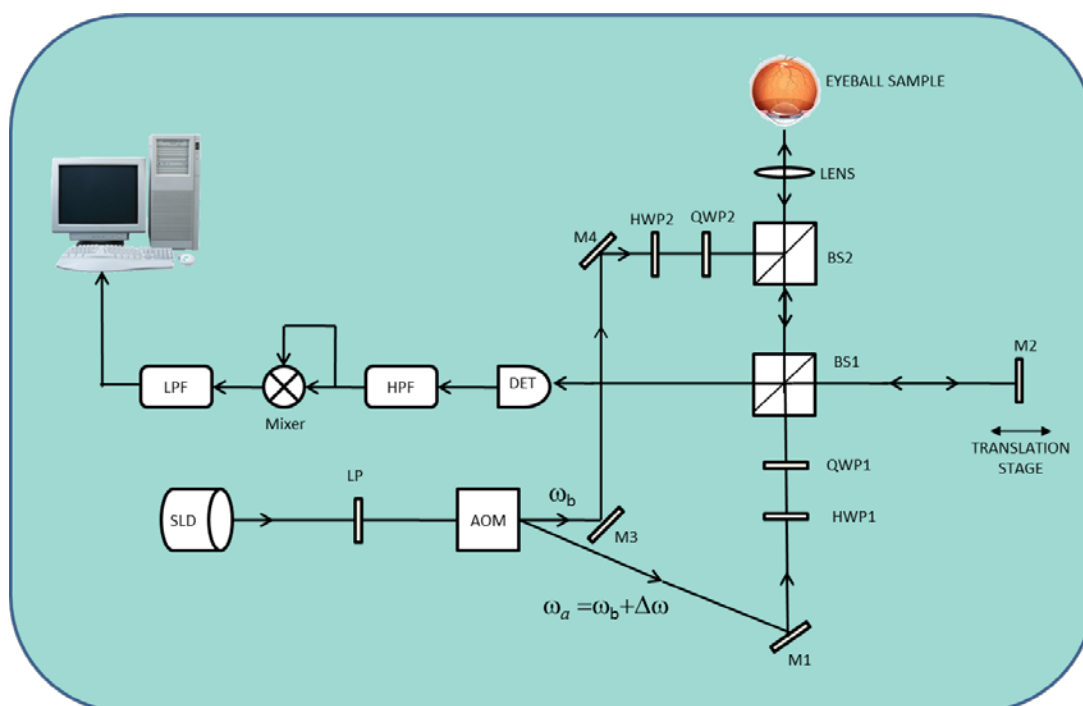


Fig. 6.1 Schematic diagram of the PSOCT system. SLD: superluminescent diode; LP: linear polarizer; AOM: acousto-optic modulator; HWP: half wave plate; QWP: quarter wave plate; BS: beam splitter; M: mirror; DET: detector; HPF: high-pass filter; LPF: low-pass filter.

The configuration of our PSOCT system is depicted in Fig. 6.1. It is a variation of the conventional OCT architecture, augmented by heterodyning and filtering techniques. We have a detailed description about the mechanism of the PSOCT in Chapter 5. It should be noted that

special attention should be paid to the preparation of samples for the PSOCT system to ensure that the maximum amount of light is incident on the layer of interest and collected while the physical and biomedical properties of the sample remain unchanged. For example, in preparing the ex vivo eye sample of an animal, the eye is acquired immediately post mortem, then enucleated and placed in a chilled saline solution. The sample holder is depicted in Fig. 6.2. The entry window of the eye holder, a flat glass slide, is gently pressed against the cornea to reduce the refraction and maintain the eye in a stable position. For imaging the retina, the beam focus is placed approximately on the superior region of the optic nerve head. A red aiming beam, aligned with the broadband infrared SLD beam, is used to determine the imaging position on the retina.

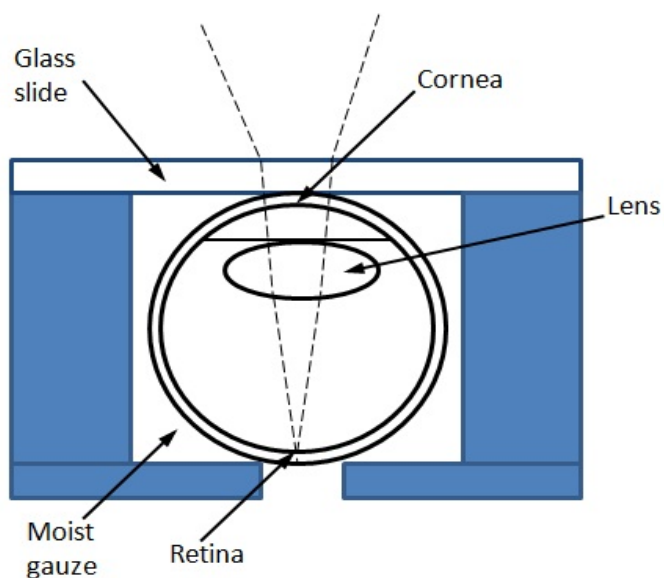


Fig. 6.2 An eye sample holder

Ocular pathology shows that many diseases (e.g., glaucoma, age-related macular degeneration) affect the macular region of the retina. The center of this region, the fovea, as shown in the green circle in Fig. 6.3, is most important because in the healthy eye it corresponds

to the location on the retina with the best vision. Many early pathological changes are accompanied by physical deformation in the macular region. For instance, glaucoma, the second leading cause of blindness worldwide, is associated with the loss of the axon of ganglion cells in the retinal nerve fiber layer. As such, the macula of retina has been the focus of ophthalmological OCT studies. Fig. 6.4 shows the OCT image of a healthy human retina and a detached retina due to a dense cataract.

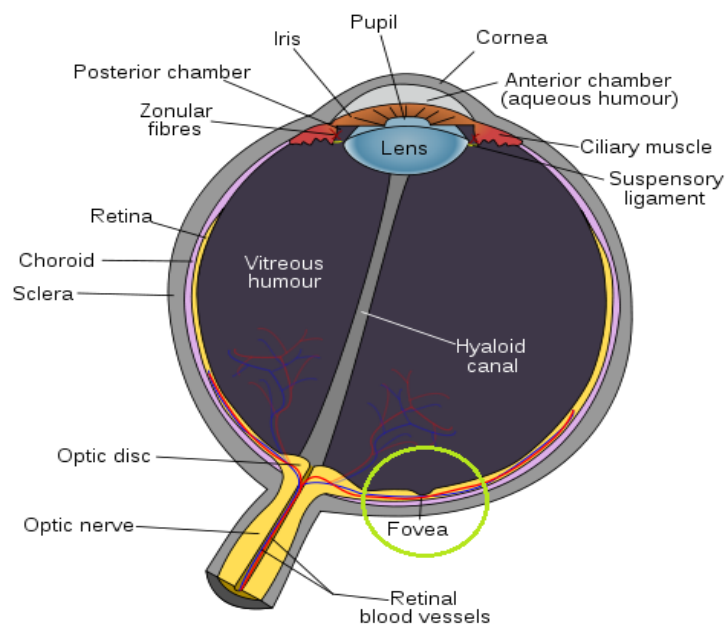


Fig. 6.3 Schematic diagram of Human eye

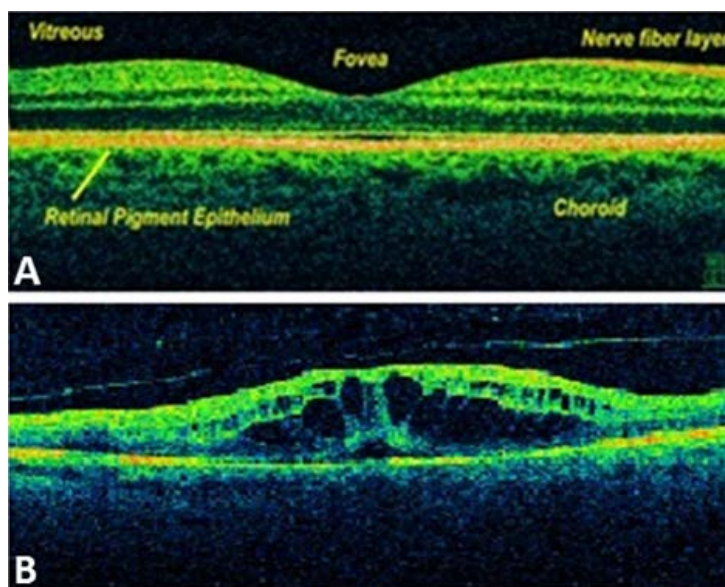


Fig. 6.4 (a) OCT image of a healthy human retina (b) OCT image of a detached retina

6.4 PSOCT for dermatology

The PSOCT is also proved useful in identifying a variety of dermatological conditions. In skin, birefringence is attributed to the regular arrangement of collagen fibers in the dermis. Loss of collagen structure and integrity is often associated with abnormalities of the skin, including tumors and connective tissue diseases, suggesting that birefringence assessments may prove valuable as a diagnostic indicator of certain pathologies. Fig. 6.5 shows an example of OCT images of human skin based on phase retardation caused by birefringence. In addition, OCT might be a promising diagnostic tool for the detection of skin tumors, such as basal cell carcinoma. Studies have shown that dermal tissues at the early stage of cancer are less depolarizing than healthy ones; both cancerous and healthy tissues act like partial depolarizer, with neither significant diattenuation nor retardance. This effect is caused by the presence of

subsurface structures beneath cancerous moles that prevent light from penetrating the tissue as deeply as in normal skin.

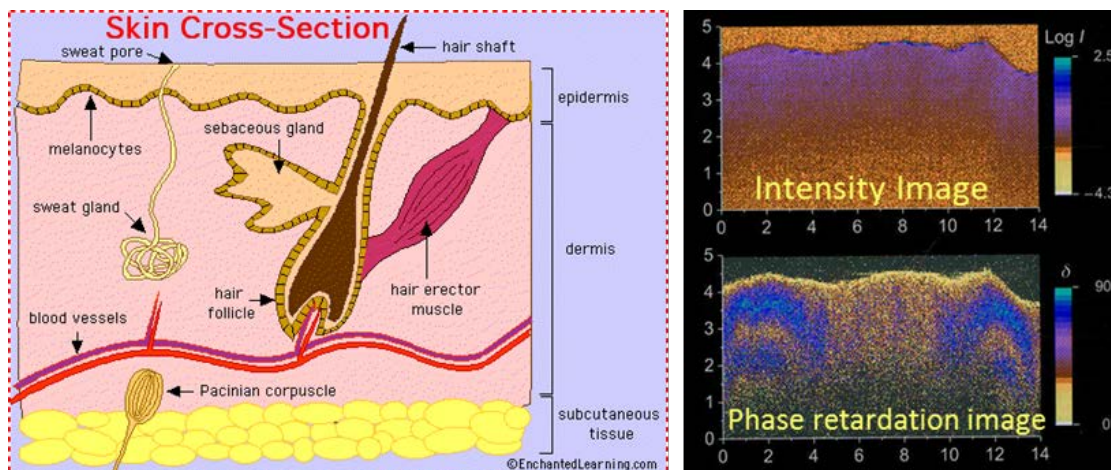


Fig. 6.5 OCT images of human skin based on the intensity and retardance of backscattered light.

Using our PSOCT, we can potentially carry out MM (Mueller matrix) imaging of many biological samples of clinical interest. The key focuses will be the study of ocular and dermal tissues. While a conventional OCT yield a single image, our technique will produce 16 distinct images for the layer of interest with abundant polarization information, enabling the detection of diseases more effectively. For example, in glaucoma, the loss of ganglion cells axon cause less birefringence, which can be observed directly from the change in the M_{34} and M_{43} Mueller-metric images; the disorder of fibrils in the glaucomatous nerve fiber layer results in higher depolarization, which is reflected by the M_{22} Mueller-metric images.

Specifically, we will carry out the following tasks:

Task 1: Build a data base of MM images of ocular tissues. For this task, we will first use ex vivo rabbit and monkey eyes, to be obtained from a commercial vendor. In addition, we will use epi-

ocular human tissue equivalents, to be obtained from a company such as MatTek.

Task 2: Build a data base of MM images of dermal tissues. For this task, we will use in vitro 3-D human epithelial tissue equivalents, also to be obtained for a company such as MatTek.

Task 3: Build a data base of MM images of basic human biological units (such as collagen), also to be obtained from a commercial vendor.

Task 4: Develop a basic protocol for employing the data bases mentioned above for further clinical studies aimed at detecting relevant diseases.

We expect that the complete PSOCT system, capable of producing 16 MM images of each layer, will prove to be a very robust and rapid technique for mapping out detailed morphological structures of clinical interest. Moreover, with the ability to detect depolarized light, the PSOCT will be useful in detecting early-stage diseases characterized by multiple-scattering depolarization, as well as identifying the presence and development of diseases. Specifically, we expect the PSOCT to be used in the following applications:

1. Examine the retina and the retinal structures such as the retinal nerve fiber layer, fovea and the retinal pigment epithelium.
2. Examine the extent of retinal defects or abnormalities caused by various eye diseases or trauma such as macular degeneration and retinal detachment.
3. Identify the presence of anomalies that may indicate the onset of skin cancers or other maladies.
4. Evaluate the effectiveness of treatments to diseases by monitoring tissue changes under therapy.

Chapter 7 Polarimetric Laser Radar (LADAR)

7.1 Introduction

Radar systems range from the simple ones (e.g., the ones used for motion detection) to more complex systems (e.g., the ones designed to detect, track, and identify objects at great distances; to assist the controlling of aircraft at airports; and to perform surveillance for in-port threat defense and shipboard protection systems.)^{71,72,73} Yet they all operate on the same simple principles: If a target is present when an electro-magnetic wave is radiated, the wave gets scattered by the target. The scattered wave is then detected by the radar receiver, and information about the target can be inferred. Regular radar systems may be classified as continuous wave (CW) sourced or pulse sourced. The CW radar, in its simplest form, transmits and receives single-frequency sinusoidal electromagnetic wave. The CW radar is able to measure the radial velocity of a target produced by the Doppler effect, but not the target distance. On the other hand, the pulse radar can estimate the distance to a target by measuring the time for a short pulse to travel between the transmitter/receiver and the target. The pulse generally consists of cycles of sinusoidal wave at certain frequency. Therefore, the relative motion between the target and the radar due to the Doppler effect can also be measured based on the frequency shift.

Laser radar, also referred to as Ladar or Lidar, uses laser pulses usually invisible to the eye to measure the distance to a target and its other properties. The first generation of Ladar's did not take the polarization-altering properties of a target into account. However, scientist quickly discover that the capabilities of a ladar imaging system can be enhanced significantly if the

incoming signal can be analyzed polarimetrically^{74,75,76,77,78}. Polarimetric imaging technique takes advantage of the fact that a given object emits and scatters light in a unique way depending on its polarimetric signature, which allows us to distinguish objects with different polarimetric properties, even if they have the similar reflectivity. Sinceolarization plays an essential role in the interaction of light and matter^{79,80,81,82,83}. By breaking down the light into independent polarization components, one can often reveal occluded surface information such as the composition, texture and roughness^{84,85,86,87,88}. As such, polarimetric imaging is utilized widely in many situations. For example, astrophysicists use polarimeters to measure the spatial distribution of magnetic fields on the surface of the sun⁸⁹. In the field of medical imaging, researchers analyze the polarization of light through coherence interferometry to yield the details about the optical properties of biological tissues. For defense applications, polarization imaging is often used to detect objects through smoke and obscurants such as vegetation or camouflage⁹⁰.

7.2 Fully Automated Polarimetric Ladar System

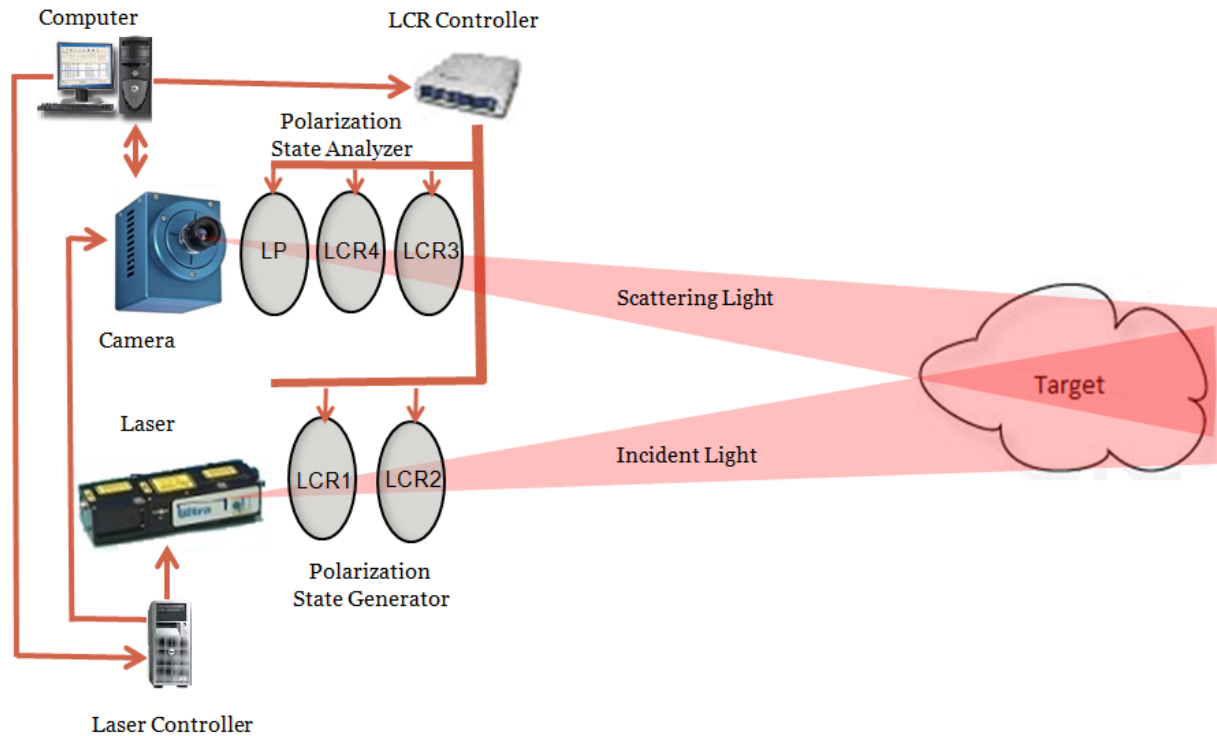


Fig. 7.1 Schematic illustration of the fully-automated imaging Polarimetric LADAR.

The basic configuration for the PLADAR is illustrated schematically in Fig.7.1. A pulsed laser at 1571 nm (pulse width = 6.5 ns) is used as the light source. The Stokes imaging occurs in the following order: At the pre-detection stage, the computer sends signals to the LCR controller as well as the laser controller. The LCR controller sets the LCR's in proper states. Once the LCR's are ready, the laser controller triggers the pulse and the camera simultaneously. The source laser is first sent through the PSG to produce the desired polarization before hitting the target. The back-scattered light transmits the PSA and is then detected by the infrared camera, which has a

CCD array of 300×256 pixels with $30 \times 30 \mu m^2$ pixel size. An exposure time window is applied to the camera to eliminate the unwanted background noise. The recorded intensity data array is transmitted back to the computer where the Stokes vector of each pixel is calculated simultaneously by a computer program, thus producing four distinct images, corresponding to the four Stokes parameters, for the input scene.

The operation speed of this PLADAR system is determined primarily by the response time of the LCR's. As mentioned in section 3, to analyze the Stokes vector, four independent measurements with different LCR phase delays are required. For the LCR's used in our experimental setup, it takes 15 ms for the retardation to increase from 0 to π , and 5 ms to relax from π to 0. The activation and relaxation of phase delay of each LCR in a measurement cycle is shown in Fig.7.2. Compared with the response time of the LCR's, the exposure window for light detection (1 μs for the camera in our setup) is negligible. The intensities I_1 , I_2 , I_3 and I_4 listed in Table-1 are recorded at times T_1 , T_2 , T_3 and T_4 , respectively. For our current setup, completing one cycle of 4 measurements for any input scene takes about 35ms, enabling the LADAR system to operate at video-rate.

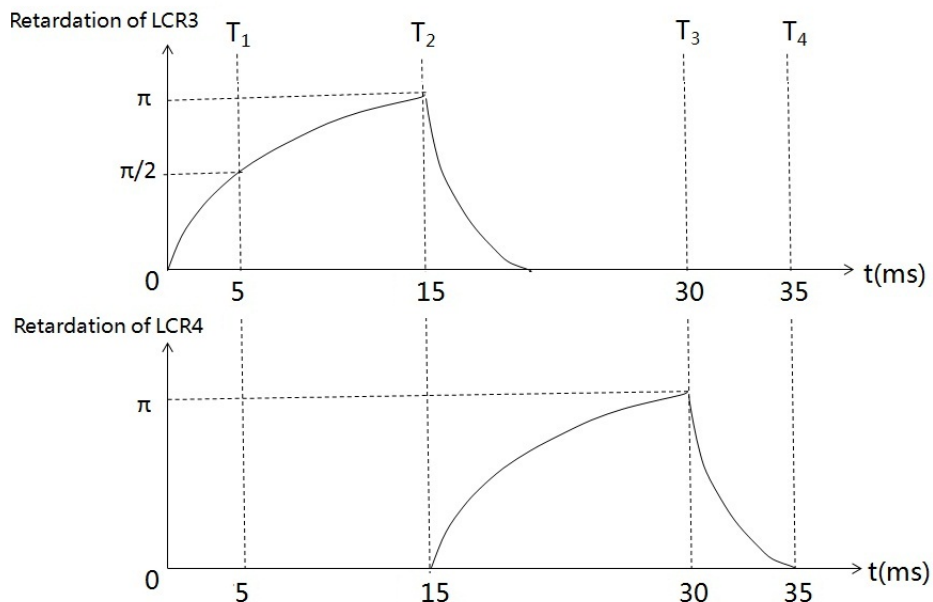


Fig. 7.2 The activation and relaxation of phase delay of each LCR in a measurement cycle.

7.3 Stokesmetric Imaging of Various Scenes

We first tested the PLADAR imaging system with an artificial scene comprising of optical elements with well-defined polarimetric properties. Specifically, we mounted a set of polarizer (at 45°) and a QWP on a piece of metal. Right circularly polarized light is generated using the PSG to illuminate this artificial scene. The resultant four Stokes vector images of the reflected light are shown in fig 7.3. The false red/blue color is imposed by the software to represent positive/negative value, respectively. Image (a), corresponding to the I element in the Stokes vector, contains only intensity-based information. Figures 'b' through 'd' are the Q, U and V images of the Stokes vector. Since our target objects are almost transparent, they can barely be distinguished from the background. However, because the tilted polarizer only selects

45° polarization to pass while the rest of the scene does not, it is easily distinct in the picture (c) containing only the U element. Similarly, because the QWP produces an extra π phase shift to the incident light in a round trip, the V image of it appears red, while the surroundings appear blue. Such an obvious contrast makes it possible to detect easily the almost transparent QWP in (a).

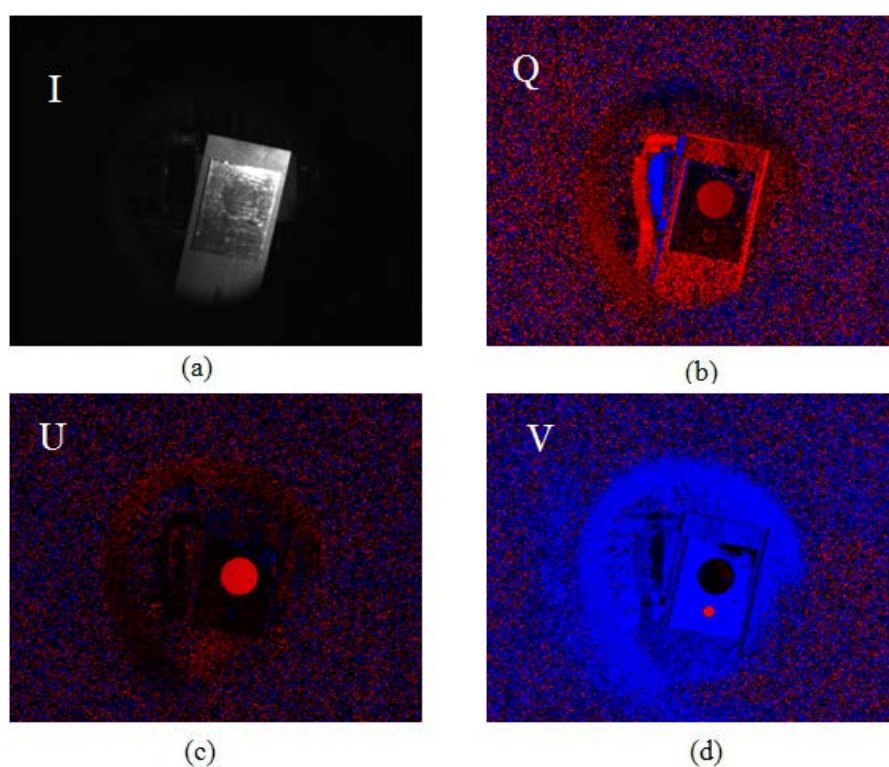


Fig. 7.3 Stokesmetric images of objects illuminated by right circularly polarized light.

After validating the capabilities of the automated PLADAR system, we used it to capture the Stokesmetric images of targets merged in more complicated scenes. Fig.7.4 shows a sample image set obtained for one such scene. We imitated the scene of a harbor by placing model boats on still water. A crystal is placed between two windows of the boat and a transparent tape is

attached to the body of the boat to form the phrase “work boat”. As can be seen, both the crystal and the letters can hardly be recognized from Fig.7.4 (a). However, image (c), corresponding to the U vector (containing purely 45° polarized light) clearly depicts the crystal due to its birefringence. The word “work boat” is also readable from image (c) from the body of the boat because of its different polarimetric signature from the surroundings. This ability to identify and distinguish various surfaces with a very high contrast makes the PLADAR a promising tool for surveillance and tracking applications. Note that for this imaging system, the angle of view (AOV) is primarily determined by the dimension of the CCD sensor and the effective focal length (EFL) of the camera. In our current setup, the $9 \times 7.7 \text{ mm}^2$ CCD sensor area and 16mm EFL of the relay lenses yield an AOV of 31.5° and 27.0° in the horizontal and vertical directions, respectively. The AOV can be further enhanced by increasing the size of the CCD for applications such as the wide-area surveillance.

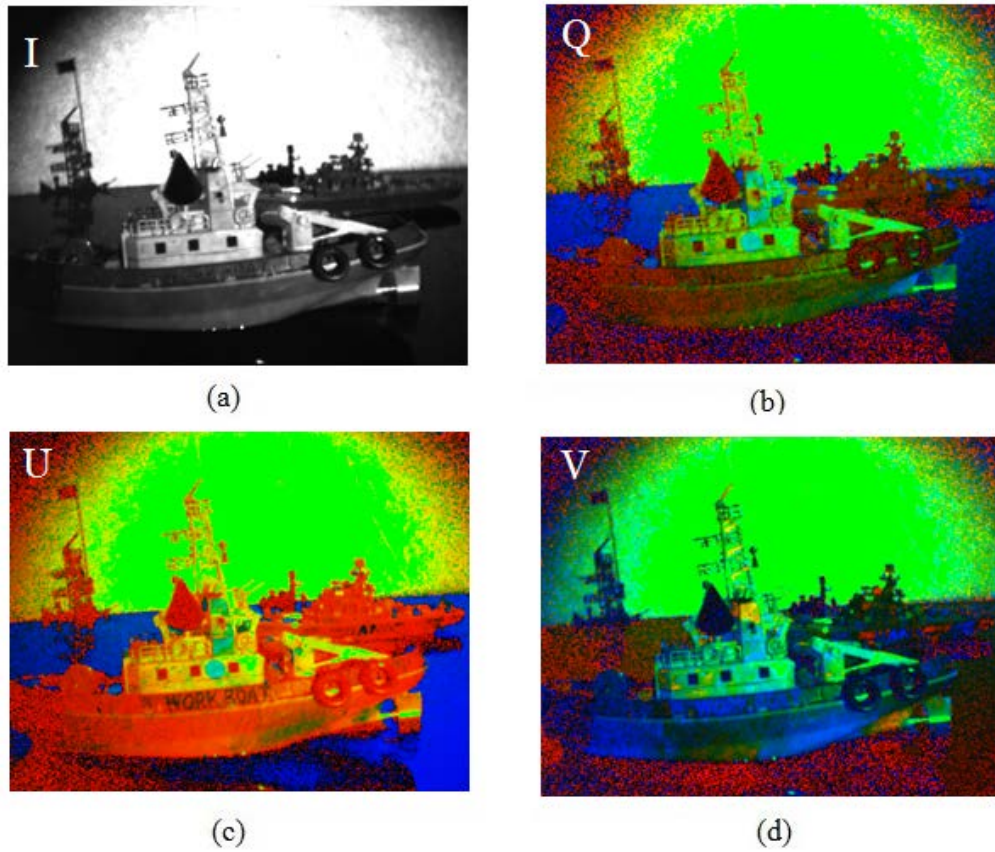


Fig. 7.4 Stokesmetric images produced under right circularly polarized light, for an artificial harbor.

By measuring the Stokes parameter images for a set of different input polarizations states, it would be possible to produce the full set of Muellermetric images, in a manner similar to what we have demonstrated recently for a polarimetric optical coherence tomography system [70].

Chapter 8 White Light Cavity (WLC) based on superluminal effect

8.1 Introduction

White light cavity (WLC) has a broader line width without loss of a build-up factor than an ordinary cavity with the same finesse^{91,92}. Such an enhanced line width is an essential property to apply WLC to optical detection, sensing and communication: For example WLC increases the sensitivity enough to detect the extremely weak side band signal produced by gravity waves without restricting the detection bandwidth^{93,94}. For a data buffer system, the high transmission of WLC over a broad enough spectral range to encompass the data pulse spectrum has been proposed as a data buffer system. It shows an enhanced delay time bandwidth product (DBP) overcoming constraints encountered by conventional buffer systems. WLC effect in a laser cavity was proposed for hypersensitive rotation sensing wherein the sensitivity of the lasing frequency to displacement was enhanced on the order of 10^5 higher than a conventional laser⁹⁵.

One way to realize the WLC is through filling the cavity with negative dispersion material as shown in Fig. 8.1. Such a cavity resonates over a frequency range that is far wider than that of the empty cavity, without a reduction in the cavity build-up factor. Techniques⁹⁶ to create negative dispersion over a limited frequency range have been demonstrated using dual stimulated Brillouin scattering (SBS) or dual stimulated Raman scattering (SRS) in an optical fiber. A cavity containing such a fast-light medium can be employed to realize a data buffering system

that circumvents the typical delay-bandwidth constraint encountered in a conventional data buffer based on slow light techniques.

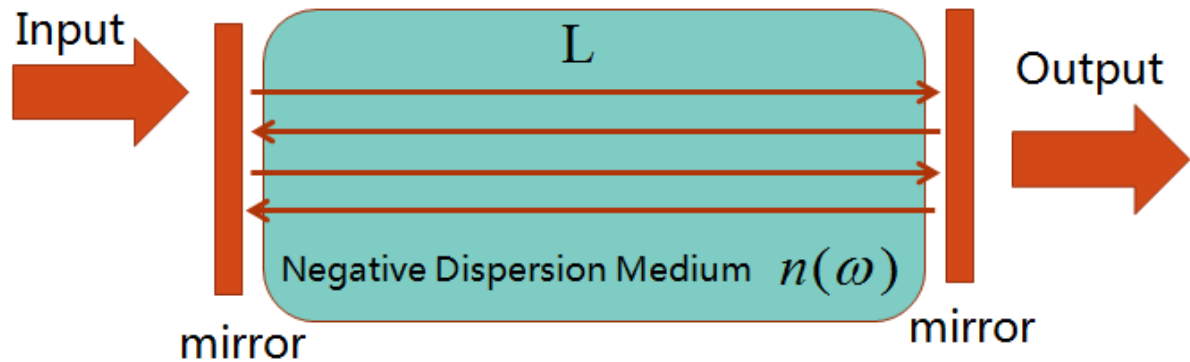


Fig. 8.1 WLC filled with Negative Dispersion Medium

For application to telecommunication systems, it would be convenient to realize such a device using fiber optic resonators. As we know, Krammer-kronig relationship indicates that a negative dispersion is usually associated with loss. However, in a dual-gain scheme, where the valley between the gain peaks can be viewed as a “loss”, the index at the center of the valley has a negative dispersion. In this chapter, we present the results of our efforts towards realizing a passive WLC in a fiber resonator, using dual gain peaks for producing the negative dispersion, thus achieving negative dispersion at the center of the resonance frequency, as shown in Fig. 8.2. Specifically, we demonstrate the basic functionality of a WLC in this system, and identify the conditions to achieve a WLC suited for high-speed data buffering.

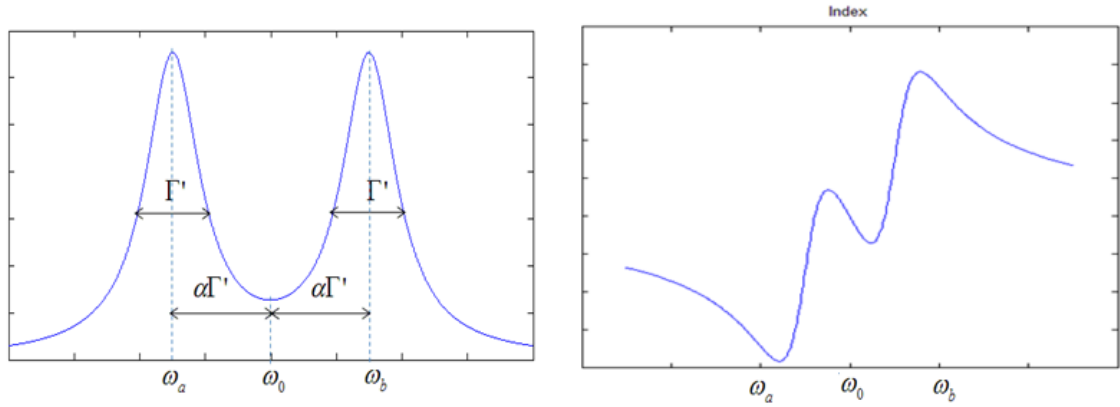


Fig. 8.2 The dual-gain scheme to realize negative dispersion.

8.2 Theoretical Model and Experimental Configuration:

In order to illustrate the concept of the WLC produced by Brillouin pumps, it is useful to consider first the model for an optical field propagating in an optical fiber resonator. Fig.8.2 shows such a resonator, which consists of a 2X2 coupler and a fiber loop. If we assume the coupler to be lossless, the relations between the input and output fields (a_1 and b_1) are related to the fields inside the loop (a_2 and b_2) are given by

$$\begin{bmatrix} b_1 \\ b_2 \end{bmatrix} = \begin{bmatrix} \sqrt{1-K} & j\sqrt{K} \\ j\sqrt{K} & \sqrt{1-K} \end{bmatrix} \begin{bmatrix} a_1 \\ a_2 \end{bmatrix} \quad (8.1)$$

where K is the intensity coupling coefficient. The relationship

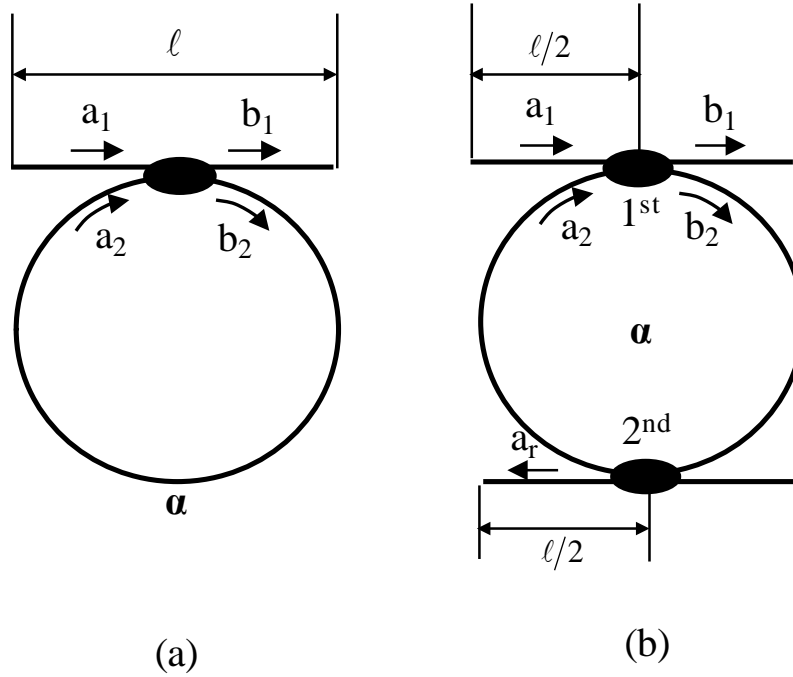


Fig. 8.3 Schematics of (a) fiber ring resonator, (b) ring resonator coupled to a single mode fiber

between a_2 and b_2 can be expressed in terms of the round-trip transmission factor, α , and the round trip phase shift, θ :

$$a_2 = \alpha e^{j\theta} b_2 \quad (8.2)$$

Using Eqs.(8.1) and (8.2), we can derive the power transmission ratio, $|b_1/a_1|^2$ and the inserted power ratio, $|b_2/a_1|^2$:

$$\left| \frac{b_1}{a_1} \right|^2 = \frac{\alpha^2 + |t|^2 - 2\alpha|t|\cos\theta}{1 + \alpha^2|t|^2 - 2\alpha|t|\cos\theta} \quad (8.3a)$$

$$\left| \frac{b_2}{a_1} \right|^2 = \frac{1 - |t|^2}{1 - 2\alpha|t|\cos\theta + \alpha^2|t|^2} \quad (8.3b)$$

where t is the complex amplitude transmission coefficient ($K+T=1, T=|t|^2$). In what follows, we will use $|a_1|^2=1$. Next, consider θ in the presence of bi-frequency Brillouin pumps. The probe at frequency ω propagates the ring resonator whose circumference is L . The phase shift resulting from the propagation is written as kL . The wave vector amplitude of the probe is represented by k . To observe the WLC effect, the bi-frequency pumps are used to produce dual gain peaks via SBS process in the fiber resonator, yielding negative dispersion between the gain peaks. Since the gain medium fills the whole length of the resonator, the condition necessary for realizing an ideal WLC is a vanishing group index: $n_g=0$. In the unsaturated domain, where power broadening of the SBS process is ignored, the Brillouin dual gains α_{Br} and the phase β are given by

$$\alpha_{Br} = \frac{1}{2} \left[\frac{g_0 I_{P1}}{1 + 4(\nu - \nu_B - \Delta)^2 / \Gamma_B^2} + \frac{g_0 I_{P2}}{1 + 4(\nu - \nu_B + \Delta)^2 / \Gamma_B^2} \right] \quad (8.4)$$

$$\beta = \frac{g_0 I_{P1} (\nu - \nu_B - \Delta) / \Gamma_B}{1 + 4(\nu - \nu_B - \Delta)^2 / \Gamma_B^2} + \frac{g_0 I_{P2} (\nu - \nu_B + \Delta) / \Gamma_B}{1 + 4(\nu - \nu_B + \Delta)^2 / \Gamma_B^2} \quad (8.5)$$

where ν_B , g_0 , and Γ_B are Brillouin frequency, gain coefficient, and linewidth, respectively. I_{P1} and I_{P2} are pump intensities per unit area. We consider the equal intensity so that $I_{P1} = I_{P2} = I_P$ (W/m^2). 2Δ corresponds to the gain separation. The phase shift after one round trip can be written as $kL = n_f \omega L / c + \beta L$, where n_f and c are the mean index of the fiber and speed of light, respectively. The gain factor after each pass through the resonator loop, in the presence of the dual gains, is given by $\alpha \exp(\alpha_{Br} L)$, which we will call the “modified gain.” k is expressed, via

Taylor expansion, around the cavity resonance frequency ω_0 as $k = k_0 + k_1(\omega - \omega_0) + k_2(\omega - \omega_0)^2 + k_3(\omega - \omega_0)^3$ where $k_0 = n_f \omega_0 / c$, $k_1 = n_f / c + d\beta/d\omega|_{\omega_0}$ and $k_3 = (1/6)d^3\beta/d\omega^3|_{\omega_0}$. Assuming $\omega_0 = \nu_B$, the second order term vanishes (i.e. $k_2=0$) due to the antisymmetric dispersion profile around ω_0 . Replacing θ with kL , and α with $\alpha \exp(\alpha_{Br}L)$ into Eq.(8.3a), we obtain the transmitted power spectrum of the fiber-based WLC, as shown in Fig. 8.4.

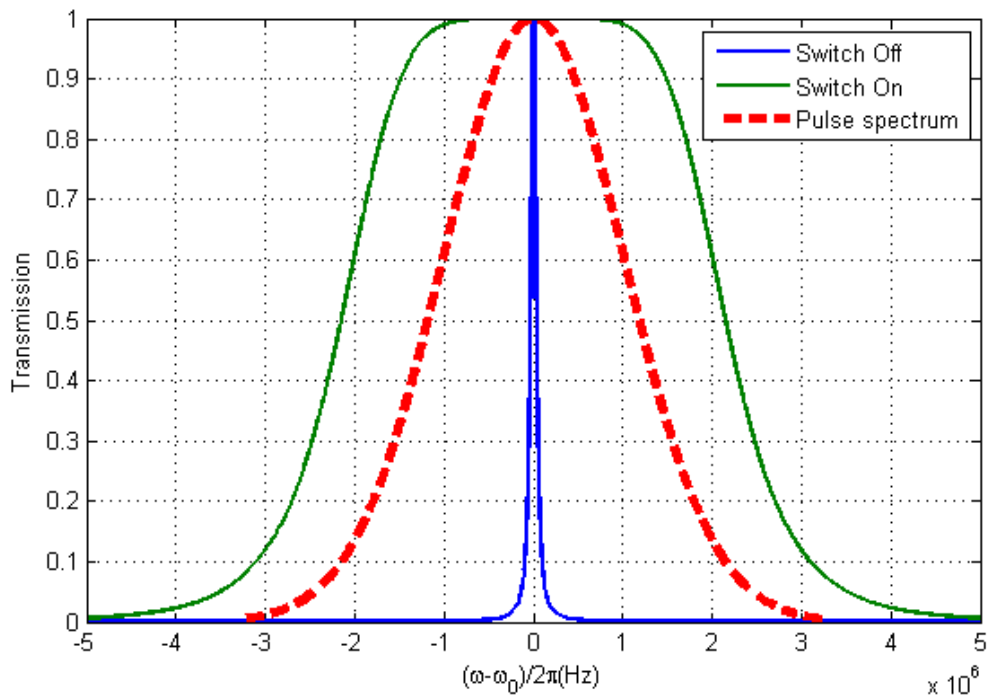


Fig. 8.4 WLC with the fast light medium switched on and off

Chapter 9 Optical data buffer based on ring WLC

9.1 Introduction

In Chapter 8, we described the principles of a WLC. In this chapter, we present the design of an optical data buffer system based on the WLC, where the white light cavity effect is produced by dual stimulated Brillouin scattering. The system consists of a pair of fiber optic white light cavities placed in series. The delay time can be controlled independently of the bandwidth of the data pulses. Furthermore, we show how the bandwidth of the system can be made as large as several times the Brillouin frequency shift. We also show that the net delay achievable in such a buffer can be significantly larger than what can be achieved using a conventional recirculating loop buffer.

In recent year, slow light in optical fibers has been of interest due to its applicability to current optical devices for fiber optic communication such as optical buffers, optical delay lines and fast memory access^{97,98,99,100,101}. However, the amount of delay achieved is typically too small to be of interest for most applications. We have shown that this limitation can be overcome by using fast-light, in a manner that is rather counter-intuitive¹⁰². Briefly, this approach makes use of so-called white light cavities (WLCs). A WLC is a cavity containing a fast-light medium, tuned so

that negative dispersion causes the wavelength to become independent of frequency over a certain spectral range. As such, it resonates over a broader spectral range compared to an empty cavity of equal length and finesse, without a reduction in the cavity build-up factor¹⁰³. The buffer system is composed of two WLCs as well as an intervening zone of dispersion-free propagation. When the fast-light medium is deactivated, the WLC acts as a narrow-band cavity, which reflects a high-bandwidth pulse stream. However, when the fast-light medium is activated, the data stream passes through the WLC. Using these properties, the data stream can be trapped between the two WLCs for a duration that is limited only by the residual transmission through the cavity in the narrow-band mode and the length of the intervening zone. As shown in ref [96], such a buffer can slow down a data pulse for a duration that is several thousand times longer than the pulse with virtually no distortion. However, for many reasons, a buffer of this type based on free space components is likely to be impractical, especially for telecommunication. In this paper, we show how to realize such a buffer using WLC's based on fiber resonators, with an optical fiber forming the intervening path.

The buffer presented in this paper has some formal similarity to the dark-state based scheme employing a pair of micro-ring cavities^{104,105,106,107}. However, the fundamental physical process is quite different, since the concept presented here makes use of anomalous dispersion. We also note that our buffer is similar in configuration to the feedback buffer employing a recirculation loop^{108,109,110,111}. The key difference between our scheme and the feedback buffer is that once the data is in the loop, it is almost completely isolated. During each circulation through the loop, the attenuation is due to a vanishingly small coupling to the WLC and the residual transmission

loss inherent to the fiber. As such, there is no need for an amplifier in the loop. A single-stage amplification upon release from the buffer is sufficient to restore the signal level to the input value. Elimination of an intra-loop amplifier entails absence of noise due to amplified spontaneous emission, so that for a given level of signal to noise ratio (SNR), a much larger number of loop circulations can be allowed. Furthermore, absence of intra-loop amplification reduces the energy cost of the buffer.

9.2 Fiber-based Fast-light Data Buffer

In chapter 8 we showed a model of WLC based on the negative dispersion produced in a fiber. In order to quantify the dispersion in the fiber loop for a real case, we express $n(\omega)$ in terms of a Taylor expansion about ω_0 :

$n(\omega) = n_0 + (\omega - \omega_0)n_1 + (\omega - \omega_0)^3 n_3$, $n_1 = dn/d\omega|_{\omega=\omega_0}$, $n_3 = (1/6)dn^3/d\omega^3|_{\omega=\omega_0}$ where n_0 is the mean index of the fiber.

Fig. 8.4 displays the numerical simulations for $|a_r/a_i|^2$ of an ideal fiber-coupled resonator with no dispersion (dashed line) and with strong negative dispersion (solid line, $n_1 < 0$, $n_3 \neq 0$). Of course, all fibers have some degree of dispersion. However, dispersion in a typical single-mode fiber is negligible compared that induced by Brillouin pumps in our system, thus justifying our assumption of $n_1 = 0$, $n_3 = 0$ for the ideal resonator. For simplicity, we assume unit input intensity $|a_i| = 1$ and no internal loss ($\alpha = 1$). We choose n_1 to fulfill the ideal white Light Cavity (WLC) condition. For the configuration presented in Fig.8.3(b), the length of the dispersive medium is assumed to be equal to that of the ring resonator. In that case, the ideal WLC condition requires

$n_g = 0$, where n_g is the group index of the dispersive fiber. Next, n_3 is adjusted so that the WLC linewidth becomes finite. We have chosen $k_1 = k_2 = 0.01$, $\ell = 1$, $n_0 = 1.45$ and $L = 10.6897$ where L and ℓ are in meter.

It is instructive here to discuss in some detail the values of the parameters necessary to produce the WLC condition: i.e. $n_g = 0$. Specifically, we consider bi-frequency Brillouin pumps with a frequency separation $S = 2 * \text{FSR}$ where FSR is the free spectral range of the cavity. Using the data presented in ref.¹¹², with a Brillouin gain bandwidth $\Delta v_B \approx 25\text{MHz}$, we find the Brillouin coefficient to be $g_0 = 1.01885 \times 10^{-11} \text{m/W}$. By considering the same cavity parameters as used in Fig.2, and assuming the pumps to be resonant in the cavity, we find the input power of each Brillouin pump to be $\sim 1.3\text{W}$. In the simulation, we have used Lorentzian dual gains, with the pump frequencies given by $\nu_{\pm} = \nu_0 - \nu_B \pm 0.77\Delta v_B$ where $\nu_0 = \omega_0 / 2\pi$ is the frequency corresponding to a wavelength of 1550nm, and ν_B is the Brillouin frequency.

As can be seen from Fig. 9-2, the linewidth of WLC is expanded, compared to the ordinary ring resonator associated with $n(\omega) = n_0$. It should be noted that this broadening occurs without a reduction in the cavity build-up factor. If the WLC linewidth is broad enough for the pulse spectrum to be under the resonant spectral region of WLC, then the input signal will transmit without loss or distortion.

Next, we consider the propagation of a pulse through such a fiber-coupled resonator. Equation (7) represents the transfer function between the input and the output. The transfer function is denoted as H_0 for the resonator without dispersion [$n(\omega) = n_0$] and as H_{WLC} under the white light

cavity condition [$n(\omega) = n_0 + (\omega - \omega_0)n_1 + (\omega - \omega_0)^3 n_3$]. To find the group velocity associated with the system, it is important to express the group index in terms of $\angle H_{0/WLC}$, the phase shift induced during propagation through the resonator. The phase contribution resulting from the propagation through the whole system (fiber plus cavity) can be expressed as $(\omega n_{eff} \ell) / c = (n_0 \omega \ell) / c - \angle H_{0/WLC}$, where we define n_{eff} for the effective refractive index provided by the resonator. By the definition of the group index, obviously $n_{g(resonator)} = n_{eff} + \omega (dn_{eff} / d\omega)$ where $n_{g(resonator)}$ is the group index of the whole system (and not the group index of the medium). Thus, $n_{g(resonator)}$, evaluated at $\omega = \omega_0$, a resonance frequency of the cavity centered between the two Brillouin gain peaks, is given by¹¹³

$$n_{g(resonator)} = n_0 - \frac{c}{\ell} \frac{d \angle H_{0/WLC}}{d\omega} \quad (9.1)$$

Note that the pulse distortion would be characterized by $\Delta T \approx - (d^2 \angle H_{0/WLC} / d\omega^2) \Delta \omega$.

It is instructive to compare $\angle H_{0/WLC}$ to the phase of b_1/a_1 , denoted as $\angle H_{a_1, b_1}$ in Fig. 9.1(a). Fig. 9.1(b) graphically shows the output pulses resulting from propagation through the system, in the presence of the cavities associated with H_0 (dashed) and H_{WLC} (circles) as well as the pulse after propagating a distance ℓ through a fiber only without dispersion (solid). For illustration, we chose the input pulse to be of the form $S_{in}(t) = \exp(-t^2/t_0^2) \exp[j(\omega_0 + \xi)t]$. Here, t_0 is chosen so that $\Delta v_{pulse} = 10 \Delta v_{cavity}$, where $\Delta v_{pulse} = 1/t_0$ and Δv_{cavity} is the full-width-half-maximum (FWHM) of the ordinary resonator. Fourier transform of $S_{in}(t)$ leads us to $\tilde{S}_m(\omega) = t_0 / \sqrt{2} \exp[-\{(\omega - \omega_0 - \xi)t_0\}^2 / 4]$. Applying the convolution theorem, we obtain the amplitude of the output pulse as:

$S_{out}(t) = 1/\sqrt{2} \int_{-\infty}^{\infty} S(\omega) \exp(-jk_0 \ell) H_{0/WLC}(\omega) \exp(j\omega t) d\omega$, where $k_0 = n_0 \omega \ell / c$. We simply set $H_{0/WLC} = 1$ when

the field propagates in the fiber only.

Note that there is a discontinuity accompanied by a phase leap at $\omega = \omega_0$ as illustrated in Fig. 9.1(a). Of course, such a discontinuity disappears when the sources of all losses as well as the finite bandwidth of a real signal are taken into account. However, under the assumptions used here, this result can be explained as follows, in analogy with the critically coupled microresonator presented in ref¹¹⁴, for example. Specifically, a critically coupled resonator shows a π -phase leap on resonance. For the resonator considered here, we have used $\alpha = 1$, $k_1 = k_2 = 0.01$ so that $\alpha \sqrt{1-k_2} = \sqrt{1-k_1}$. This means that the transmission factor between b_2 and a_2 ($\alpha \sqrt{1-k_2}$) matches the transmission coefficient of the first coupler ($\sqrt{1-k_1}$), corresponding to critical coupling. Thus, $\angle H_{b1,a1}$ shows the π -phase leap at resonance. The second coupler, which is identical to the first one, is also critically coupled. Thus, the π -phase leap occurs twice, resulting in a discontinuity of 2π for $\angle H_{0/WLC}$.

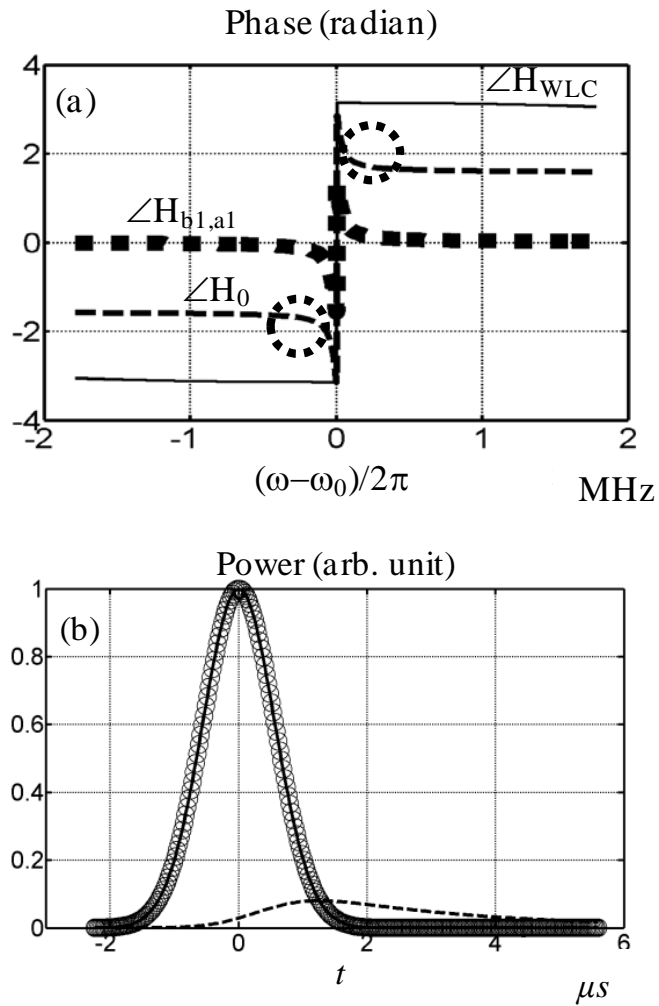


Fig. 9.1 (a) Phases associated with the transfer functions of the resonator displayed in Fig. 1(b).

$\angle H_{b1,a1} = \arg(b_1/a_1)$, $\angle H_0 = \arg(a_0/a_1)$ in the absence of WLC effect, and $\angle H_{WLC} = \arg(a_0/a_1)$ for WLC, with $n_1 = -1.192 \times 10^{-15} / \text{rad}$, $n_3 = 1.223 \times 10^{-32} / \text{rad}^3$ (b) Reference pulse after propagating in a fiber of length ℓ (solid line) and the outputs associated with H_0 (dashed line) and H_{WLC} (circles). The output in the presence of the WLC effect is essentially overlapped with the reference.

We explain the output pulses illustrated in Fig. 9.1(b) with the aid of Fig. 9.1(a). According to (9-1), the negative slope of $\angle H_0$ suggests $n_{g(\text{resonator})} > n_0$. By setting $\xi = 0$, we have chosen the input pulse to have the carrier frequency equal to ω_0 . As such, the pulse lies within the slow light zone. Since $\Delta v_{\text{pulse}} = 10\Delta v_{\text{cavity}}$, most of the pulse spectrum is under the spectral region of $|H_0| = 0$. As a consequence, the output associated with H_0 is delayed and attenuated, as can be seen in Fig. 9.1(b). For the case of WLC, we consider $\xi = 1.5/t_0$ so as to ensure that the pulse spectrum is mostly outside the region where $\angle H_{\text{WLC}}$ leaps by 2π . Thus, over the spectrum of the pulse, we have $|H_{\text{WLC}}| \approx 1$, $d\angle H_{\text{WLC}}/d\omega \approx 0$ and $d^2\angle H_{\text{WLC}}/d\omega^2 \approx 0$, so that $n_{g(\text{WLC})} \approx n_0$, according to (9-1). As a result, the output of WLC is not advanced compared to the reference pulse propagating the distance of ℓ through a bare fiber; rather, these outputs are virtually superimposed on each other, as illustrated in Fig. 9.1(b). This behavior can also be understood physically noting that $n_g = 0$ for the fiber inside the resonator under the ideal WLC condition. Thus the pulse propagates in the resonator with the speed of $v_g \gg c$, thereby spending very little time inside. Of course, under realistic condition, such a propagation does not violate special relativity or causality¹¹⁵. In ref¹¹⁶, we describe in detail the exact behavior of a pulse inside a cavity loaded with an anomalously dispersive medium, under a range of conditions, including $n_g = 0$.

In analogy with the previously proposed Fabry-Perot(FP) buffer system, we now present the design of a fiber-based data buffer, as shown in Fig. 9.2. We assume that a bi-frequency Brillouin pump creates a negative dispersion in a ring resonator to produce the WLC effect, in a manner analogous to the previous WLC demonstration where a bi-frequency Raman pump was

used to produce dual Raman gain peaks as in ref [97], yielding a negative dispersion between the peaks. Here, each Brillouin pump produces a Lorentzian gain peak for the counter-propagating probe. As we discussed earlier, we can reach the WLC condition for a gain separation of $1.54\Delta v_B$ ($\Delta v_B = 25\text{MHz}$), if we use 1.3W input power for each Brillouin pump. In the spectral region between these two gain peaks, the probe experiences negative dispersion. From reference [97], we note that $\Delta v_{WLC} = \alpha\delta^{2/3}$ where Δv_{WLC} is the WLC bandwidth, δ is the gain separation, and α is a constant of proportionality, which is close to unity for Lorentzian gain peaks. Thus, we expect $\Delta v_{WLC} = 11.4\text{MHz}$. The WLC on the left (LWLC) is connected to the WLC on the right (RWLC) through fiber spools to construct a closed loop where a pulse would be trapped.

Later, we discuss how to increase Δv_B by using Gaussian Brillouin gain. From this discussion, we will find that one can increase δ up to the order of GHz, while keeping $n_g=0$ between the gains. In doing so, we can get a value of Δv_{WLC} in the GHz regime, because the relation $\Delta v_{WLC} = \alpha\delta^{2/3}$ holds for Gaussian gain peaks as well, with the value of α again being close to unity. The exact value of α for either shape of the gain peaks can only be determined numerically or experimentally.

For a data pulse and the WLCs, we use the same parameters as considered in Fig. 9-3. The operating scheme to delay the pulse without distortion is similar to that presented in [6]. When the pulse enters from left, we turn on the bi-frequency Brillouin pumps to activate the WLC effect in LWLC. Thus, the pulse transmits through the resonator with no distortion, as shown in Fig. 9-3(b). Once the pulse has left LWLC, we turn off the WLC effect. Now, the pulse is loaded and circulates inside the trapping loop.

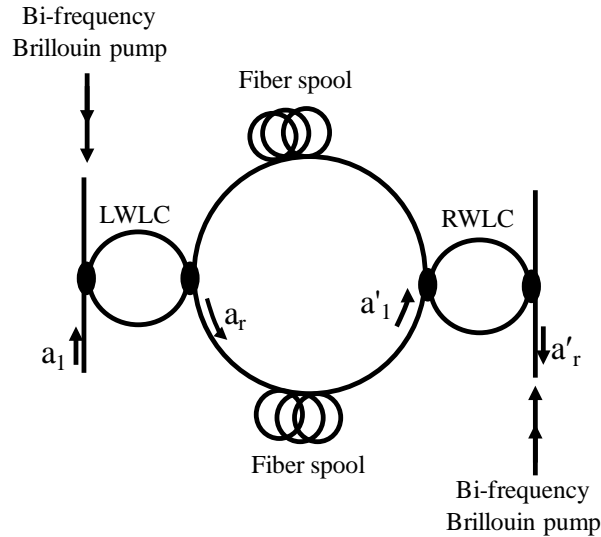


Fig. 9.2 Schematic illustration of the fiber-based data buffer system, employing bi-frequency Brillouin pumps. LWLC: Left White Light Cavity; RWLC: Right White Light Cavity.

To consider power loss during the circulation, it is important to note that the carrier frequency of the pulse is shifted by $\xi = 1.5/t_0$ from the resonant frequency, ω_0 , of the bare cavity (i.e., without the WLC effect). If it is not shifted, the pulse spectrum would include the transmission window of the bare cavities. In that case, the spectral component within this window would leak out through the bare cavities. With the carrier frequency shifted, LWLC as well as RWLC acts as a simple coupler, with an intensity coupling coefficient of $k_1 = k_2 = 0.01$. On each bounce, the pulse is reflected, with a small transmission loss due to this finite coupling coefficient.

Once we are ready to extract the pulse from the trapping loop, we activate the WLC effect in RWLC. On arriving at RWLC, the pulse passes through it with neither attenuation nor distortion.

To find a full transfer function to describe the data buffer system, we consider the amplitude transfer characteristics $H_{lr} = a_r/a_l$ ($H_{lr'} = a'_r/a'_l$) where H_{lr} ($H_{lr'}$) denotes the transfer function of LWLC (RWLC). After N multiple round trips inside the trapping loop, a_r is related to a'_l by

$$H_{lr'} = \left(\sqrt{1-k_1} \sqrt{1-k_2} \right)^N e^{-jk_0 \frac{2N+1}{2} L_2} 10^{-\frac{\alpha}{20}} \quad (9.2)$$

where L_2 is the length of the trapping loop and $k_0 = \omega n_0/c$. Here, α represents the total attenuation due to the propagation through the loop. A conventional single mode fiber for 1550 nm exhibits an attenuation loss of ~ 0.2 dB/km so that $\alpha = 0.2 \times (N+1/2)L_2$. The time elapsed in the loop represents the system delay: $\tau_d = [n_0(N+1/2)L_2]/c$.

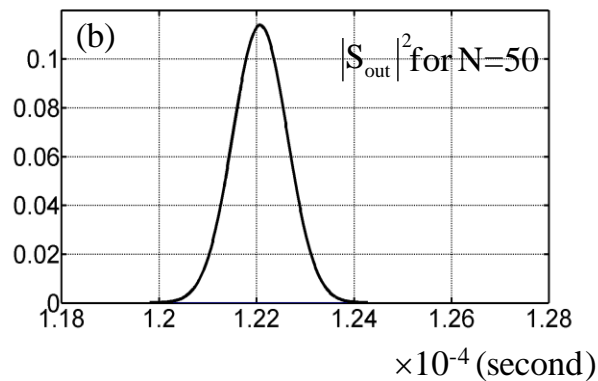
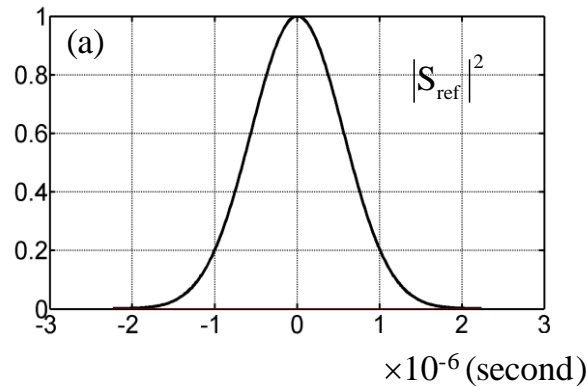


Fig. 9.3 Output pulses from the fiber-based buffering system: (a) reference pulse, (b) pulse after 50 round trips inside the trapping loop.

Fig. 9.2 illustrates the reference pulse propagating a distance ℓ through a fiber, as well as the output from the data buffer for $N=50$. The reference pulse can be written as

$$S_{ref}(t) = 1/\sqrt{2} \int_{-\infty}^{\infty} \exp(-jk_0\ell) S(\omega) \exp(j\omega t) d\omega.$$

Using H_{lr} , $H_{l'r'}$ together with (9.2), the output of the data buffer can be written as:

$$S_{out}(t) = 1/\sqrt{2} \int_{-\infty}^{\infty} \exp(-jk_0\ell) H_{total} S(\omega) \exp(j\omega t) d\omega \quad (9-$$

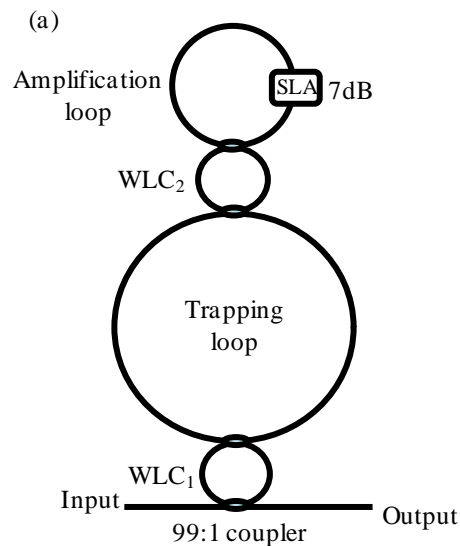
10)

where $H_{total} = H_{l'r'}(\omega) H_{r'l}(\omega) H_{lr}(\omega)$. Figs. 9.2(a) and 9.2(b) show that for $L_2 = 500$ the output pulse is delayed by 1.22×10^{-4} seconds compared to the reference. Fig. 9.2(b) indicates that the pulse delay is accompanied by no serious distortion, but an attenuation of about 9.3 dB (from 1 to 0.115). The attenuation per pass is 0.186 dB, which is the sum of attenuation due to transmission (0.1dB), plus a loss of 1% (0.043 dB) at each of the two couplers.

9.3 Fast-light Data Buffer vs Conventional Fiber Loop Data Buffer

The attenuation suffered in the storage loop can be compensated by using an optical amplifier. Such an amplifier could be added to the storage loop. However, since the loss per pass in the loop is very small and an amplifier would have an insertion loss much higher than the single pass attenuation, a better approach is to use a separate loop for the amplification. This is illustrated schematically in Fig. 9.3(a). Prior to the buffering process, both WLCs are inactive. The pulse

stream to be stored is inserted into the trapping loop by activating WLC_1 and deactivating it after the stream is fully loaded. We assume the perimeter of the trapping loop to be 0.5 km (same as the loop considered in Fig. 9.2). After 50 passes (with an attenuation of 9.3 dB), WLC_2 is activated and the pulse stream enters the amplifying loop. The amplifier in this loop is gated to provide a net amplification (amplifier gain minus the insertion loss of the amplifier) of 9.3 dB, restoring the original amplitude. We neglect the attenuation in the amplifying loop, which can be much smaller. Once the stream re-enters the trapping loop, WLC_2 is deactivated. This process is repeated M times after another 50 passes through the trapping loop.



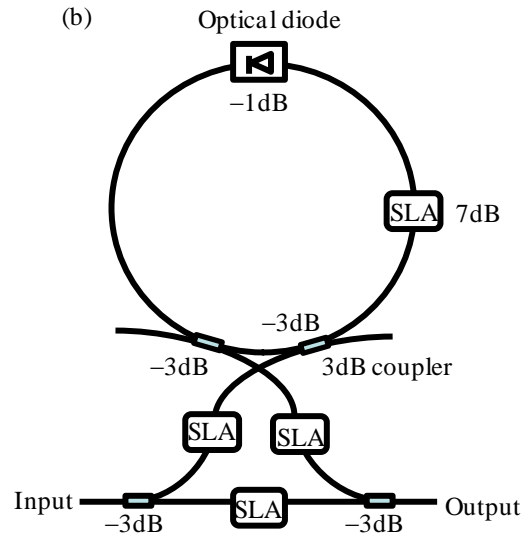


Fig. 9.4 Schematics illustration of (a) a WLC-based data buffer augmented by amplification, (b) a conventional recirculating data buffer [13]; SLA: Semiconductor Laser Amplifier; WLC_{1,2}: White Light Cavity_{1,2}. In Fig. 6(b), the optical diode acts as an isolator.

The number of times the amplification is applied, M , is limited by the fact that the signal to noise ratio (SNR) is degraded due to noise added during each pass through the amplification process. The actual reduction in SNR during each pass would depend on the type of amplification employed. The maximum allowable net reduction in SNR would depend on the SNR in the input pulse stream and the fidelity requirement of the system. As an example, we consider a case where M is limited to 100. The net delay achievable is then ~ 12.2 msec and the delay-bandwidth product for the input pulse used in Fig. 5 would be 10^4 . Obviously, if much shorter pulses are used (which would require a higher bandwidth WLC), the delay bandwidth product (DBP) can be correspondingly larger. For example, for a pulse width of 0.122 nsec (requiring a WLC linewidth of ~ 30 GHz), DBP would be 10^8 .

It is instructive to compare such a system with a conventional recirculating buffer. A typical implementation of such a buffer is illustrated in Fig. 6(b). Here, during each pass, there is a loss of 7 dB due to the two couplers and the isolator. The net gain (amplifier gain minus the insertion loss of the amplifier) provided by the amplifier in each pass is thus 7 dB. If all other parameters are comparable to the buffer shown in Fig. 6(a), then the maximum number of amplification for approximately the same reduction in SNR would be about 133 ($=9.3 \times 100/7$). The net delay achievable would be 0.33 msec. Thus, all else being equal, the delay time achievable for the buffer proposed here would achieve a delay of nearly 37 times larger than what can be achieved using a conventional recirculating buffer. This is attributable solely to the fact that the conventional buffer has a large loss (7 dB) per pass, while for the WLC buffer, the inherent loss per pass is much smaller (0.186 dB). The factor by which the WLC delay is larger is essentially a ratio of these two numbers. The relative advantage thus would become better as the loop perimeter becomes smaller and/or couplers with higher efficiency are employed.

Chapter 10 Optical data buffer based on Linearly Chirped Bragg Grating (LCBG)

10.1 Introduction

It is widely accepted that Bragg reflection from linearly chirped Bragg gratings (LCBGs) can compensate for a chromatic dispersion by reflecting different wavelengths at different location along the axis of the gratings^{117,118,119}. In this chapter, we studied the possibility of making use of such a dispersion-compensating property to construct a white light cavity (WLC). A pair of LCBGs is suggested as the reflectors of the cavity. The analytical and numerical analysis show that the reflection by a LCBG does not solely occur at the position where Bragg condition is reached. The accumulated effect of multiple scatterings at different locations inside the LCBG produces a positive group delay, preventing the WLC to be realized with simple LCBG.

In Chapter 8, we show that white light cavity (WLC) has a broader linewidth without loss of a build-up factor than an ordinary cavity with the same finesse. Such an enhanced linewidth is an essential property to apply WLC to optical detection, sensing and communication^{120,121,122}: For example WLC increases the sensitivity enough to detect the extremely weak side band signal produced by gravity waves without restricting the detection bandwidth. For a data buffer system, the high transmission of WLC over a broad enough spectral range to encompass the data pulse spectrum has been proposed as a data buffer system. It shows an enhanced delay time bandwidth product (DBP) overcoming constraints encountered by conventional buffer systems. WLC effect

in a laser cavity was proposed for hypersensitive rotation sensing wherein the sensitivity of the lasing frequency to displacement was enhanced on the order of $\sim 10^5$ higher than a conventional laser.

In WLC, the frequency dependent phase shift due to propagation delay is cancelled by tailoring a dispersion profile of the intracavity medium such that WLC condition is achieved: $n_g = 1 - L/\ell$ where L is the cavity length, and n_g and ℓ are the group index and the length of intracavity medium, respectively. In previous implementations, n_g is controlled by coupling a weak probe to a strong pump in non-linear media. However, such a probe-pump interaction scheme is not applicable when we need to use a high power probe, for example, ~ 40 Watt probe beam is used in the Advanced LIGO interferometer and then the pump would have to be even stronger to induce dispersion. Current material technology cannot provide a non-linear medium which holds such high power beams. A passive approach to the enhancement of the bandwidth of LIGO like interferometer was attempted by using two gratings placed in parallel; however, if one consider the geometrical optical path arising from the wavelength-dependent diffraction angle as well as the additional phase change associated with the spatial phase modulation of the gratings, it is then impossible to make the variation of the phase with respect to frequency become zero^{123, 124}. The essence of this constraint originates from the constant grating period. In ref.[124], if the grating period is a function of frequency i.e. $g \equiv g(\omega)$ rather than the constant, then the phase variation would become $d\Phi/d\omega = L(\omega)/c - D \tan\beta [dg/d\omega]$ implying that $d\Phi/d\omega$ could be zero with the appropriate choice of $dg/d\omega$.

10.2 White Light Cavity (WLC) condition

First, it is necessary to understand the condition needed in order to construct a passive WLC. As show in Fig.10.1, the basic scheme of the WLC is a variation of a regular Fabre-Perot interferometer with additional phase generated by the reflectors.

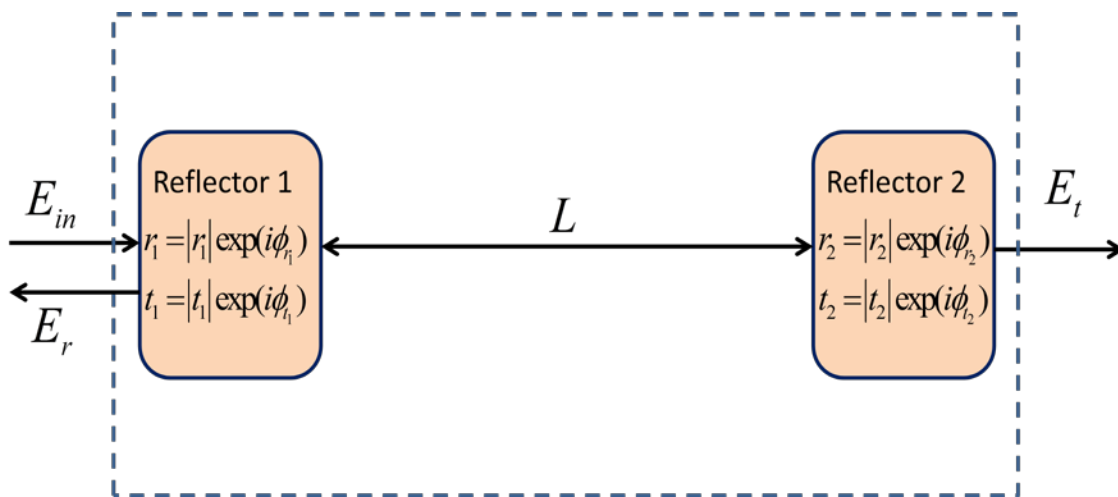


Fig. 10.1 Schematic illustration of WLC: two reflectors are separated by L to form a modified FP cavity.

The cavity has a length L between the surfaces of the reflectors and a mean refractive index n_0 . The field reflection coefficient and transmission coefficient of the two reflectors are denoted as r_i and t_i ($i=1,2$), respectively. Note that $r_i = |r_i| \exp(j\phi_i)$ and $t_i = |t_i| \exp(j\phi_i)$ are complex numbers with the phase shift ϕ_i and ϕ_i upon reflection and transmission. Both the amplitude and phase of r_i and t_i are functions of the frequency of light. For a linear cavity setup like Fig.10.1, the input field (E_{in}) of the cavity simply relates to the output (E_t) through

$E_t/E_m = |t_1||t_2| \exp\left[j(\phi_{t_1} + \phi_{t_2})\right] / \left(1 - |r_1||r_2| \exp\left[j(\phi_{r_1} + \phi_{r_2})\right] \exp(2jn_0\omega L/c)\right)$, where ω denotes the angular frequency of the optical field. Consequently, the cavity transmission, $T_c \equiv |E_t/E_m|^2$, is

$$T_c = \frac{|t_1|^2 |t_2|^2}{1 + |r_1|^2 |r_2|^2 - 2|r_1||r_2| \cos(\Phi_{total})} \quad (10.1)$$

where $\Phi_{total} = \phi_{r_1} + \phi_{r_2} + \phi_c$. $\phi_c = 2n_0\omega L/c$ denotes the phase accumulated through propagation inside the cavity. The medium in the cavity is assumed to be dispersion-free, i.e., n_0 is frequency-independent. Thus ϕ_c is only proportional to the frequency of the light. When $\Phi_{total}(\omega_0) = 2m\pi$ (m : positive integer), the cavity is known as on resonance at frequency ω_0 . When the frequency shifts to $\omega_0 + \Delta\omega$, the total phase change of $\Phi_{total}(\omega_0)$ is given by:

$$\Delta\Phi_{total} = \Phi_{total}(\omega_0 + \Delta\omega) - \Phi_{total}(\omega_0) = \phi_{r_1}(\omega_0 + \Delta\omega) - \phi_{r_1}(\omega_0) + \phi_{r_2}(\omega_0 + \Delta\omega) - \phi_{r_2}(\omega_0) + \frac{2n_0\Delta\omega L}{c} \quad (10.2)$$

Without losing the generality, we can assume the two reflectors to be identical (i.e., $\phi_{r_1} = \phi_{r_2} = \phi_r$ and $\phi_{t_1} = \phi_{t_2} = \phi_t$). Thus,

$$\Delta\Phi_{total} = 2\left(\phi_r(\omega_0 + \Delta\omega) - \phi_r(\omega_0) + \frac{n_0\Delta\omega L}{c}\right) \approx \frac{2L\Delta\omega}{c} \left(n_0 + \frac{c\phi'_r}{L}\right) \quad (10.3)$$

where $\phi'_r = \partial\phi_r/\partial\omega|_{\omega=\omega_0}$ is the first-order derivative term in Taylor expansion of $\phi_r(\omega, \xi)$ around ω_0 .

This approximation holds since $\Delta\omega \ll \omega_0$ in this case. As seen from eqn. (10.3), when $\phi'_r = -\frac{n_0L}{c}$,

$\Delta\Phi_{total}$ would vanish and $\Phi_{total}(\omega_0 + \Delta\omega)$ would remain $2m\pi$. If this is ensured for a relatively wide range of $\Delta\omega$, which means light of different frequencies are resonant simultaneously with the cavity, the so-called WLC condition is achieved. Physically, ϕ'_r , determined from the relative phase of the individual component of the grating response, represents the time difference between the arrival of the frequency components, and is thus called the group delay. A negative

group delay means that high frequency travels a shorter distance in the reflector than the lower frequency, cancelling out the extra phase gained in cavity propagation. As such, after a round trip, the high and low frequencies both have the increase in phase for $2m\pi$ inside the WLC.

10.3 Theoretical Analysis of Linearly Chirped Bragg Grating (LCBG)

As illustrated in section 10.2, the ability to manipulate the penetration depth of light inside the reflector according to its wavelength is crucial for realizing a WLC. The negative group delay demands light with short wavelength to leave the grating earlier than the longer wavelength. If each wavelength can be associated with a desired reflection point along the length of the reflector, then the reflector will be considered an ideal candidate of the reflector. As is well-known, in a uniform grating, when the grating period equals to an integer multiple of the wavelength (the so-called Bragg condition), the reflected waves constructively interfere with each other, resulting in high total reflection close to unity. A LCBG has a Bragg condition varying as a function of position along the grating. This is achieved by ensuring that the spatial frequency of the grating, κ , varies as a function of position along the FBG. The Bragg condition for the chirp FBGs can be written as $k(z) = m \frac{\kappa(z)}{n_{eff}}$ where z is the position along the grating.

With this type of structure, the device becomes broadband in response with a varying Bragg condition along the distance. In essence this results in a device which reflects the varying frequency components of the pulse at different points along its length as shown in Fig.10. 2.

Consequently, the long wavelength components of the pulse will see a different delay to the short wavelength components. If the profile of the delay exactly cancels out the phase difference accumulated in the cavity propagation, the WLC condition is fully reached.

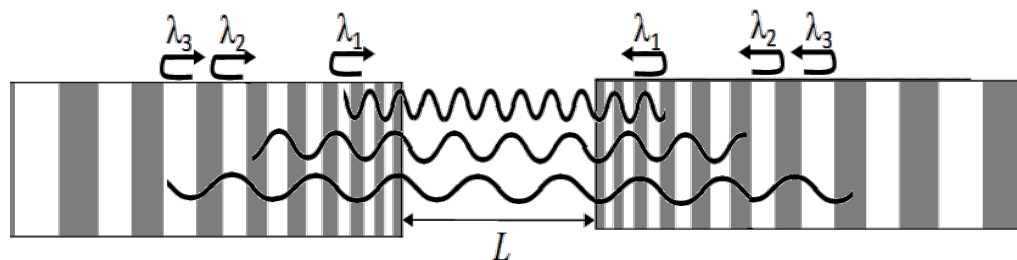


Fig. 10.2 Schematic illustration of a typical Fabry-Perot (FP) cavity of length L formed by a pair of LCBGs. Different wavelengths ($\lambda_1 < \lambda_2 < \lambda_3$) are reflected at different locations inside the grating region

In order to analyze the properties of the LCBG quantitatively, we approach the reflection and transmission of the LCBG with the well-known coupled-mode theory introduced by Kogelnik.

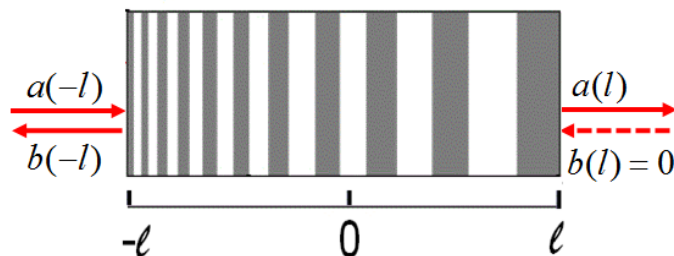


Fig. 10.3 Coupled-mode model of light propagating in the LCBG

As shown in Fig.10.3, the total field, represented by the superposition of the forward and backward propagating modes, is written as $E_{total}(z) = E_f(z) + E_b(z) = a(z)e^{ikz} + b(z)e^{-ikz}$. Thus the

reflection coefficient at the entrance of the LCBG is defined as $r = \frac{E_b(-L)}{E_f(-L)} = \frac{b(-L)}{a(-L)} e^{i2kL}$

The index modulation of the LCBG along the z-axis can be represented by $\delta n(z)/n_0 = 2\beta \cos[\theta(z)]$ where β is the modulation depth. $\theta(z) = \alpha z^2/2 + \kappa z$ in which κ denotes the modulation frequency at $z=0$ and α represents the chirping parameter. For an LCBG of length $2l$ with the origin at the center, the analytical solution of r , solved from the coupled-mode equation, is found to be

$$r = \frac{\exp(j\alpha z_0^2/2) F(j\eta; 1/2; -j\alpha(\ell/2 + z_0)^2/2) + \beta^2 k_0^2 \rho(-\ell/2 - z_0) F(1/2 + j\eta; 3/2; -j\alpha(\ell/2 + z_0)^2/2)}{jk_0 \beta \rho F(-j\eta; 1/2; j\alpha(\ell/2 + z_0)^2/2) + (-\ell/2 - z_0) F(1/2 - j\eta; 3/2; j\alpha(\ell/2 + z_0)^2/2)} e^{i2kL},$$

$$\rho = -\frac{F(j\eta; 1/2; -j\alpha(\ell/2 - z_0)^2/2)}{\beta^2 k_0^2 \rho(\ell/2 - z_0) F(1/2 + j\eta; 3/2; -j\alpha(\ell/2 - z_0)^2/2)} \quad (10.4)$$

where $F(a; b; x) = \sum_{n=0}^{\infty} \frac{a_n}{b_n} \frac{x^n}{n!}$; $a_0 = 1$; $b_0 = 1$; $a_n = a(a-1)\cdots(a-n+1)$; $b_n = b(b-1)\cdots(b-n+1)$, is the first kind

of the hypergeometrical confluent function. $z_0 = (2k - \kappa)/\alpha$ and $\eta = \beta^2 k_0^2 / (2\alpha)$ are expressed in terms of $k_0 \equiv \kappa/2$. According to Shapiro [14], z_0 implies the point where a wave of the wave number k propagating along z-axis is reflected. Thus z_0 is relevant to the effective optical length

for that particular frequency: $l_{eff} = z_0(\omega) + \ell/2$. We calculated amplitude and phase of r for a negatively chirped grating (spatial frequency decreases with distance) in Fig.10. 3 where

$2\ell = 1 \times 10^{-4} \text{ m}$, $\alpha = -6 \times 10^6 \text{ m}^{-1}$ and $\beta_0 = 6.7 \times 10^{-4}$, as shown in Fig.10. 4

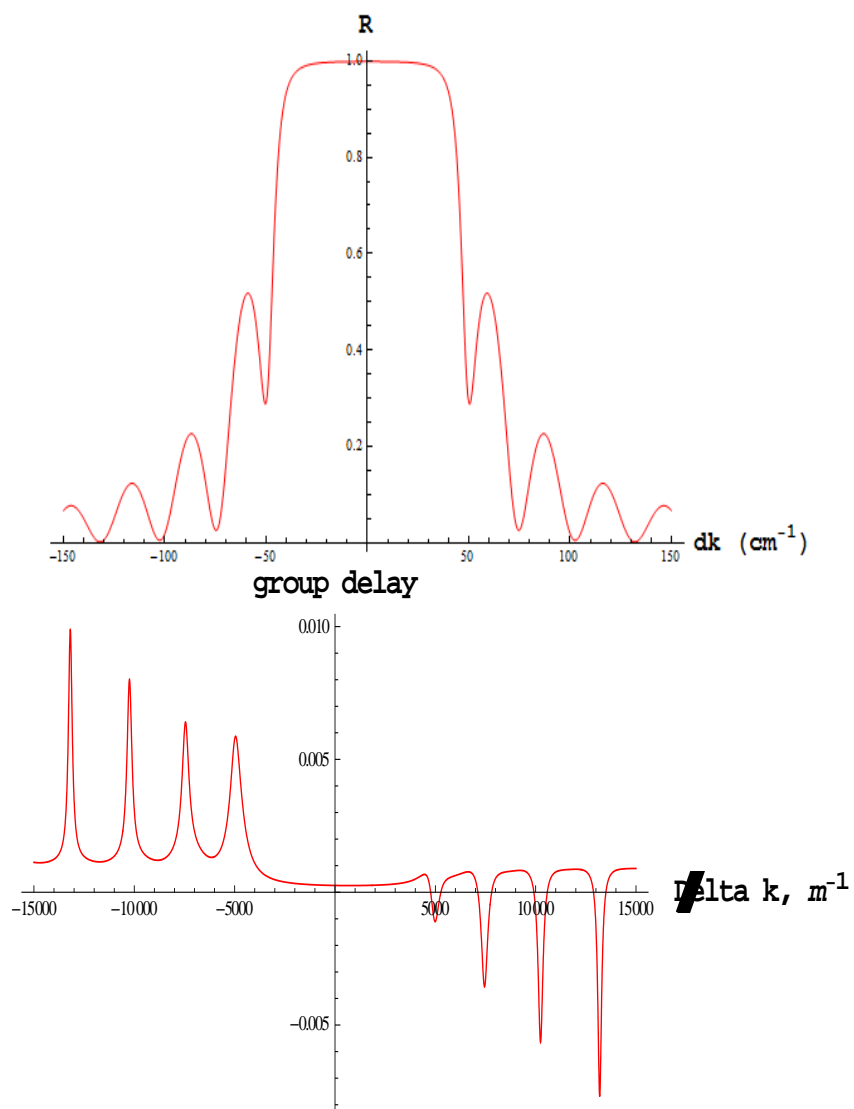


Fig. 10.4 The theoretical amplitude and phase of reflection coefficient for a negatively chirped LCBG.

As seen from Fig.10.4, to our surprise, instead of being a negative value near the resonance as predicted, $\phi' > 0$ for the detuning region near resonance. We have selected different parameters

for modulation depth, chirping rate and grating length, however, the group delay near resonance remains positive for all the combinations.

10.4 Simulating the LCBG with Transfer Matrix Method (TMM)

To verify the theoretical analysis, we simulate the reflection properties of the LCBG with numerical method. The transfer matrix method (TMM) is the most favored technique for modeling LCBG because of its speed, accuracy and the ability to handle gratings with arbitrary profiles. For this method, the grating is divided into slices much smaller in length than the grating period, so the LCBG may be considered as a piecewise representation of the continuous whole. The index change is taken to be constant within each section. Therefore, rather than a solution derived from the whole index profile of the LCBG, a discretized solution may be sought to solve each slice of the structure in a piecewise fashion, the product of these solutions approximating to the real solution of the grating structure. The detailed mathematic representation of the TMM can be found in ref¹²⁵. Fig.10. 5 shows the simulation result for amplitude and phase of r for the negative LCBG analyzed in section 3. Excellent agreement is found with the theoretical analysis in Fig.10. 4. Note that the group delay near the resonance frequency, calculated from numerical simulation, is also positive.

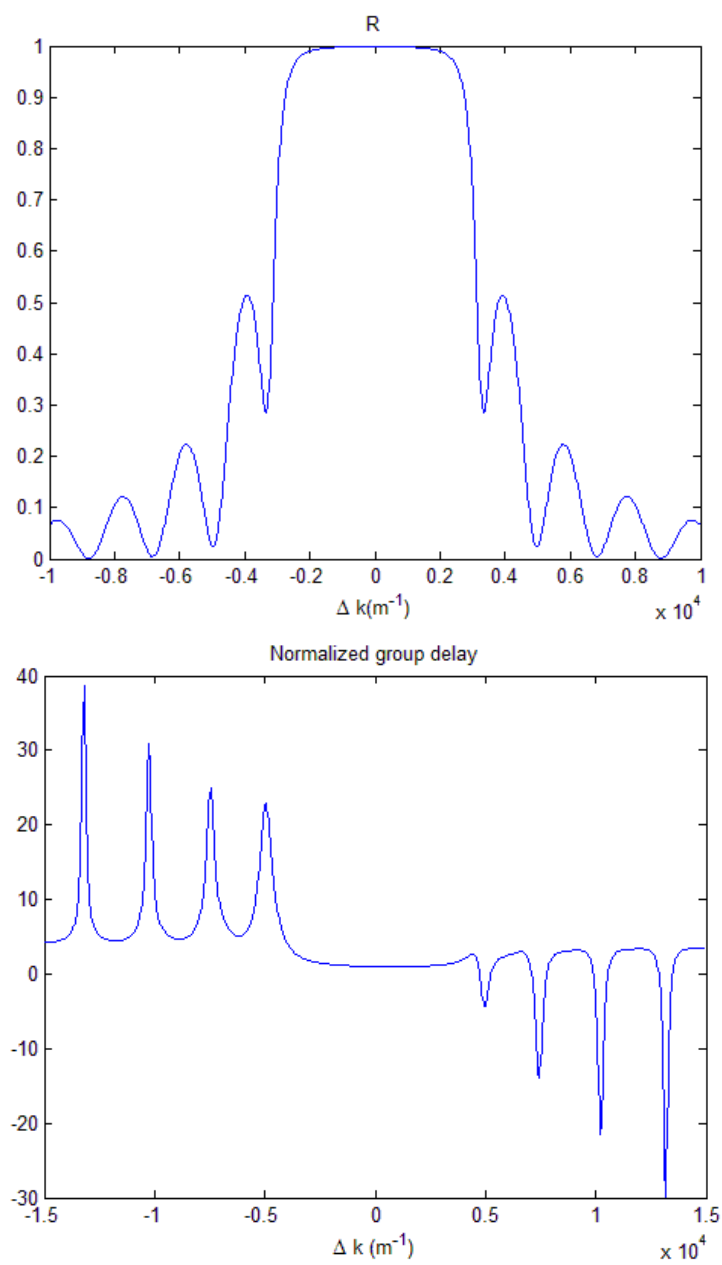


Fig. 10.5 The simulated result for amplitude and phase of reflection coefficient for the LCBG.

10.5 Revisiting the reflection properties of the LCBG

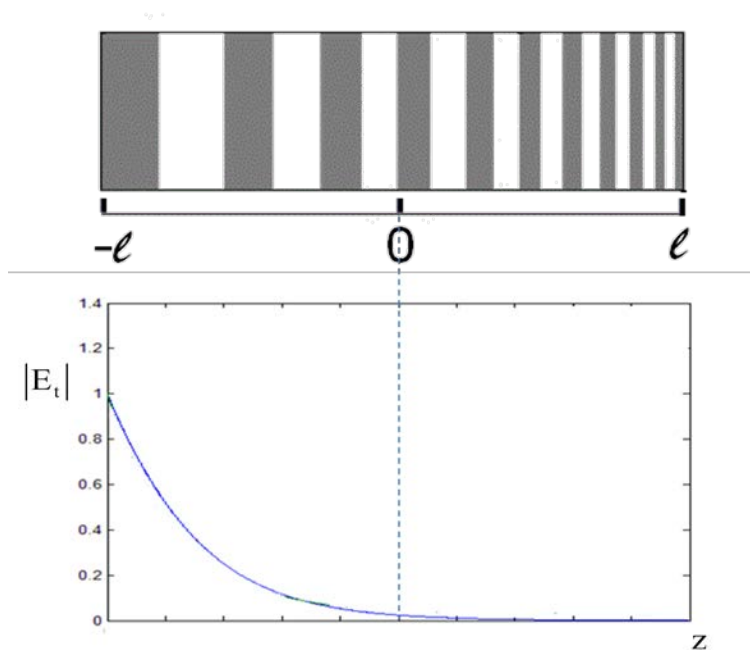


Fig. 10.6 The attenuation of forward-propagating wave in the LCBG.

The discrepancy between the physical intuition about the reflection in the LCBG and the actual analysis rooted in the ignorance of the wide band gap of the LCBG. Effectively, we can treat the LCBG as a concatenation of individual uniform FBG's, each occupying a center reflection wavelength. The physical intuition simply assumes that light is only reflected at the piece of the LCBG where Bragg condition is matched, while the other pieces in the grating have trivial effect on the reflection. However, the periodical structure of uniform gratings generates a wide reflection band near the resonance. A closer look at the field profile of the forward-propagating wave in the LCBG, as shown in Fig.10. 6, reveal that even before reaching the Bragg condition point, a significant portion of the incident wave has already been reflected. Therefore, the

reflection by other pieces inside the LCBG, even where the Bragg condition is not met, should not be neglected.

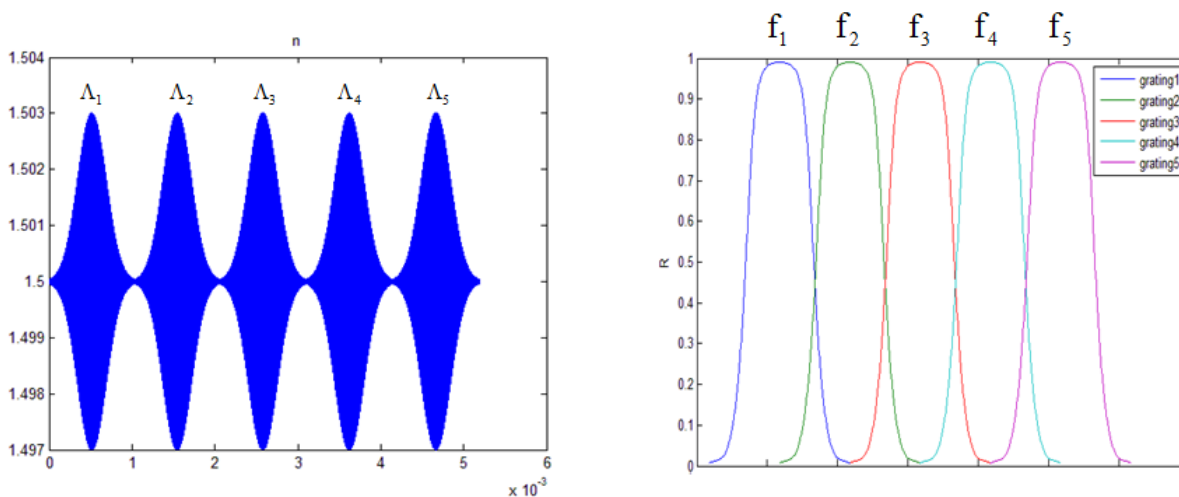


Fig. 10.7 The scheme and reflection spectrum of segmented apodized chirped grating.

To illustrate this point, we further simulated a segmented apodized chirped grating, with the center Bragg wavelength of individual gratings deliberately set far from each other so that their reflection spectra don't overlap with each other, as shown in Fig.10. 7. In this case, the light resonating with one grating is not affected by other gratings. Reflection doesn't occur until the Bragg match condition is reached. By carefully design the grating we can achieve quasi-negative-group-delay between the individual frequencies, and therefore simultaneous resonance as shown in Fig.10. 8 (a) and (b). However, this scheme is only valid for discrete and limited number of frequencies. When the frequency is off resonance, the phase of reflection is purely random as shown in Fig.10. 8 (c) and (d), resulting a random group delay. In the case of the LCBG, due to the continuous structure, the effect of scattering by the off-resonance gratings is unavoidable. As such, it is improper to claim that the penetration depth of the light in the LCBG

is linearly related to its wavelength. The simple LCBG is not suitable for constructing WLC. Whether it is possible to engineer the grating in other aspects to realize the negative group delay and thus the WLC is still an open question.

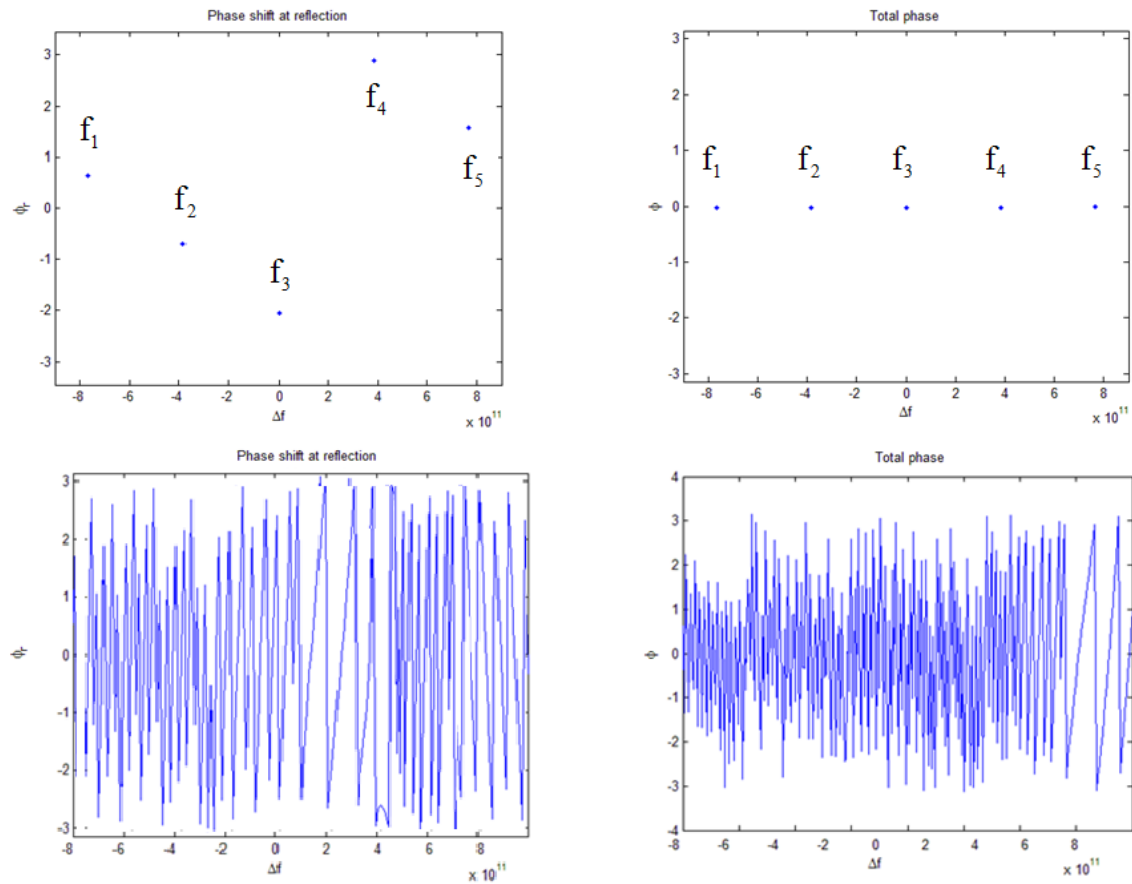


Fig. 10.8 The total phase for a round-trip propagation in the cavity based on segmented apodized chirped grating.

Reference

-
- ¹ Born, M. and Wolf, E., *Principles of Optics*, 3rd ed., Pergamon Press, New York, 1965.
 - ² Azzam, R. M. A. and Bashara, N. M., *Ellipsometry and Polarized Light*, North-Holland, Amsterdam, 1977.
 - ³ Towne, D. H., *Wave Phenomena*, Addison-Wesley, Reading, MA, 1964.
 - ⁴ Wood, R. W., *Physical Optics*, 3rd ed., Optical Society of America, Washington, D.C., 1988.
 - ⁵ Haosheng Lin and Thomas Rimmel, *Astr. Phys. J.* 514(1), 448-455 (1999)
 - ⁶ Johannes F. de Boer, Thomas E. Milner, and J. Stuart Nelson, *Opt. Lett.* 24, 300-302 (1999)
 - ⁷ Duggin, M.J.; Kinn, G.J.; Schrader, M., *Proc. SPIE* 3121, 307–313 (1997).
 - ⁸ Shurcliff, W. A., *Polarized Light*, Harvard University Press, Cambridge, MA, 1962.
 - ⁹ Stokes, G. G., *Trans. Camb. Phil. Soc.*, 9, 399 (1852). Reprinted in *Mathematical and Physical Papers*, Vol. 3, Cambridge University Press, London, 1901
 - ¹⁰ Jenkins, F. S. and White, H. E., *Fundamentals of Optics*, McGraw-Hill, New York, 1957.
 - ¹¹ Mueller, H., Report No. 2 of the OSRD project OEMsr-576, 1943.
 - ¹² L.J. Denes, M. Gottlieb, B. Kaminsky, and D. Huber, *Proc. SPIE*, **3240**, 8-18 (1998).
 - ¹³ Jones, R. C., *J. Opt. Soc. Am.*, **31**, 488–493 (1941).
 - ¹⁴ Jones, R. C., *J. Opt. Soc. Am.*, **32**, 486–493 (1942).
 - ¹⁵ Jones, R. C., *J. Opt. Soc. Am.*, **37**, 107–110 (1947).
 - ¹⁶ Poincaré H., *Theorie Mathématique de la Lumière*, Gauthiers-Villars, Paris, 1892.
 - ¹⁷ Hecht, E. and Zajac, A., *Optics*, Addison-Wesley, Reading, MA, 1974.

-
- ¹⁸ Clarke, D. and Grainger, J. F., *Polarized Light and Optical Measurement*, Pergamon Press, Oxford, 1971.
- ¹⁹ T-W. Nee, S-M. F. Nee, M. W. Kleinschmit, M. S. Shahriar, *J. Opt Soc Am.*, **A 21**, 532-539 (2004).
- ²⁰ Amrit Ambirajan and Dwight C. Look, Jr., *Opt. Eng.* **34**, 1651–1655 (1995).
- ²¹ Amrit Ambirajan and Dwight C. Look, Jr., *Opt. Eng.* **34**, 1656–1659 (1995).
- ²² T. Nee, S.F. Nee, *Proc. SPIE* **2469**, 231 (1995).
- ²³ Curran, P.J., *Remote Sens. Environ.* **12**, 491-499, (1982).
- ²⁴ J. Chen, T. N. Pappas, A. Mojsilovic, and B. E. Rogowitz, *IEEE Trans. Image Processing*, **14**, 1524-1536, (2005)
- ²⁵ M.S. Shahriar, J.T. Shen, R. Tripathi, M. Kleinschmitt, T. Nee, S.F. Nee, *Opt, Lett*, **29**, 298 (2004).
- ²⁶ E. Chow, S. Y. Lin, S. G. Johnson, P. R. Villeneuve, J. D. Joannopoulos, J. R. Wendt, G. A. Vawter, W. Zubrzycki, H. Hou, and A. Alleman, *Nature* **407**, 983 (2000).
- ²⁷ J. M. Hickmann, D. Solli, C. F. McCormick, R. Plambeck, and R. Y. Chiao, *J. Appl. Phys.* **92**, 6918 (2002)
- ²⁸ Solli D R, McCormick C F, Chiao R Y and Hickmann J M, *Opt. Photonics News*, **35** (2003)
- ²⁹ M.S. Shahriar, J.T. Shen, M.A. Hall, R. Tripathi, J.-K. Lee, A. Heifetz, *Opt. Comm.*, **245**, 67–73 (2005)
- ³⁰ Jong-Kwon Lee, John T. Shen, Alexander Heifetz, Renu Tripathi, M. S. Shahriar, *Opt. Comm.* **259**, 484-487 (2006)

-
- ³¹ Jong-Kwon Lee, John.T. Shen, Alex. Heifetz, and M.S. Shahriar, *Opt. Comm.* **277**, 63-66 (2007)
- ³² B. Li, J. Zhou, L. Li, X. J. Wang, X. H. Liu, and J. Zi, *Appl. Phys. Lett.*, **83**, 4704 (2003)
- ³³ Golosovsky, Y. Saado, and D. Davidov, *Appl. Phys. Lett.*, **75**, 4168 (1999)
- ³⁴ Kim and V. Gopalan, *Appl. Phys. Lett.*, **78**, 3015 (2001)
- ³⁵ M. R. Hee, D. Huang, E. A. Swanson, and J. G. Fujimoto, *J. Opt. Soc. Am. B* **9** 903-908 (1992)
- ³⁶ D. Huang, E. A. Swanson, C. P. Lin, D. Huang, E. A. Swanson, C. P. Lin, J. S. Schuman, W. G. Stinson, W. Chang, M. R. Hee, T. Flotte, K. Gregory, C. A. Puliafito, J. G. Fujimoto, *Science* **254**, 1178-1181 (1991)
- ³⁷ A.F. Fercher, *J. Biomed. Opt.*, **1**, 157-173 (1996).
- ³⁸ M. Brezinski, *Optical Coherence Tomography: Principles and Applications*, Elsevier, Burlington, 2006.
- ³⁹ J. M. Schmitt, *IEEE J. Sel. Top. Quantum Electron.* **5**, 1205-1215 (1999).
- ⁴⁰ Fujimoto, J. G. *Nat. Biotechnol.* **21**, 1361-1367 (2003).
- ⁴¹ Wolfgang Drexler, *J. Biomed. Opt.*, **9**, 47-74 (2004).
- ⁴² W. Drexler, U. Morgner, F. X. Kartner, C. Pitris, S. A. Boppart, X. D. Li, E. P. Ippen and J. G. Fujimoto, *Opt. Lett.* **24**, 1221-1223 (1999).
- ⁴³ Zhihua Ding, Hongwu Ren, Yonghua Zhao, J. Stuart Nelson, and Zhongping Chen, *Opt. Lett.*, **27**, 243-245 (2002).
- ⁴⁴ Michael R. Hee, David Huang, Eric A. Swanson, and James G. Fujimoto, *J. Opt. Soc. Am. B* **9**,

903-908 (1992).

⁴⁵ Richard C. Haskell, Francis D. Carlson, and Paul S. Blank, *Biophys. J.*, **56**, 401-413 (1989).

⁴⁶ J. F. de Boer, T. E. Milner, and J.S. Nelson, *Opt. Lett.* **24**, 300-302 (1999).

⁴⁷ J. F. deBoer, S. Srinivas, A. Malekafzali, Z. P. Chen, and J. S. Nelson, *Opt. Exp.* **3**, 212-218 (1998).

⁴⁸ Christoph K. Hitzenberger, Erich Götzinger, Markus Sticker, Michael Pircher and Adolf F. Fercher, *Opt. Exp.* **9**, 780-790 (2001).

⁴⁹ M. J. Everett, K. Schoenenberger, B. W. Colston, Jr., and L. B. Da Silva, *Opt. Lett.* **23**, 228-230 (1998).

⁵⁰ G. Yao and L. V. Wang, *Opt. Lett.* **24**, 537-539 (1999).

⁵¹ Shuliang Jiao, Gang Yao, and Lihong V. Wang, *Appl. Opt.* **39**, 6318-6324 (2000).

⁵² The part of light at ω_a , reflected from the sample, does not contribute to the observed signal because of path length mismatch.

⁵³ See, for example, M. Sargent, M. O. Scully, and W. E. Lamb, *Laser Physics*, Addison-Wesley, London, 1974.

⁵⁴ D. Goldstein, *Polarized Light*, 2nd Ed., CRC Press, New York, 2003.

⁵⁵ M. I. Mishchenko and J. W. Hovenier, *Opt. Lett.* **20**, 1356-1358 (1995).

⁵⁶ Valery Tuchin, *Tissue Optics*, SPIE press, 2000.

⁵⁷ J. Welzel, "Optical coherence tomography in dermatology: a review", *Skin Res and Tech*, **7**, 1-9 (2001).

⁵⁸ R. Steiner et al., *Med. Laser Appl.* **18**, 249-259 (2003)

-
- ⁵⁹ C. Bowd et al., Arch Ophthalmol., **118**, 22-26. (2000).
- ⁶⁰ Y. Wang et al., J. Biomed. Opt. **13**, 064003-064010 (2008).
- ⁶¹ M. C. Pierce et al., J Invest Dermatol, **123**, 458–463 (2004).
- ⁶² M.G. Ducros et al., IEEE J. Sel. Top. Quantum Electron., **5**, 1159-1167 (1999).
- ⁶³ E. Gotzinger et al., Opt. Express **17**, 4151-4165 (2009).
- ⁶⁴ M. G. Ducros et al., J. Opt. Soc. Am. A **18**, 2945-2956 (2001).
- ⁶⁵ S. Sakai et al., Biomed. Opt. Express, **2**, 2623-2631 (2011)
- ⁶⁶ J. A. Burns et al., Head Neck Surg, **145**, 91-99 (2011).
- ⁶⁷ K. Twietmeyer et al., Opt. Express **16**, 21339-21354 (2008).
- ⁶⁸ M. H. Smith et al., Proc. SPIE, **3911**, 210-216 (2000).
- ⁶⁹ M. Antonelli et al., Opt. Express **18**, 10200-10208 (2010)
- ⁷⁰ X. Liu, S. C. Tseng, R. Tripathi, A. Heifetz, and M.S. Shahriar, Opt. Comm. **284**, 3497–3503(2011).
- ⁷¹ J. L. Eaves and E. K. Reedy, eds., *Principles of Modern Radar*, Van Nostrand Reinhold, New York, 1987.
- ⁷² M. I. Skolnik, *Introduction to Radar Systems*, 2nd ed., McGraw-Hill, NY, 1962.
- ⁷³ Oliver C. and Quegan S., *Understanding Synthetic Aperture Radar Images*, Artech House, London, 1998.
- ⁷⁴ L.J. Sullivan, SPIE **227**, 148–161. (1980).
- ⁷⁵ Walter G. Egan, *Optical Remote Sensing Science and Technology*, Marcel Dekker, 2004.
- ⁷⁶ Henderson, B.W., Aviat. Week Space Technol. **132**, 75-76 (1990).

-
- ⁷⁷ T. Nee and S. F. Nee, Proc. SPIE **2469**, 231–241 (1995).
- ⁷⁸ Harold Mott, "Remote Sensing with Polarimetric Ladar", John Wiley & Sons, Inc., Hoboken, New Jersey, 2007
- ⁷⁹ Hecht, E. and Zajac, A., *Optics*, Addison-Wesley, Reading, MA, 1974.
- ⁸⁰ P.J. Curran, Remote Sens. Environ. **12**, 491-499, (1982).
- ⁸¹ M. J. Duggin, Proc. SPIE **3754**, 108-117 (1999).
- ⁸² Shih-Yau Lu and Russell A. Chipman, J. Opt. Soc. Am. A **13**, 1106-1113 (1996)
- ⁸³ Brian J. DeBoo, Jose M. Sasian, and Russell A. Chipman, Appl. Opt. **44**, 5434-5445 (2005)
- ⁸⁴ Egan, W.G., Johnson, W.R., & Whitehead, V.S. , Applied Optics, **30**, 435–442 (1991).
- ⁸⁵ Prosch, T., Hennings, D., & Raschke, E., Applied Optics, **22**, 1360–1363 (1978).
- ⁸⁶ Chenault, D.B., Pezzaniti, J.L., & Chipman, R.A. Proceedings SPIE, **1746**, 231–246 (1992).
- ⁸⁷ Boucher, Y., Cosnefroy, H., Petit, A.D., Serrot, G., & Briottet, X. Proceedings SPIE, **3699**, 16–26 (1999).
- ⁸⁸ Bréon, F.M., Tanré, D., Lecomte, P., & Herman, M. IEEE Transactions on Geoscience and Remote Sensing, **33**, 487–499 (1995).
- ⁸⁹ Haosheng Lin and Thomas Rimmele, Astr. Phys. J. **514**, 448-455 (1999)
- ⁹⁰ Duggin, M.J.; Kinn, G.J.; Schrader, M., Proc. SPIE **3121**, 307–313 (1997).
- ⁹¹ R. H. Rinkleff, and A. Wicht, Phys. Scr. T. **118**, 85–88 (2005).
- ⁹² A. Rocco, A. Wicht, R.-H. Rinkleff, and K. Danzmann, Phys. Rev. A, **66**, 053804 (2002).
- ⁹³ A. Wicht, K. Danzmann, M. Fleischhauer, M. Scully, G. Miller, and R. H. Rinkleff, Opt. Commun. **134**, 431–439 (1997).

-
- ⁹⁴ M. Salit, G. S. Pati, K. Salit and M. S. Shahriar, *J. of Modern Optics*, **54**, 2425–2440 (2007).
- ⁹⁵ H.N. Yum, M. Salit, J. Yablon, K. Salit, Y. Wang, and M.S. Shahriar, *Optics Express*, **18**, 17658-17665 (2010).
- ⁹⁶ R. Fleischhaker, and J. Evers, *Phys. Rev. A*, **78**, 051802 (2007)
- ⁹⁷ Y. Okawachi, M. S. Bigelow, J. E. Sharping, Z. Zhu, A. Schweinsberg, D. J. Gauthier, R. W. Boyd, and A. L. Gaeta, *Phys. Rev. Lett.*, **94**, 153902 (2005).
- ⁹⁸ K. Y. Song, M. G. Herráez, and L. Thévenaz, *Opt. Exp.*, **13**, 82–88 (2005).
- ⁹⁹ K. Y. Song, K. S. Abedin and K. Hotate, *Opt. Exp.*, **16**, 225-230 (2008).
- ¹⁰⁰ K. Y. Song, K. S. Abedin, K. Hotate, M. G. Herráez and L. Thévenaz, *Opt. Exp.*, vol. **14**, 5860-5865 (2006).
- ¹⁰¹ Z. Zhu, D.J. Gauthier and R.W. Boyd, *Science*, **318**, 1748-1750, (2007).
- ¹⁰² H.N. Yum, M.E. Kim, Y.J. Jang and M.S. Shahriar, *Opt. Exp.* , **19**, 6705-6713 (2011)
- ¹⁰³ G.S. Pati, M. Salit, K. Salit and M.S. Shahriar, *Phys. Rev. Lett.*, **99**, 133601, (2007).
- ¹⁰⁴ Q. Xu, S. Sandhu, M. L. Povinelli, J. Shakya, S. Fan and M. Lipson, *Phys. Rev. Lett.*, **96**, 123901 (2006).
- ¹⁰⁵ Q. Xu, P. Dong and M. Lipson, *Nat. Phys.* **3**, 406-410, (2007).
- ¹⁰⁶ J. Scheuer, A. A. Sukhorukov, and Y.S. Kivshar, *Opt. Lett.*, **35**, 3712-3714, (2010).
- ¹⁰⁷ P. Dong, L. Chen, Q. Xu and M. Lipson, *Opt. Lett.* , **35**, 2315-2317, (2009).
- ¹⁰⁸ E.F Burmeister, D.J. Blumenthal and J.E. Bowers, *Optical Switching and Networking*, **5**, 10-18 (2008).
- ¹⁰⁹ R. Langenhorst, M. Eiselt, W. Pieper, G. Grobkopf, R. Ludwig, L. Kuller, E. Dietrich and H.

-
- G. Weber, "Fiber loop optical buffer," *J. Lightw. Technol.*, vol. 14, no. 3, pp. 324–335, Mar. 1996.
- ¹¹⁰ A. Agrawal, L. Wang, Y. Su and P. Kumar, "All-optical loadable and erasable storage buffer based on parametric nonlinearity in fiber," *J. Lightw. Technol.*, vol. 23, no. 7, pp. 2229–2238, Jul. 2005.
- ¹¹¹ K. Hall and K. Rauschenbach, "All-optical buffering of 40-Gb/s data packets," *IEEE Photon. Technol. Lett.*, vol. 10, no. 3, pp. 442–444, Mar. 1998.
- ¹¹² A. Loayssa, R. Hernández, D. Benito and S. Galech, "Characterization of stimulated Brillouin scattering spectra by use of optical single-sideband modulation," *Opt. Lett.*, vol. 29, no.6, pp. 638–640, Mar. 2004.
- ¹¹³ J.E. Heebner, R.W. Boyd and Q. Park, "Slow light, induced dispersion, enhanced nonlinearity, and optical solitons in a resonator-array waveguide," *Phys. Rev. E*, vol. 65, 036619, Mar. 2002.
- ¹¹⁴ J.E. Heebner and R.W. Boyd, "'Slow' and 'fast' in resonator-coupler waveguide," *J. Mod. Opt.*, vol. 49, no. 14/15, pp. 2629–2636, 2002.
- ¹¹⁵ L.J. Wang, A. Kuzmich and A. Dogariu, "Gain-assisted superluminal light Propagation," *Nature*, vol. 406, pp. 277–279, Jul. 2000.
- ¹¹⁶ H.N. Yum, Y.J. Jang and M.S. Shahriar, "Pulse propagation through a dispersive intracavity medium," under review. Available: <http://arxiv.org/abs/1012.4483>.
- ¹¹⁷ O.V. Belai, E.V. Podivilov, D.A. Shapiro, "Group delay in Bragg grating with linear chirp," *Opt. Comm.*, 266, 512-520 (2006).
- ¹¹⁸ K. O. Hill, F. Bilodeau, B. Malo, T. Kitagawa, S. Thériault, D. C. Johnson, J. Albert, and K.

Takiguchi, *Optics Letters*, **19**, 1314-1316 (1994)

¹¹⁹ François Ouellette, *Optics Letters*, **12**, 847-849 (1987)

¹²⁰ B. J. Meers, *Phys. Rev. D*, **38**, 2317 (1988).

¹²¹ G. Heinzl, K.A. Strain, J. Mizuno, K. D. Skeldon, B. Willke, W. Winkler, R. Schilling, A. Rüdiger, and K. Danzmann, *Phys. Rev. Lett.* **81**, 5493 (1998).

¹²² M. B. Gray, A. J. Stevenson, H.-A. Bachor, and D. E. McClelland, *Appl. Opt.* **37**, 5886 (1998).

¹²³ S. Wise, G. Mueller, D. Reitze, D. B. Tanner, and B. F. Whiting, *Classical Quantum Gravity* **21**, S1031 (2004).

¹²⁴ S. Wise, V. Quetschke, A.J. Deshpande, G. Mueller, D.H. Reitze, D.B. Tanner and B.F. Whiting, *Phys. Rev. Lett.* **95**, 013901 (2005).

¹²⁵ Pochi Yeh, *Optical Waves in Layered Media*, Wiley, New York, 1991.